Fall 12-2019

NanoThermoMechanical Logic Gates for Thermal Computing

Ahmed Hamed
University of Nebraska-Lincoln, a.hamed@huskers.unl.edu

NANOTHERMOMECHANICAL LOGIC GATES FOR THERMAL COMPUTING

by

Ahmed Hamed

A DISSERTATION

Presented to the Faculty of

The Graduate College at the University of Nebraska

In Partial Fulfillment of Requirements

For the Degree of Doctor of Philosophy

Major: Mechanical Engineering and Applied Mechanics

(Thermal Science)

Under the Supervision of Professor Sidy Ndao

Lincoln, Nebraska

December, 2019

NANOTHERMOMECHANICAL LOGIC GATES FOR THERMAL COMPUTATION

Ahmed Hamed, Ph.D.

University of Nebraska, 2019

Advisor: Sidy Ndao

Limited performance and reliability of electronic devices at extreme temperatures, intensive electromagnetic fields, and radiation found in space exploration missions (i.e., Venus & Jupiter planetary exploration, and heliophysics missions) and earth-based applications require the development of alternative computing technologies. Thermal computing, data processing based on heat instead of electricity, is proposed as a practical alternative and opens a new scientific area at the interface between thermal and computational sciences.

We successfully developed thermal AND, OR and NOT logic gates, achieved through the coupling between near-field thermal radiation and MEMS thermal actuation. In the process, we developed two novel non-linear thermal expansion designs of microstructure silicon V-shaped chevron beams which were required to achieve the desired thermal AND gate operation. The successful design paves the way to develop full thermal logic circuits, so we show the design and simulation of a thermal calculator based on binary mathematical computations. This thermal calculator was able to perform the addition of two decimal numbers.

Furthermore, we introduce the microfabrication and characterization of the thermal AND and OR logic gates. The thermal AND logic gate consists of two non-linear mechanisms using novel and ingenious chevron mechanisms consisting of spring-assisted

reduction and cascading chevrons amplification for the reducing and the amplification mechanisms, respectively. The experimental results show that we achieved non-linearity ratios of thermal expansion $\frac{\beta}{\alpha}$ of 0.36 and 3.06 for the reducing and the amplification mechanisms, respectively. For the characterization of thermal AND logic gate, for the case when the two inputs were at T_{min} (i.e., 0,0 case), we achieved an effectiveness of 10.7 % at a heat source temperature of 1549 K. For the thermal OR logic gate, for the cases of (1,0) and (0,1), we achieved an effectiveness of 25.3 % and 23.2 % at an input temperature of 1324 K and 1391 K, respectively. These results are significant breakthroughs in the field of thermal computation science and technology as they demonstrate thermal computing at high temperatures based on demonstrated and easy to manufacture NanoThermoMechanical logic gates.

To my father, my mother, my siblings, my wife, and my kids

ACKNOWLEDGEMENTS

I am grateful to Prof. Sidy Ndao for advising and supporting me to accomplish my Ph.D. research. I am thankful to Prof. Ndao guidance to learn advanced sciences and technologies that helped me significantly to open my mind to promising applications. I appreciate the confidence Prof. Ndao expressed in my abilities and his investment in my scientific training, especially in clean-room microfabrication. I appreciate the time freedom Prof. Ndao granted me, which was essential to understand the field of electromagnetics and to develop my skills using cluster computing. I would like to express my gratitude to Dr. Mahmoud Elzouka for sharing his clean-room experience with me. I am thankful to Prof. Jeffrey Shield, Prof. Timothy Wei and Prof. Christos Argyropoulos, who accepted to be the members of my Advisory committee and advised me with their valuable suggestions.

I would like to thank the funding agencies which participated funding the research accomplished in this dissertation; Department of Mechanical and Materials Engineering and the College of Engineering at University of Nebraska-Lincoln, Office of Research and Economic Development at University of Nebraska-Lincoln and National Science Foundation.

Finally, I would like to thank my father, my mother, my siblings, my wife, and my kids for their support to accomplish this dissertation.

GRANT INFORMATION

Table of Contents

LIST OF TABLES

LIST OF FIGURES

NOMENCLATURE

A_{cond}	Conduction cross sectional area
$\boldsymbol{A}$	Magnetic vector potential
$\boldsymbol{B}$	Magnetic flux density
c	Speed of light
C	4$^{\text{th}}$ order elasticity tensor
d_c	Separation distance between two slabs
$\boldsymbol{D}$	Electric flux density
E_b	Blackbody emissive power
$E_{b,\lambda}$	Blackbody spectral emissive power
$\boldsymbol{E}$	Electric field vector
F	Deformation gradient
$\boldsymbol{F}_V$	Body force
g	Green's function
$\bar{\bar{\boldsymbol{g}}}$	Weyl component of dyadic Green's function
$\bar{\bar{\boldsymbol{G}}}^e$	Electric dyadic Green's function
$\bar{\bar{\boldsymbol{G}}}^m$	Magnetic dyadic Green's function
$\hbar$	Circular Planck's constant

$\boldsymbol{H}$	Magnetic field vector
$\bar{\bar{I}}$	Dyadic idem factor
$\boldsymbol{J}$	Current density vector
$\boldsymbol{J^r}$	Random current density vector
k	Thermal conductivity
k_B	Boltzmann constant
k_v	Wavevector in vacuum
k_ρ	Component of wavevector parallel to the surface
$\mathbf{k}$	Wavevector
n	Refractive index
$\boldsymbol{P}$	Poynting vector
q	Radiative heat flux
q_{abs}^{prop}	Radiative heat flux absorbed due to propagating waves
q_{abs}^{evan}	Radiative heat flux absorbed due to evanescent waves
$Q_{cond,I \to O}$	Conductive heat transfer from the input to the output terminals
$Q_{cond,S \to C}$	Conductive heat transfer from the heat source to the output terminal C
$Q_{rad,C \to A}$	Radiative heat transfer between C and A terminals
$Q_{rad,C \to B}$	Radiative heat transfer between C and B terminals

$Q_{rad,H \to O}$ Radiative heat transfer between the heat source and the output terminal

$Q_{rad,O \to L}$ Radiative heat transfer between the output terminal and the heat sink

r Fresnel reflection coefficient

R Reflectance of electromagnetic waves

$\boldsymbol{r}$ Position vector

S Second Piola-Kirchhoff stress tensor

S_{ex} Extra stress contribution from initial stresses and viscoelastic stresses

t Time

    Fresnel transmission coefficient

T Temperature

    Transmittance of electromagnetic waves

T_{max} Maximum operating temperature

T_{min} Minimum operating temperature

T_{ref} Strain reference temperature

T_{room} Room operating temperature

u_v Electromagnetic volumetric energy density in vacuum

$\mathbf{u}$ Displacements

V Volume

z_c	Coordinate of point where radiation is calculated

Greek symbols

α	Displacement rate of the terminal between T_{room} and T_{min}
	Thermal expansion coefficient
β	Displacement rate of the terminal between T_{min} and T_{max}
δ	Dirac-delta function
Δ_{CA}	Separation distances between output terminal C and input terminals A
Δ_{CB}	Separation distances between output terminal C and input terminals B
Δ_{OL}	Separation distances between the output terminal and the heat sink
Δ_{IO}	Separation distances between the output terminal and the source
ε	Electric permittivity
	Total strain
ε_{el}	Elastic strain
ε_{inel}	Inelastic strains
ε_{th}	Thermal strain
ε_r	Relative electric permittivity (dielectric function)
$\bar{\varepsilon}$	Real component of electric permittivity
$\acute{\varepsilon}_r$	Real component of relative electric permittivity

ε_r''	Imaginary component of relative electric permittivity
ε_v	Vacuum permittivity
ϵ	Effectiveness of thermal logic gate
Γ	Collision frequency
Θ	Mean energy of Planck's oscillator
λ	Wavelength of radiation
λ_{Th}	Wavelength of thermal radiation
μ	Magnetic permeability
μ_r	Relative magnetic permeability
μ_v	Vacuum permeability
ρ_e	Electric charge volumetric density
σ	Electric conductivity
τ	Spectral transmissivity
ϕ_e	Electric scalar potential
ω	Radiation angular frequency (rad/s)
ω_p	Plasma frequency
ξ	Energy transmission coefficient

Chapter 1: Introduction

1.1. Motivation

Electronics have limited performance in harsh environments (e.g., elevated temperature, external electric fields and ionizing radiation environments) found in many engineering applications such as space exploration (e.g., Venus) and geothermal energy exploitation deep beneath the earth; consequently, developing alternative computing technologies is necessary. Integrated electronic logic circuits are composed of nonlinear and switchable electronic elements such as transistors, diodes, and switches. The existence of these electronic building blocks achieves the effective transmission of electrical power. The traditional linear and passive thermal components, such as thermal resistors and capacitors, are not sufficient to introduce an integrated thermal logic circuit. It is needed to realize switchable and nonlinear thermal components as their electronic counterparts, which leads to tunable thermal control devices and paves the way for thermal computation technology and thermal information treatment. Thermal computing has the potential to unlock the mysteries of outer space, explore and harvest our own planet's deep-beneath-the-surface geology, and harness waste heat for more efficient-energy utilization.

1.2. Thermal Computation

Any computational task can be broken down into a series of simple logic operations using logic gates. The basic logic gates, which are the building blocks for any logic circuit, are the AND, OR and NOT gates. Logic states (i.e., input and output states), used in computational operations, can take one of two values, namely, High or Low. The high and low are relative, and they are determined by a specified threshold. The more

contrast there is between the high and low values, the more robust a logic system is. Logic circuits work on the basis of current flow control using for example preferential flow resistance elements called diodes. Diodes are devices which allow current to pass in one direction (called the diode's forward direction), while blocking it in the opposite direction (the reverse direction). In an electrical circuit, the current is the flow of electric charges with ONE (1) and ZERO (0) logic states; whereas in a thermal circuit with ONE corresponding to the high temperature (T_{max}) and ZERO corresponding to the low temperature (T_{min}), current is represented by the heat flow.

Heat transfer is the thermal energy flow across the boundaries of a system with a spatial temperature difference. There are three main modes for heat transfer: conduction through solids and fluids, convection through fluids, and radiation through solids, fluids or even vacuum. Due to the recent rapid advancements in microtechnology and nanotechnology, the device or structure characteristic length can become comparable to the mean free path of the energy and information carriers (electrons, photons, phonons, and molecules). Consequently, it is important to understand the microscopic pictures behind heat transfer phenomena (i.e., thermal energy transport at micro- and nanoscale). Many attempts have been proposed to realize thermal diodes, switches, and transistors [1] [2] [3]. By the conduction heat transfer mechanism, researchers realized thermal switches and regulators based on the thermal conductivity change of system materials such as: vanadium oxide (VO_2) due to its metal-insulator transition temperature [4]. In this study, it was reported an order-of-magnitude breakdown of the Wiedemann-Franz law at temperatures ranging from 240 to 340 K in metallic VO_2 in the vicinity of its metal-insulator transition. The thermal conductivity of $Ge_2Sb_2Te_5$ can be manipulated based on

the switching between the metastable structural states (i.e., amorphous phase, fcc phase $\sim$130 °C and hcp phase $\sim$200 °C), since the phonon and electron contributions to volume and interface heat conduction in the three phases were separated [5] [6]. The measured of the thermal conductivity for $Ge_2Sb_2Te_5$ films were reported $0.25 \pm 0.05 \, W/m.K$ for the amorphous phase, $0.45 \pm 0.09 \, W/m.K$ for the cubic (fcc) phase, and $1.32 \pm 0.18 \, W/m.K$ for the hexagonal (hcp) phase. Hexadecane/graphite composite materials have a variation in thermal conductivity up to 3.2 times near solid-liquid transition temperature $\sim$18 °C [7]. The graphene was reported to achieve an order of magnitude increase in the thermal conductivity and the breakdown of the Wiedemann-Franz law in the thermally populated charge-neutral plasma in graphene, and this is due to electrostatic gating at liquid nitrogen temperatures $\sim$75 °C [8]. Through manipulating the nanoscale ferroelastic domain structure of $Pb(Zr,Ti)O_3$ film with applied electric fields, the room-temperature thermal conductivity was reversibly tuned and modulated by 11% [9]. In addition, thermal switches and regulators can be realized by solid-solid and solid-liquid contact switches and regulators [10] [11].

By the convection heat transfer mechanism, thermal switches and regulators can be realized based on jumping droplets of water on superhydrophobic and superhydrophilic surfaces [12]. In the forward direction, the superhydrophobic surface is the condenser, so self-propelled jumping drops are returning the working fluid from the superhydrophobic condenser to the superhydrophilic evaporator; developing continuous phase-change heat transfer. In the reverse direction, the liquid drops are trapped by the superhydrophilic condenser, which results in a planar phase-change diode with an orientation-independent diodicity of over 100. Another approach to realize thermal

switches and regulators is electrowetting. Coplanar electro-wetting-on-dielectric configuration was used to realize a liquid-droplet-based thermal switch [13]. By changing the conductive path between two silicon dies using electrowetting to move a thin layer of dielectric liquid, OFF/ON thermal resistances ratios of up to 14 were reported [14]. Additionally, applying an electric field was used to turning bubbles on and off during boiling using charged surfactants, which resulted in rapid and reversible altering of heat transfer performance up to an order of magnitude [15].

Regarding the thermal radiation mechanism, thermal switches and diodes can be realized based on the change of VO_2 emissivity across metal-insulator transition of VO_2 [16] [17] [18], and the change of the near-field gap size [19] [20]. Most of the proposed thermal nonlinear devices are designed based on the material properties transition, which limits the operation of the thermal device around certain temperature (i.e. the transition temperature) and using a specific material. Until now, no full operating thermal logic circuit has been shown. We propose the thermal AND, OR, and NOT logic gates achieved through the coupling between near-field thermal radiation (NFTR) and MEMS thermal actuation.

1.3. Analogy Between Thermal Computation and Electronic Computation

As beforementioned here, logic circuits work on the basis of current flow control using for example preferential flow resistance elements called diodes. To create a thermal diode, we need to control the resistance of heat flow in response to the heat flow direction. Due to the high contrast between the near-field thermal radiation and the far-field thermal radiation, here, we employ NFTR through a vacuum to manipulate heat transfer between two terminals in the forward as well as in the reverse directions by carefully manipulating

the separation gap [19]. Therefore, Forward versus Reverse directions can be achieved by switching (i.e., controlling the vacuum gap) between far-field and near-field thermal radiation between two terminals, resulting in thermal diodes. Using this concept, our group has previously demonstrated, experimentally, high temperature near-field NanoThermoMechanical rectification [19]. As shown in Figure *1-1*, the thermal diode consists of two terminals (upper and lower). Initially, both terminals are at low temperatures, T_{min}, separated by a spacing, d_{ini}, large enough to suppress any near-field radiative heat transfer. The gap also remains the same as both terminals are set to T_{max}. In the forward bias, the upper and lower terminals' temperatures are set to T_{max} and T_{min}, respectively. This causes the upper terminal to move downward, effectively reducing the separation gap and significantly increasing the heat transfer rate through NFTR. By reversing the heat flow direction by switching the temperatures of the terminals (i.e., reverse bias), the terminals move farther apart from each other and therefore reduce the heat transfer rate.
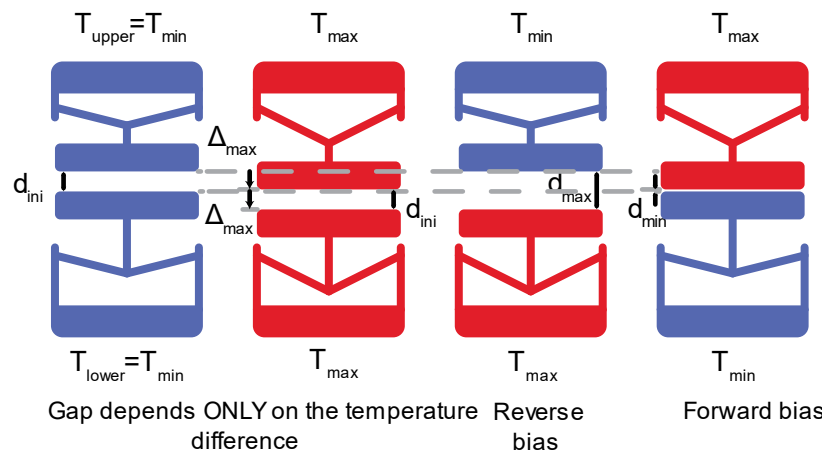
Figure 1-1: Schematic drawing of the proposed thermal diode.

Using the thermal diodes described above, thermal logic gates can be constructed. Figure *1-2* shows the analogy between electronic and thermal logic AND gates based on

diodes. A simple logic AND gate takes two logic inputs (A and B) and returns an output C. Based on the AND gate 'truth table', the gate output is ONE (1) (i.e., T_{max} for the thermal gate) only if both inputs are ONEs (T_{max}), otherwise it returns an output as ZERO (0)(T_{min}). The electrical resistance between the source (i.e., the heat source in the thermal gate) and the output terminal C is analogous to a conductive resistance.
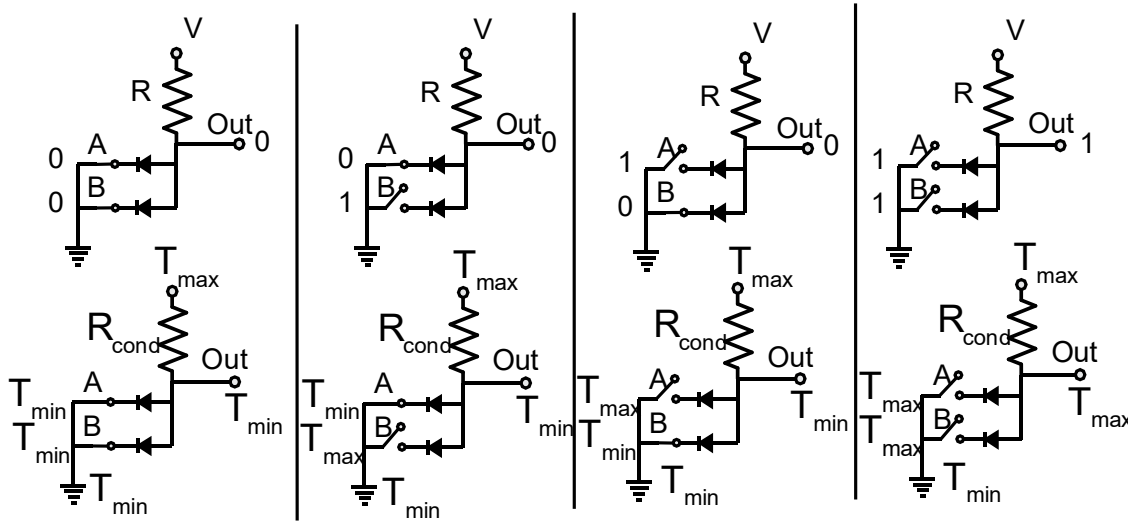
Figure 1-2: Analogy between the electronic and thermal logic AND gates.

Figure 1-3 shows the analogy between electronic and thermal logic OR gates based on diodes. A simple logic OR gate takes two logic inputs (A and B) and returns an output C. Based on the OR gate 'truth table', the gate output is ONE (1) (i.e., T_{max} for the thermal gate) if any input is ONE (T_{max}), otherwise it returns an output as ZERO (0)(T_{min}). The electrical resistance between the ground (i.e., heat sink in the thermal gate) and the output terminal C is analogous to a conductive resistance.
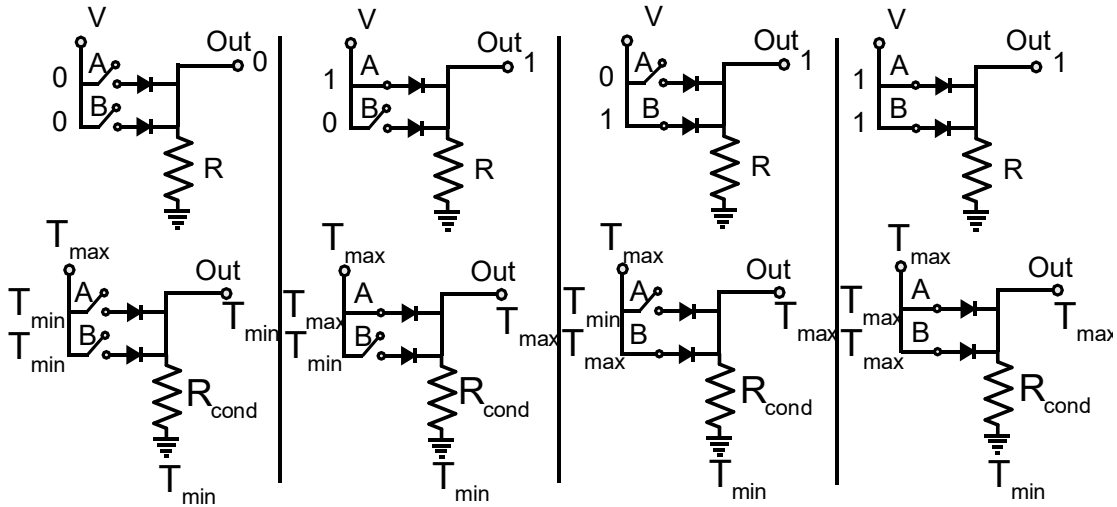
Figure 1-3: Analogy between the electronic and thermal logic OR gate.

1.4. An Overview on Thermal Radiation

Thermal emissions from the real macrostructures can be described by comparison to the emitted thermal radiation from the blackbody at the same temperature using the emissivity of the surface. This classical theory of thermal radiation is referred to as the far-field regime of radiative heat transfer (i.e., far-field radiation), where the structure, or the separation distance between structures exchanging the radiative energy, is more than the dominant wavelength of thermal radiation as predicted by Wien's law [21].

For micro- and nanostructures, where the structures or the separation distances are comparable to the dominant wavelength of the thermal radiation $\left(\lambda_{Th} = \frac{\hbar c}{k_B T}\right)$, the microscopic picture behind the transport process should be considered. The exchange of radiative heat between bodies basically takes the form of electromagnetic waves (i.e., electromagnetic radiation). Electromagnetic radiation is generated by accelerating charges (electric or conceptually magnetic charges), whose sources are found in any material because of electrons and nuclei with negative and positive charges, respectively. According to statistical mechanics and at a finite (non-zero) temperature, the value of

each microscopic property of the system, including the velocity of particles comprising the material, fluctuates around its macroscopic average. These fluctuations are termed as thermal motion, which results in the random mechanical vibrations of the charges (i.e., accelerated charges). Therefore, the thermal fluctuation of charges is a mechanism to exchange energy via thermal radiative heat transfer.

Back to the blackbody concept, the maximum possible electromagnetic density (energy per unit volume), that can populate inside a cavity with opaque walls, can be described as

$$u_v = \frac{\omega^3}{\pi^2 c^3} \frac{1}{e^{\frac{\hbar\omega}{k_B T}} - 1} \hbar\omega = \frac{\hbar\omega^3}{\pi^2 c^3 \left(e^{\frac{\hbar\omega}{k_B T}} - 1 \right)} \tag{1-1}$$

where u_v is the spectral electromagnetic energy density (energy per unit volume per unit frequency). The first term on the right-hand side of equation *(1-1)*, $\frac{\omega^3}{\pi^2 c^3}$, is the density of electromagnetic states (DOS), which represents the number of possible propagating electromagnetic waves/states in a unit volume at a certain frequency. The second term, $\frac{1}{e^{\frac{\hbar\omega}{k_B T}} - 1}$, is the Bose-Einstein distribution, which represents the probability of the existence of photons at a certain frequency for a certain temperature. The third term, $\hbar\omega$, represents the energy of the single photon.

Electromagnetic waves are divided into two categories: propagating waves and evanescent waves. As illustrated in Figure *1-4*, The propagating waves (or modes) are those modes that extend in space for several wavelengths, so they are transferred from one body to another, thus resulting in a net heat transfer. The evanescent waves are those waves that have high intensity near the emitter's surface, and their intensity decays

exponentially over a distance of about a wavelength normal to the surface. In the blackbody radiation calculations, propagating waves are only considered, and surface evanescent waves are ignored since they have no access to the whole vicinity inside the enclosure, away from the surface.
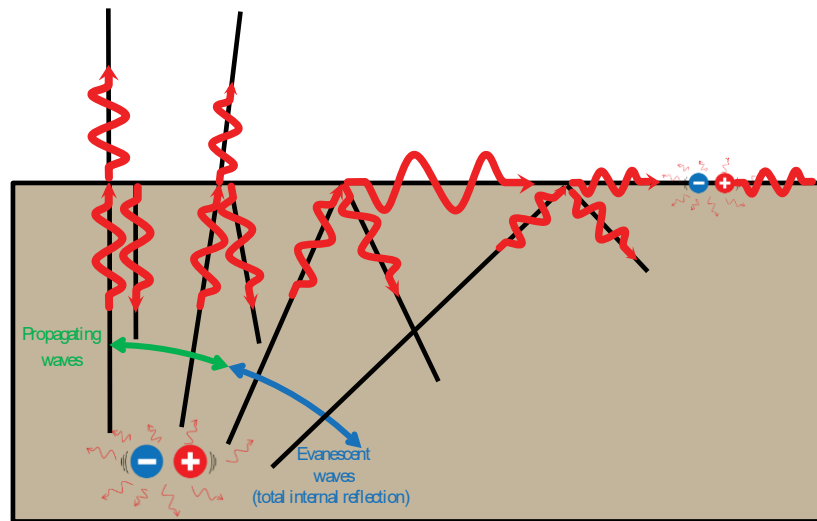
Figure 1-4: Schematic of the mechanism of thermal radiation

On the other hand, in the case of the vicinity comparable to or smaller than the characteristic thermal wavelength, the evanescent waves are tunneled and contribute the net radiative thermal transport between the structures. This regime is referred to as the near-field regime of radiative heat transfer (i.e., near-field radiation), which can greatly exceed the far-field blackbody limit. The fluctuation–dissipation theorem (FDT) attributes the origin of thermal emission to the random motion of charges, which in turn, produces a fluctuating current. Fluctuational electrodynamics, which combines FDT with Maxwell's electromagnetic wave theory, is able to describe both the far-field and near-field thermal radiation phenomena. Though the time average of the electromagnetic field due to the randomly fluctuating current is zero, the energy density can be very high near the surface and the Poynting vector depends on the correlation of the fluctuating currents.

1.5. Organization of the Dissertation

This dissertation aims to introduce novel NanoThermoMechanical logic gates, achieved through the coupling between near-field thermal radiation and MEMS thermal actuation, to be the building blocks of thermal computation technology. The dissertation has the following structure:

- Chapter 2 presents the theoretical background required to cover the topics presented in the dissertation. The chapter describes the near-field thermal radiation physically and includes an analytical method using dyadic Green's function for calculating near-field thermal radiation.

- Chapter 3 introduces the design and modeling of thermal AND, OR, and NOT logic gates, achieved through the coupling between near-field thermal radiation and MEMS thermal actuation. In the process, two novel non-linear thermal expansion designs of microstructured chevron beams were developed. The chapter also shows the stability of the designed NanoThermoMechanical logic gates and their ability to be clustered and used in a full thermal logic operator (i.e., a thermal calculator) to perform complex operations.

- Chapter 4 presents the design, microfabrication, and characterization of the two non-linear mechanisms required to achieve the desired thermal AND gate operation. The two non-linear mechanisms were microfabricated using novel and ingenious chevron mechanisms consisting of spring-assisted reduction and cascading chevrons amplification for the reducing and the amplification mechanisms, respectively.

- Chapter 5 presents the microfabrication and characterization of the NanoThermoMechanical AND and OR logic gates. The results of the experimental measurements show thermal logic operations can be achieved successfully through demonstrated and easy-to-manufacture NanoThermoMechanical logic gates.

- Chapter 6 summarizes the outcomes of the dissertation, and points to future research directions based on achievements outlined in the dissertation.

Chapter 2:   Theoretical Background

2.1. Fundamentals of Thermal Radiation: Near-Field and Far-Field

Radiation heat transfer is different from conduction and convection, as the heat can be transferred without a medium and propagated in a vacuum. This is because all surfaces of finite temperature emit energy in the form of electromagnetic waves (photons). In macroscale structures, thermal radiation is treated as incoherent photon particles (i.e., rays propagating in straight lines) with the neglect of the phase information carried by the electromagnetic waves, and the concepts of geometric optics can therefore be used for modeling such a transport mechanism [22]. The photon particles can be scattered, absorbed along the path, or enhanced by emission of the medium along the propagation direction. Upon reaching a surface, thermal radiation can be transmitted, absorbed, or reflected. In addition, thermal radiation calculations in macroscale are based on the blackbody concept. A blackbody is defined as the perfect absorber and emitter that can absorb all incident radiation at all incidence angles and all wavelengths [21]. Consequently, it is known in classical physics that the maximum possible emitted thermal radiation is achieved by the blackbody, and its total and spectral characteristics are described by the Stefan-Boltzmann law (equation (2-1)) and according to Planck's law (also called Planck distribution) (equation (2-2)), respectively.

$$E_b = \sigma T^4 \tag{2-1}$$

$$E_{b,\lambda} = \frac{\hbar \omega^3}{4\pi^2 c^2 \left(e^{\frac{\hbar \omega}{k_B T}} - 1 \right)} \tag{2-2}$$

where E_b is the total emissive power of a blackbody at temperature T, $\sigma (=$

$5.67 \times 10^{-8} W/m^2 K^4$) is the Stefan-Boltzmann constant, $E_{b,\lambda}$ is the spectral emissive

power (the rate at which radiation of a wavelength is emitted in all directions from a

surface per unit wavelength interval $d\lambda$ about λ and per unit surface area), $\hbar$ is the

circular Planck's constant (i.e., Planck's constant over 2π), ω is the frequency of the

electromagnetic wave $\left(\omega = \frac{2\pi c}{\lambda}\right)$, c is the speed of the electromagnetic radiation

propagation, and k_B is the Boltzmann constant.

The spectrum of electromagnetic radiation is illustrated in Figure 2-1, where the

intermediate portion of the spectrum (approximately from 0.1 to 100 μm) is referred to as

the thermal radiation (i.e., the UV and all of the visible and infrared (IR)). Consequently,

thermal radiation is basically an electromagnetic radiation; consequently, its generation,

propagation and absorption can be analyzed using basic laws of electromagnetics. Table

2-1 displays the basic laws of electromagnetics, which were introduced by James Clark

Maxwell, in four equations set (i.e., Maxwell's equations) [23].
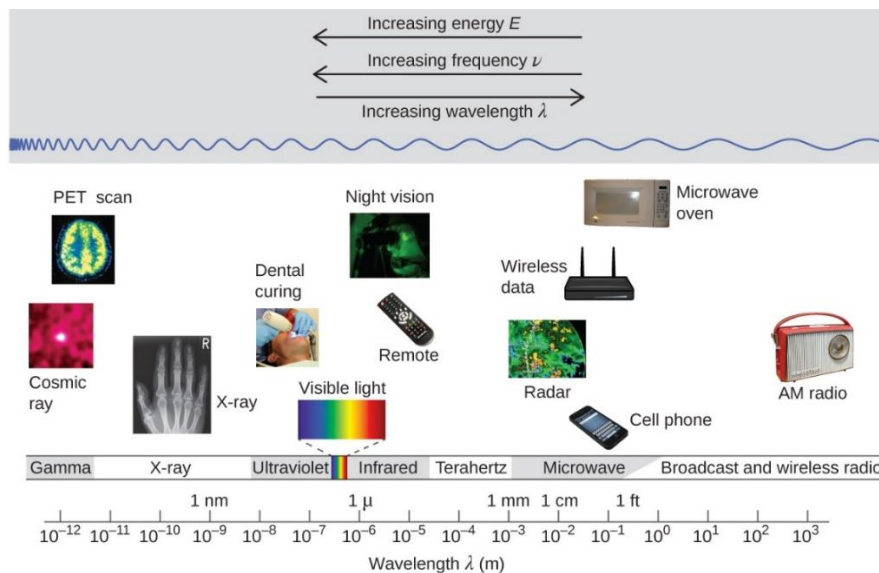
Figure 2-1: Electromagnetic spectrum *[24]*

Table 2-1: Maxwell's equations

Time domain	Frequency domain		
$$\nabla \times E(r,t) = -\frac{\partial B(r,t)}{\partial t}$$ $$= -\mu \frac{\partial H(r,t)}{\partial t}$$	$$\nabla \times E(r,\omega) = i\omega B(r,\omega)$$ $$= i\omega\mu H(r,\omega)$$	Faraday's law	(2-3)
$$\nabla \times H(r,t) = J(r,t) + \frac{\partial D(r,t)}{\partial t}$$ $$= J(r,t) + \bar{\varepsilon}\frac{\partial E(r,t)}{\partial t}$$	$$\nabla \times H(r,\omega) = J(r,\omega) - i\omega D(r,\omega)$$ $$= \sigma E(r,\omega) - i\omega\bar{\varepsilon}E(r,\omega)$$ $$= -i\omega(\bar{\varepsilon} + i\frac{\sigma}{\omega})E(r,\omega)$$ $$= -i\omega\varepsilon E(r,\omega)$$	Ampere's law	(2-4)
$$\nabla \cdot D(r,t) = \rho_e$$ $$\nabla \cdot (\bar{\varepsilon}E(r,t)) = \rho_e$$	$$\nabla \cdot D(r,\omega) = \rho_e$$ $$\nabla \cdot (\bar{\varepsilon}E(r,\omega)) = \rho_e$$	Gauss's law	(2-5)
$$\nabla \cdot B(r,t) = 0$$ $$\nabla \cdot (\mu H(r,t)) = 0$$	$$\nabla \cdot B(r,\omega) = 0$$ $$\nabla \cdot (\mu H(r,\omega)) = 0$$	Gauss's law	(2-6)

The current continuity relation can be given as;

$$\nabla \cdot J(r,\omega) = i\omega\rho_e \tag{2-7}$$

The relationship between the electric/magnetic flux densities (D, B) and the electric/magnetic field intensities (E, H), respectively, can be defined using constitutive relations;

$$D = \varepsilon E \tag{2-8}$$

$$B = \mu H \tag{2-9}$$

The Fourier transform is applied to convert the components of the fields between time domain and frequency domain;

$$A(r,t) = A(r)Re\left[e^{-i\omega t}\right] \tag{2-10}$$

where A can be any of the fields D, B, E, or H.

Electric permittivity ε and magnetic permeability μ are employed in Maxwell's equations to define the electromagnetic properties of the material. The electric permittivity for isotropic media contains imaginary and real parts ($\varepsilon = \bar{\varepsilon} + i\frac{\sigma}{\omega}$). The imaginary part represents the delay in the polarization response to the applied electric field due to both electric conductivity (σ) and frequency (ω); so this part represents the losses to the propagating electromagnetic fields in the material. The relative electric permittivity, which is the ratio between the electric permittivity of the material and the vacuum, is commonly used and it is known as the dielectric constant, $\varepsilon_r = \frac{\varepsilon}{\varepsilon_v} = \acute{\varepsilon}_r + i\varepsilon_r''$.

For the magnetic permeability μ, its value for the majority of materials will be set to that of the vacuum, due to the absence of magnetic response; $\mu = \mu_v = 4\pi \times 10^{-7}\ Tm/A$.

The speed of propagation of the electromagnetic radiation c (i.e., speed of light) and the refractive index of the material n can be calculated using electric permittivity and magnetic permeability of the material:

$$c = \frac{1}{\sqrt{\mu\varepsilon}} \tag{2-11}$$

$$n = \sqrt{\mu_r \varepsilon_r} \tag{2-12}$$

Due to the unity of relative magnetic permeability for nonmagnetic materials, the refractive index can be described as:

$$n = \sqrt{\varepsilon_r} \tag{2-13}$$

In Maxwell's equations, the sources of electromagnetic radiation are electric current density J and electric charge density ρ_e. In thermal radiation, bodies are

considered as neutral, so electric charge density is usually zero. Therefore, the electric current density is the only source for electromagnetic radiation problems. In thermal radiation, the electric current density is randomly fluctuating with dependence on emitter temperature through some correlation driven by the fluctuation-dissipation theorem.

The randomness in the current density in thermal radiation requires a minor modification in Maxwell's equations. Consequently, according to the approach invented by Rytov [25], Ampere's law is modified by adding random current density term $\boldsymbol{J^r}$, which represents the force that raises the fluctuations in electromagnetic fields (i.e., the origination of thermal radiation). The inclusion of the random current density term results in the stochastic Maxwell's equations, which are the basis of fluctuational electrodynamics.

The rate of heat transfer by thermal radiation from the emitter to the receiver can be calculated using the time-averaged Poynting vector, whose amplitude in a certain direction is the radiative heat transfer rate in that direction [23]:

$$\langle \boldsymbol{P(r,\omega)} \rangle = \frac{1}{2} Re[\langle \boldsymbol{E(r,\omega)} \times \boldsymbol{H^*(r,\omega)} \rangle] \tag{2-14}$$

The time-averaged values are used since they are the measured values, especially if the oscillation frequencies of the fields are above terahertz. In addition, the time-dependent fields are decomposed in the frequency domain as follows:

$$\boldsymbol{A(r,t)} = \int\limits_{-\infty}^{\infty} \boldsymbol{A(r,\omega)} e^{-i\omega t} \frac{d\omega}{2\pi} \tag{2-15}$$

However, it is preferred to consider only the positive frequencies in thermal radiation problems. Therefore, the frequency domain decomposition takes the form,

$$A(\boldsymbol{r}, t) = 2 \int_0^\infty A(\boldsymbol{r}, \omega) e^{-i\omega t} \frac{d\omega}{2\pi} \tag{2-16}$$

Consequently, the time-averaged Poynting vector can be expressed as

$$\langle \boldsymbol{P}(\boldsymbol{r}, \omega) \rangle = 4 \times \frac{1}{2} Re[\langle \boldsymbol{E}(\boldsymbol{r}, \omega) \times \boldsymbol{H}^*(\boldsymbol{r}, \omega) \rangle] \tag{2-17}$$

2.1.1. Fluctuation-Dissipation Theorem: Correlating Random Current Density to Temperature

As mentioned hereinbefore, the fluctuation-dissipation theorem governs the relationship between the random current density $\boldsymbol{J}^r$ and the temperature. By applying the fluctuation-dissipation theorem to linear systems (i.e., the impedance/resistance is linear in the applied force), a relation can be established between thermal fluctuation in a certain variable at thermal equilibrium and the impedance of the system to the same variable, which dissipates the energy into heat [26].

Regarding the thermal radiation, all kinds of electromagnetic waves carry energy. The electromagnetic waves can be absorbed by a certain material, resulting in the dissipation of the electromagnetic waves (i.e., introducing resistance to these waves). This is the mechanism to convert the waves' energy into thermal energy (i.e., heat). Moreover, according to the fluctuation-dissipation theorem, there is a reverse process that converts this internal thermal energy into random fluctuations that emit electromagnetic radiation.

The fluctuation-dissipation theorem establishes the relationship between the ensemble average of the spatial correlation function of the fluctuating electric current density $\boldsymbol{J}^r$, and the emitter's temperature through

$$\langle J_\alpha^r(\boldsymbol{r}',\omega)J_\beta^{r*}(\boldsymbol{r}'',\omega')\rangle$$

$$= \frac{1}{\pi}\big(\omega\varepsilon_v\varepsilon_r''(\omega)\big)\Theta(\omega,t)\delta(\boldsymbol{r}'-\boldsymbol{r}'')\delta(\omega-\omega')\delta_{\alpha\beta}$$

(2-18)

where J_α^r is the current density in direction α (x, y, or z), $\Theta(\omega,t)$ is the mean energy of Planck's oscillator,

$$\Theta(\omega,t) = \frac{\hbar\omega}{e^{\frac{\hbar\omega}{k_B T}}-1}$$

(2-19)

Dirac delta functions, $\delta(\boldsymbol{r}'-\boldsymbol{r}'')$ and $\delta(\omega-\omega')$, are indicating that currents are uncorrelated in spatial space, and uncorrelated in the frequency domain. $\delta_{\alpha\beta}$ is the Kronecker delta which equals 1 for $\alpha=\beta$, and zero otherwise (i.e., isotropic media). In addition, the correlation of fluctuating current density is proportional to $\omega\varepsilon_v\varepsilon_r''(\omega)$, which is the material conductivity (σ). The material conductivity determines the dissipation to the electromagnetic wave travelling within the material, and higher conductivity means generating higher amplitudes of fluctuating current densities at a certain temperature (i.e., more dissipative material). Furthermore, increasing the temperature results in increasing the mean energy of Planck's oscillator, which gives rise in magnitudes of fluctuating current for conductive materials.

2.1.2. Eigen-Solutions to Maxwell's Equation

Due to the existence of uncorrelated randomly vibrating electromagnetic radiation sources within the material, we should consider all the possible temporal and spatial frequencies (i.e., frequency in rad/s and wavevector in 1/m) by including all possible solutions of Maxwell's equations for a given configuration of materials. These possible solutions can be predicted by solving a source-free version of Maxwell's equations, which are reduced to a Helmholtz equation:

$$\nabla \times \left(\frac{1}{\varepsilon} \nabla \times \boldsymbol{H}(\boldsymbol{r}, \omega) \right) = \omega^2 \mu \boldsymbol{H}(\boldsymbol{r}, \omega) \qquad (2\text{-}20)$$

Assuming dependence on time to be harmonic for all modes, $H_i(x, y, z, t) = H_i(x, y, z)e^{i\omega t}$ (i can be replaced with spatial directions x, y and z). A simplified version for isotropic media in cartesian coordinates can take the form

$$\nabla^2 H_i = -\omega^2 \varepsilon \mu H_i = -\frac{\omega^2}{c^2} H_i \qquad (2\text{-}21)$$

where H_i is any component of the magnetic field. This simplified equation can be proven to have plane wave solutions on the form [23]:

$$H_i = A_i e^{\mathbf{k.r}} \qquad (2\text{-}22)$$

where $\boldsymbol{r}$ is the position vector and $\mathbf{k}$ is the wavevector which is a representation of the wave's frequency in space (i.e., $|\mathbf{k}| = 2\pi/\lambda$), where λ is the wavelength, so the wavevector has a magnitude in each of the spatial directions (x, y and z). It is similar to temporal frequency ($\omega = 2\pi/T$) which represents the wave's frequency in time (T). This Helmholtz equation is basically an eigenmode problem, since for a media with given properties and at a given temporal frequency (ω), there are certain field solutions H_i (eigenfunction), and each solution is characterized by a wavevector value k (eigenvalue).

In thermal radiation problems, waves are the heat carriers, so the more allowed modes of waves, the more available channels to transfer the energy will be (i.e., the higher rate of radiative heat transfer). Based on the eigenvalue problem of the Helmholtz equation, each mode can be determined by temporal frequency (ω), spatial frequency ($\mathbf{k}$), and field solution profile $\boldsymbol{H}(x, y, z)$, which can be identified by the wave's polarization for plane waves in a homogenous media (i.e., transverse electric TE or transverse magnetic TM).

For an infinite slab in x and y directions, which is radiating heat to a vacuum as shown in Figure 2-2, it is convenient to define wavevectors; $k_z\hat{\mathbf{z}}$ and $\mathbf{k}_\rho = k_x\hat{\mathbf{x}} + k_y\hat{\mathbf{y}}$; according to:

$$|\mathbf{k}| = \sqrt{k_x^2 + k_y^2 + k_z^2} = \sqrt{k_\rho^2 + k_z^2} = \frac{n\omega}{c} \tag{2-23}$$

where n is the refractive index of the material through which the wave propagates, and k_ρ is the independent wavevector, parallel to the interface, and invariant in both media (a result of the electromagnetic boundary conditions). However, according to the condition of the Helmholtz equation for propagating waves, there is some limitation for k_ρ to sustain a propagating wave (i.e., real number for k_z). The allowed solutions (i.e., modes) can be categorized based on their temporal and spatial frequency into four regions.
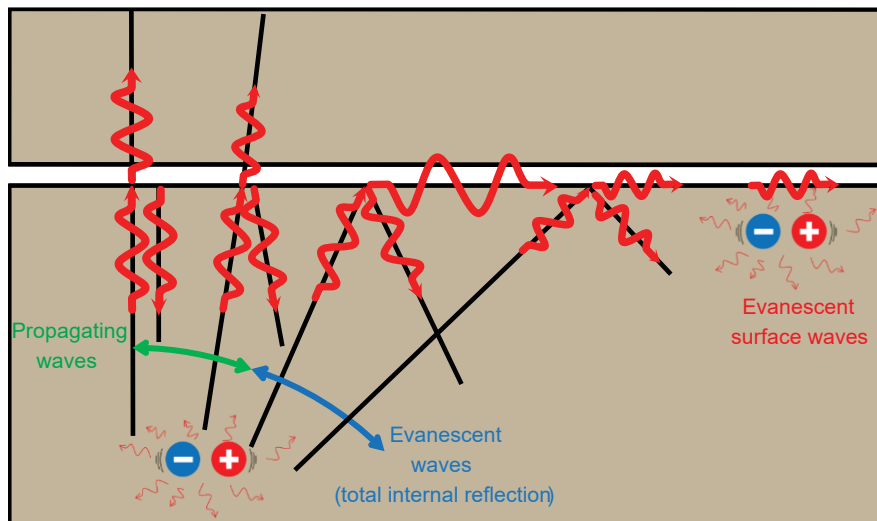
Figure 2-2: Schematic of modes of thermal radiation

The first region includes the propagating modes in both vacuum and slab $(0 < k_\rho < \omega/c)$, where these modes can be excited by every vibrating charge within the slab. Every dipole inside the bulk of one structure radiates in all directions. Based on the basic laws of physics, all the radiation with incident angles less than the critical angle of

incidence can propagate in the structure and the vacuum as well. These modes can participate in both near and far-field thermal radiation, and the blackbody radiation energy density can be calculated by counting the number of the propagating modes per unit volume per unit frequency bounded by the light line $(\omega = k_\rho c)$ multiplied by the mean energy of Planck's oscillator.

The second region includes the propagating modes in the slab, and evanescent in vacuum $(\omega/c < k_\rho < n\omega/c)$, where these modes are generated in the case of the incidence angle being larger than the critical angle of incidence. These modes represent the total internal reflection and can only participate in near-field thermal radiation, since they cannot propagate to long distances in vacuum (i.e., evanescent waves). These modes can be created in all kinds of structures and are available to all frequencies, so they do not cause resonance in heat transfer.

The third region includes the evanescent modes in the slab and vacuum (surface modes) $(k_\rho > \omega/c$ and $k_\rho > n\omega/c)$ (i.e., generated at the vicinity very close to oscillating charges near the interface), where these modes are confined to the slab-vacuum interface and are not excited by oscillating charges deep in the bulk of the structures. These modes are responsible for spectral selectivity and for the spikes in the spectral heat transfer. The fourth region includes propagating modes in the vacuum, and evanescent in the slab. These modes are not applicable for all materials since this requires an index of refraction less than 1, which happens at very narrow frequency ranges.

Based on this discussion, evanescent waves can originate from total internal reflection or surface waves at the interface. Consequently, if the receiver is brought close to the emitter, the evanescent waves can participate in thermal radiation through coupling

to other evanescent modes on the receiver's surface (surface plasmon/phonon polaritons or surface modes supported by photonic crystals). Another mechanism for the participation of evanescent waves in thermal radiation is through coupling to propagating modes inside the receiver's material $(k_\rho < n\omega/c)$ or inside hyperbolic metamaterial (for very large values of the tangential wavevector).

Enhancement of near-field thermal radiation can only be achieved by increasing the number of participating modes (i.e., increasing the allowed evanescent modes). The enhancement can be achieved through two broad approaches: by increasing the modes that are evanescent in vacuum and structures (surface phonon/plasmon polaritons and photonic crystals), and by increasing the modes that are evanescent in vacuum and propagating in structures by using hyperbolic metamaterial (i.e., much higher available wavevectors than isotropic media).

Surface phonon and plasmon polaritons are surface waves, since they can propagate and be confined along the interface but evanescent in both media around the interface. These surface waves (i.e., polaritons) are a result of coupling between the electromagnetic radiation and waves of charge oscillations at the interface. If this charge is formed by free electrons (i.e., metals and doped semiconductors), the surface wave is called surface plasmon polariton (SPP). If the charges are the ions of a dielectric, the ions and the electromagnetic waves couple to high frequency phonon waves (i.e., optical phonons); then the surface wave is called surface phonon polariton (SPhP).

2.2. Near-Field Thermal Radiation Calculation using Dyadic Green's Function

Several numerical and analytical techniques have been proposed to solve stochastic Maxwell's equations and calculate the associated Poynting vector [27] [28]

[29] [30]. This dissertation uses one of the most convenient approaches, which is dyadic

Green's function technique using the method of potentials [31] [32]. The dyadic Green's

function technique is based on generating expressions of the fields and energy flux in

terms of current source and scattering properties of the structures in order to average the

quantities based on averaging the fluctuating thermal current density.

Gauss's law ($\nabla \cdot \boldsymbol{B}(\boldsymbol{r}, \omega) = 0$), which mathematically indicates that the magnetic

flux density is a conservative vector field, can be related to the vector potential or

magnetic vector potential $\boldsymbol{A}(\boldsymbol{r}, \omega)$ as

$$\boldsymbol{B}(\boldsymbol{r}, \omega) = \nabla \times \boldsymbol{A}(\boldsymbol{r}, \omega) \tag{2-24}$$

Similarly, Faraday's can be represented as

$$\nabla \times \big(\boldsymbol{E}(\boldsymbol{r}, \omega) - i\omega \boldsymbol{A}(\boldsymbol{r}, \omega)\big) = 0 \tag{2-25}$$

Using the vector identity that the curl of a gradient of a scalar function results in

zero (i.e., $\nabla \times (\nabla. \emptyset) = 0$), the following relation can be driven from equation (2-25):

$$\boldsymbol{E}(\boldsymbol{r}, \omega) - i\omega \boldsymbol{A}(\boldsymbol{r}, \omega) = -\nabla. \emptyset_{\mathrm{e}} \tag{2-26}$$

where $\emptyset_{\mathrm{e}}$ is the electric scalar potential. By substituting in Ampere's law, a relationship

between electric scalar potential and magnetic vector potential can be established as

follows:

$$\nabla \times \boldsymbol{H}(\boldsymbol{r}, \omega) = -i\omega\varepsilon \boldsymbol{E}(\boldsymbol{r}, \omega) + \boldsymbol{J}^r(\boldsymbol{r}, \omega) \tag{2-27}$$

$$\nabla \times \big(\nabla \times \boldsymbol{A}(\boldsymbol{r}, \omega)\big) = -i\omega\varepsilon\mu\big(-\nabla. \emptyset_{\mathrm{e}} + i\omega \boldsymbol{A}(\boldsymbol{r}, \omega)\big) + \mu \boldsymbol{J}^r(\boldsymbol{r}, \omega) \tag{2-28}$$

$$\nabla \times \nabla \times \boldsymbol{A}(\boldsymbol{r}, \omega) = i\omega\varepsilon\mu\nabla. \emptyset_{\mathrm{e}} + \omega^2\varepsilon\mu \boldsymbol{A}(\boldsymbol{r}, \omega) + \mu \boldsymbol{J}^r(\boldsymbol{r}, \omega) \tag{2-29}$$

Using the vector identity $\nabla^2 \boldsymbol{A} = -\nabla \times \nabla \times \boldsymbol{A} + \nabla\nabla \cdot \boldsymbol{A}$ and using the wavevector

relation $k^2 = \omega^2\varepsilon\mu$,

$$\nabla\nabla \cdot \boldsymbol{A}(\boldsymbol{r}, \omega) - \nabla^2 \boldsymbol{A}(\boldsymbol{r}, \omega) = i\omega\varepsilon\mu\nabla. \emptyset_{\mathrm{e}} + k^2 \boldsymbol{A}(\boldsymbol{r}, \omega) + \mu \boldsymbol{J}^r(\boldsymbol{r}, \omega) \tag{2-30}$$

$$(-\nabla^2 - k^2)A(r, \omega) = i\omega\varepsilon\mu\nabla.\emptyset_e + \mu J^r(r, \omega) - \nabla\nabla \cdot A(r, \omega) \qquad (2\text{-}31)$$

$$(\nabla^2 + k^2)A(r, \omega) = \nabla\nabla \cdot A(r, \omega) - i\omega\varepsilon\mu\nabla.\emptyset_e - \mu J^r(r, \omega) \qquad (2\text{-}32)$$

Based on Lorentz gauge [32] [33],

$$\nabla \cdot A = i\omega\varepsilon\mu\emptyset_e \qquad (2\text{-}33)$$

So

$$\nabla\nabla \cdot A = i\omega\varepsilon\mu\nabla.\emptyset_e \qquad (2\text{-}34)$$

By substituting in equation (2-32),

$$(\nabla^2 + k^2)A(r, \omega) = -\mu J^r(r, \omega) \qquad (2\text{-}35)$$

which is an inhomogeneous Helmholtz equation. Using Green's function, $A(r, \omega)$ can be expressed as

$$A(r, \omega) = \int_V \mu J^r(r', \omega)g(r, r', \omega)\, dV' \qquad (2\text{-}36)$$

The integral is over the volume V where the current source is located. The Green's function $g(r, r', \omega)$ represents the response in $A(r, \omega)$ at location r due to an impulse unit current localized at a certain location r' (represented by Dirac delta function). The Green's function can be calculated independently from the current through the inhomogeneous Helmholtz equation (2-35),

$$(\nabla^2 + k^2)g(r, r', \omega) = -\delta(|r - r'|) \qquad (2\text{-}37)$$

Using the definitions in equations (2-34) and (2-36), the electric field at location r can be represented in terms of a current source at location r' by substituting in equation (2-26),

$$E(r, \omega) = i\omega\mu\left[1 + \frac{1}{k^2}\nabla\nabla \cdot\right]\int_V J^r(r', \omega)g(r, r', \omega)\, dV' \qquad (2\text{-}38)$$

And using the definitions in equations (2-24) (i.e., the magnetic vector potential) and (2-36), the magnetic field can be evaluated as

$$H(r,\omega) = \int_V \nabla \times J^r(r',\omega) g(r,r',\omega)\, dV' \tag{2-39}$$

The Green's function value obtained from equation (2-37) is based on impulse current source and has a polarization in a certain direction. Using the same equation for the other two directions, we get the vector format of electric and magnetic fields in terms of Green's function as follows:

$$E(r,\omega) = i\omega\mu \int_V g(r,r',\omega)\left[\overline{\overline{I}} + \frac{1}{k^2}\nabla\nabla\right]\cdot J^r(r',\omega)\, dV' \tag{2-40}$$

$$H(r,\omega) = \nabla \times \int_V g(r,r',\omega)\overline{\overline{I}}\cdot J^r(r',\omega)\, dV' \tag{2-41}$$

where $\overline{\overline{I}}$ is the dyadic idem factor $\left(\overline{\overline{I}} = \hat{x}\hat{x} + \hat{y}\hat{y} + \hat{z}\hat{z}\right)$, which results in a 3×3 identity matrix for cartesian coordinates. So, electric and magnetic dyadic Green's functions can be defined as:

$$\overline{\overline{G}}^e(r,r',\omega) = g(r,r',\omega)\left[\overline{\overline{I}} + \frac{1}{k^2}\nabla\nabla\right] \tag{2-42}$$

$$\overline{\overline{G}}^m(r,r',\omega) = \nabla \times \left(g(r,r',\omega)\overline{\overline{I}}\right) \tag{2-43}$$

Because the dyadic Green's function is a 3×3 matrix, as each column represents the response to a component of the electric current in a certain direction, the matrices of Green's functions are turning now to tensors (i.e., Green's tensors). By replacing the electric/magnetic field's intensity with its representation in terms of the electric/magnetic dyadic Green's functions, the Poynting vector can be expanded on the form,

$$\langle \boldsymbol{P}(\boldsymbol{r}, \omega) \rangle = 4 \times \frac{1}{2} Re[\langle \boldsymbol{E}(\boldsymbol{r}, \omega) \times \boldsymbol{H}^*(\boldsymbol{r}, \omega) \rangle]$$

$$= 2 Re\big[\langle \hat{\boldsymbol{x}}\big(E_y H_z^* - E_z H_y^*\big) + \hat{\boldsymbol{y}}\big(E_z H_x^* - E_x H_z^*\big) \tag{2-44}$$

$$+ \hat{\boldsymbol{z}}\big(E_x H_y^* - E_y H_x^*\big)\rangle\big]$$

where each component of electric field or magnetic field can be represented in terms of

the dyadic Green's function form,

$$E_m = i\omega\mu \int_V \big(G_{mx}^e \hat{\boldsymbol{x}} + G_{my}^e \hat{\boldsymbol{y}} + G_{mz}^e \hat{\boldsymbol{z}}\big) \cdot \big(J_x^r \hat{\boldsymbol{x}} + J_y^r \hat{\boldsymbol{y}} + J_z^r \hat{\boldsymbol{z}}\big) dV'$$

$$= i\omega\mu \int_V \big(G_{mx}^e J_x^r + G_{my}^e J_y^r + G_{mz}^e J_z^r\big) dV' \tag{2-45}$$

$$= i\omega\mu \int_V G_{mp}^e J_p^r \, dV'$$

By substituting in the expression of the Poynting vector in equation (2-44), the

Poynting vector that represents the radiative heat flux due to thermal fluctuating current

source can be expressed by [31]:

$$\langle \boldsymbol{P}(\boldsymbol{r}, \omega) \rangle$$

$$= 2 Re\left\{ i\omega\mu \int_V \left[\int_V \left[\begin{pmatrix} \hat{\boldsymbol{x}}\big(G_{yn}^e G_{zj}^{m*} - G_{zn}^e G_{yj}^{m*}\big) \\ +\hat{\boldsymbol{y}}\big(G_{zn}^e G_{xj}^{m*} - G_{xn}^e G_{zj}^{m*}\big) \\ +\hat{\boldsymbol{z}}\big(G_{xn}^e G_{yj}^{m*} - G_{yn}^e G_{xj}^{m*}\big) \end{pmatrix} \langle J_n^r(\boldsymbol{r}', \omega) J_j^{r*}(\boldsymbol{r}'', \omega) \rangle \right] dV'' \right] dV \right\} \tag{2-46}$$

By calculating the correlation for fluctuating random current

$\langle J_n^r(\boldsymbol{r}', \omega) J_j^{r*}(\boldsymbol{r}'', \omega) \rangle$ (i.e., equation (2-18)) and the dyadic electric and magnetic Green's

function, the heat flux for any radiative heat transfer problem can be calculated.

$$\langle \boldsymbol{P}(\boldsymbol{r},\omega)\rangle = \frac{2\omega^2\varepsilon_v\mu}{\pi}\, Re\left\{ i\int\limits_V \left[\int\limits_V \left[\begin{pmatrix} \hat{\boldsymbol{x}}\big(G^e_{yn}G^{m*}_{zj} - G^e_{zn}G^{m*}_{yj}\big) \\ +\hat{\boldsymbol{y}}\big(G^e_{zn}G^{m*}_{xj} - G^e_{xn}G^{m*}_{zj}\big) \\ +\hat{\boldsymbol{z}}\big(G^e_{xn}G^{m*}_{yj} - G^e_{yn}G^{m*}_{xj}\big) \end{pmatrix} \varepsilon''_r(\omega)\Theta(\omega,t)\delta(\boldsymbol{r}' \right. \right. $$

$$\left. \left. - \boldsymbol{r}'')\delta_{nj}\right] dV'' \right] dV' \right\}$$

(2-47)

By setting Kronecker delta to 1 and changing the dummy variables n and j into another third dummy variable α (i.e., $\delta_{nj} = 1$ if $n = j$, and 0 otherwise), summing over the three values (i.e., x, y and z), and replacing the $\omega^2\varepsilon_v\mu$ with k_v^2 (the square of the wavevector magnitude in vacuum), the Poynting vector can be expressed as follows:

$$\langle \boldsymbol{P}(\boldsymbol{r},\omega)\rangle = \frac{2k_v^2}{\pi}\, Re\left\{ i\int\limits_V \left[\int\limits_V \left[\begin{pmatrix} \hat{\boldsymbol{x}}\big(G^e_{y\alpha}G^{m*}_{z\alpha} - G^e_{z\alpha}G^{m*}_{y\alpha}\big) \\ +\hat{\boldsymbol{y}}(G^e_{z\alpha}G^{m*}_{x\alpha} - G^e_{x\alpha}G^{m*}_{z\alpha}) \\ +\hat{\boldsymbol{z}}\big(G^e_{x\alpha}G^{m*}_{y\alpha} - G^e_{y\alpha}G^{m*}_{x\alpha}\big) \end{pmatrix} \varepsilon''_r(\omega)\Theta(\omega,t)\delta(\boldsymbol{r}' \right. \right. $$

$$\left. \left. - \boldsymbol{r}'')\right] dV'' \right] dV' \right\}$$

(2-48)

2.2.1. Radiative Heat Transfer in 1D Setting

For 1D layered media, the electric and magnetic dyadic Green's functions can be estimated analytically, and hence the corresponding heat flux can be obtained [34]. For infinite problem in both x and y directions, and by considering the z component of the Poynting vector, the formula for radiative heat flux at location z_c can be reduced to:

$$q(z_c,\omega) = \frac{2k_v^2\Theta(\omega,t)\varepsilon''_r(\omega)}{\pi}\, Re\left\{ i\int\limits_V \big(G^e_{x\alpha}G^{m*}_{y\alpha} - G^e_{y\alpha}G^{m*}_{x\alpha}\big) dV' \right\}$$

(2-49)

The index α indicates the summation over the three orthogonal direction (x, y and z). By assuming a uniform temperature and a material homogeneity of the emitting layer, Θ and ε''_r will be uniform over the emitter and can be taken out of the integral.

The dyadic Green's function can be represented as the sum of plane waves that are periodic in the xy plan that have an amplitude dependent on z. Plane waves are the natural solutions for the Helmholtz wave equation in homogeneous medium. To decompose the dyadic Green's function $\overline{\overline{G}}$ into its plane wave components, spatial Fourier transform is used as follows [34] [35]:

$$\overline{\overline{G}}(r, r', \omega) = \int_{-\infty}^{\infty} \overline{\overline{g}}(\mathbf{k_\rho}, z_c, z', \omega) e^{i\mathbf{k_\rho} \cdot (R - R')} \frac{d\mathbf{k_\rho}}{(2\pi)} \tag{2-50}$$

where $R = x\hat{x} + y\hat{y}$, $\mathbf{k_\rho} = k_x\hat{x} + k_y\hat{y}$, and accordingly $d\mathbf{k_\rho} = dk_x dk_y$, $\overline{\overline{g}}$ is the Weyl component of dyadic Green's function, and it is a matrix similar to $\overline{\overline{G}}$. The difference between them is that $\overline{\overline{g}}$ predicts the electric/magnetic field response to an impulse current localized at z' for only one value for the wavevector $\mathbf{k_\rho}$, while $\overline{\overline{G}}$ returns the response for the resultant of all the components of the wave (i.e., integrated over all values of $\mathbf{k_\rho}$). Substituting by the expanded dyadic Green's function in the heat flux in 1D setting, the integral along the volume will be converted into an integral over the distance in z direction as follows:

$$\int_V \left(G_{x\alpha}^e G_{y\alpha}^{m*} - G_{y\alpha}^e G_{x\alpha}^{m*} \right) dV'$$

$$= \int_{z'=z_1'}^{z_2'} \int_{k_\rho=-\infty}^{\infty} \left(\begin{array}{c} g_{x\alpha}^e(\mathbf{k_\rho}, z_c, z', \omega) g_{y\alpha}^{h*}(\mathbf{k_\rho}, z_c, z', \omega) \\ -g_{y\alpha}^e(\mathbf{k_\rho}, z_c, z', \omega) g_{x\alpha}^{h*}(\mathbf{k_\rho}, z_c, z', \omega) \end{array} \right) \frac{d\mathbf{k_\rho}}{(2\pi)} dz' \tag{2-51}$$

Due to the azimuthal symmetry of the 1D problem, the wavevector $\mathbf{k_\rho}$ is more convenient to be transformed to polar coordinates,

$$\int\limits_{k_\rho=-\infty}^{\infty} d\mathbf{k}_\rho = \int\limits_{k_x=-\infty}^{\infty} \int\limits_{k_y=-\infty}^{\infty} dk_x dk_y = \int\limits_{k_\rho=0}^{\infty} \int\limits_{\theta=0}^{2\pi} k_\rho dk_\rho d\theta = 2\pi \int\limits_{k_\rho=0}^{\infty} k_\rho dk_\rho \quad (2\text{-}52)$$

Therefore, the Poynting vector can be expressed in z direction (i.e., radiative

energy flux in z direction) at location $z = z_c$ due to a fluctuating current source

distributed over the emitter (i.e., from $z' = z_1'$ to $z' = z_2'$), and kept at temperature T:

$q(z_c, \omega)$

$$= \frac{k_v^2 \Theta(\omega, t)\varepsilon_r''(\omega)}{\pi^2} Re \left\{ i \int\limits_{z'=z_1'}^{z_2'} \int\limits_{k_\rho=0}^{\infty} \begin{pmatrix} g_{\rho\alpha}^e(k_\rho, z_c, z', \omega)g_{\theta\alpha}^{h*}(k_\rho, z_c, z', \omega) \\ -g_{\theta\alpha}^e(k_\rho, z_c, z', \omega)g_{\rho\alpha}^{h*}(k_\rho, z_c, z', \omega) \end{pmatrix} k_\rho dk_\rho \, dz' \right\} \quad (2\text{-}53)$$

The procedure to compute the Weyl component of dyadic Green's function g

incorporates plane wave scattering calculations in 1D layered media [34] [36]. The near-

field thermal radiation 1D problem can be described based on one of three configurations,

which are thermal radiation between a semi-infinite body and a slab, two slabs

submerged in vacuum, or two semi-infinite bodies.

2.2.2. Radiative Heat Flux Inside a Slab Due to Emitting Semi-Infinite Body

For the radiative heat flux inside a slab due to an emitting semi-infinite body, as

presented in Figure 2-3, it is required to calculate near-field thermal radiation absorbed

locally by a semiconductor material to generate photocurrent. The Weyl component of

dyadic Green's function can be separated in an exponential term, and can be expressed in

the form [36]

$$g_{j\alpha}^e(k_\rho, z_c, z', \omega)g_{j\alpha}^{h*}(k_\rho, z_c, z', \omega) = g_{j\alpha}^e(k_\rho, z_c, \omega)g_{j\alpha}^{h*}(k_\rho, z_c, \omega)e^{2k_z'' z'} \quad (2\text{-}54)$$

where j and α can take any of the three directions ρ, θ, and z. By performing the

integration of equation (2-53) along z' analytically, the heat flux can be represented as:

$$q_{1\to3}(z_c,\omega)$$

$$= \frac{k_v^2 \Theta(\omega,t)\varepsilon_r''(\omega)}{\pi^2} Re\left\{i\int_{k_\rho=0}^{\infty}\begin{pmatrix} g_{1\to3,\rho\alpha}^e(k_\rho,z_c,\omega)g_{1\to3,\theta\alpha}^{h*}(k_\rho,z_c,\omega) \\ -g_{1\to3,\theta\alpha}^e(k_\rho,z_c,\omega)g_{1\to3,\rho\alpha}^{h*}(k_\rho,z_c,\omega) \end{pmatrix}\frac{k_\rho}{k_{z1}''}\,dk_\rho\right\} \quad (2\text{-}55)$$

where k_{z1}'' is the imaginary part of the z component of the wavevector in the emitter

media.
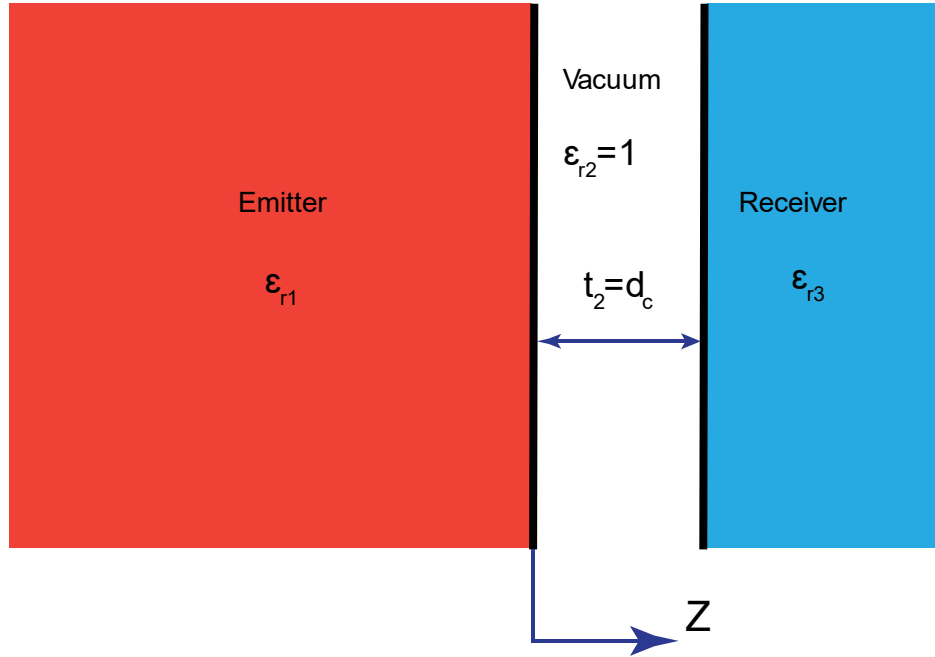
Figure 2-3: Thermal radiation inside a slab due to emitting semi-infinite body.

2.2.3. Radiative Heat Flux between Two Slabs Separated by Vacuum

For the radiative heat flux between two slabs separated by vacuum, as presented

in Figure 2-4, by substitution with appropriate Green's function components and

integrated analytically over z', the heat flux absorbed by a receiver slab can be derived

from equation (2-53). The integration over k_ρ is separated into two intervals: the first

interval $(k_\rho \leq k_v)$ represents the contribution of propagating waves in heat transfer, and

the second interval $(k_v < k_\rho < \infty)$ represents the contribution of the evanescent waves.

The total radiative heat flux absorbed is the sum of heat flux due to propagating waves q_{abs}^{prop} and evanescent waves q_{abs}^{evan} [36]:

$$q_{abs}^{prop} = \frac{\Theta(\omega, T_1)}{4\pi^2} \int_{k_\rho=0}^{k_v} \sum_{\gamma=TE,TM} \frac{\left(1 - |R_1^\gamma|^2 - |T_1^\gamma|^2\right)\left(1 - |R_3^\gamma|^2 - |T_3^\gamma|^2\right)}{\left|1 - R_1^\gamma R_3^\gamma e^{2ik_{z2}d_c}\right|^2} k_\rho dk_\rho \quad (2\text{-}56)$$

$$q_{abs}^{evan} = \frac{\Theta(\omega, T_1)}{\pi^2} \int_{k_\rho=k_v}^{\infty} \sum_{\gamma=TE,TM} \frac{Im(R_1^\gamma)Im(R_3^\gamma)}{\left|1 - R_1^\gamma R_3^\gamma e^{2ik_{z2}d_c}\right|^2} e^{-2k_{z2}''d_c} k_\rho dk_\rho \quad (2\text{-}57)$$
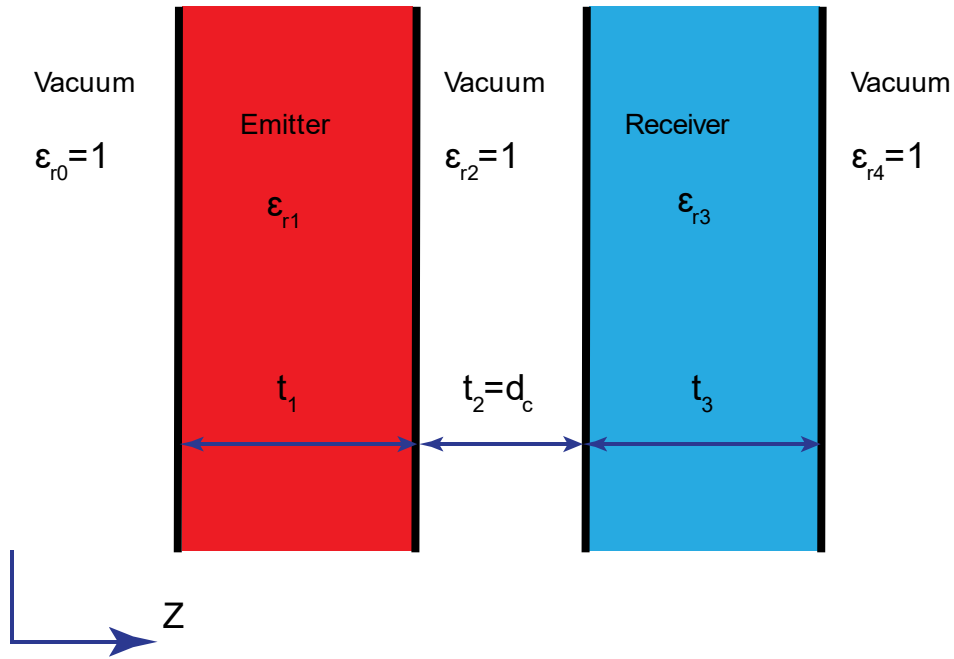
Figure 2-4: Thermal radiation between two slabs surrounded and separated by vacuum where γ represents the polarization (TE or TM), and the summation sign indicates summing the contributions from both TE and TM waves. The z component of wavevector in the vacuum k_{z2} can be calculated from

$$k_{z2} = \sqrt{k_v^2 - k_\rho^2} \quad (2\text{-}58)$$

The imaginary part of k_{z2} is k_{z2}'', and d_c is the thickness of the gap separating the two films. Reflectance and transmittance of slab 1 (i.e., emitter) and 3 (i.e., receiver) are represented by R_1, R_3, T_1 and T_3, respectively. They can be evaluated from

$$R_j^\gamma = \frac{r_{j-1,j}^\gamma + r_{j,j+1}^\gamma e^{2ik_{zj}t_j}}{1 + r_{j-1,j}^\gamma r_{j,j+1}^\gamma e^{2ik_{zj}t_j}} \tag{2-59}$$

$$T_j^\gamma = \frac{t_{j-1,j}^\gamma + t_{j,j+1}^\gamma e^{ik_{zj}t_j}}{1 + r_{j-1,j}^\gamma r_{j,j+1}^\gamma e^{2ik_{zj}t_j}} \tag{2-60}$$

where j is the media index for which reflectance and transmittance are calculated, and t_j

is the media thickness. Fresnel reflection and transmission coefficients $r_{1,2}^\gamma$ and $t_{1,2}^\gamma$,

respectively, are from media #1 (i.e., emitter) to media #2 (i.e., vacuum), and they can be

calculated from,

$$r_{1,2}^{TE} = \frac{k_{z1} - k_{z2}}{k_{z1} + k_{z2}} \tag{2-61}$$

$$r_{1,2}^{TM} = \frac{\varepsilon_{r2}k_{z1} - \varepsilon_{r1}k_{z2}}{\varepsilon_{r2}k_{z1} + \varepsilon_{r1}k_{z2}} \tag{2-62}$$

$$t_{1,2}^{TE} = \frac{2k_{z1}}{k_{z1} + k_{z2}} \tag{2-63}$$

$$t_{1,2}^{TM} = \frac{2n_1 n_2 k_{z1}}{\varepsilon_{r2}k_{z1} + \varepsilon_{r1}k_{z2}} \tag{2-64}$$

where n is the complex index of refraction, which is the square root of the complex

dielectric constant from $n = \sqrt{\varepsilon_r}$.

2.2.4. Radiative Heat Flux between Two Semi-Infinite Bodies

For the radiative heat flux between two semi-infinite bodies, as presented in

Figure 2-5, the calculations can be similar to the case of radiative heat flux between two

slabs; by finding the limit where $t_1 \to \infty$ and $t_3 \to \infty$. Consequently, the transmissivity of

both slabs will be zero (T_1^{TE}, T_1^{TM}, T_3^{TE}, and T_3^{TM}), and the Fresnel reflection coefficients

of the interfaces at $\pm\infty$ will also be zero ($r_{0,1}^{TE}$, $r_{0,1}^{TM}$, $r_{3,4}^{TE}$, and $r_{3,4}^{TM}$). The total radiative

heat flux absorbed is the sum of heat flux due to propagating waves q_{abs}^{prop} and evanescent

waves q_{abs}^{evan} [36]:

$$q_{abs}^{prop} = \frac{\Theta(\omega, T_1)}{4\pi^2} \int_{k_\rho=0}^{k_v} \sum_{\gamma=TE,TM} \frac{\left(1 - |r_{2.1}^\gamma|^2\right)\left(1 - |r_{2.3}^\gamma|^2\right)}{\left|1 - r_{2.1}^\gamma r_{2.3}^\gamma e^{2ik_{z2}d_c}\right|^2} k_\rho dk_\rho \tag{2-65}$$

$$q_{abs}^{evan} = \frac{\Theta(\omega, T_1)}{\pi^2} \int_{k_\rho=k_v}^{\infty} \sum_{\gamma=TE,TM} \frac{Im(r_{2.1}^\gamma)Im(r_{2.3}^\gamma)}{\left|1 - r_{2.1}^\gamma r_{2.3}^\gamma e^{2ik_{z2}d_c}\right|^2} e^{-2k_{z2}''d_c} k_\rho dk_\rho \tag{2-66}$$
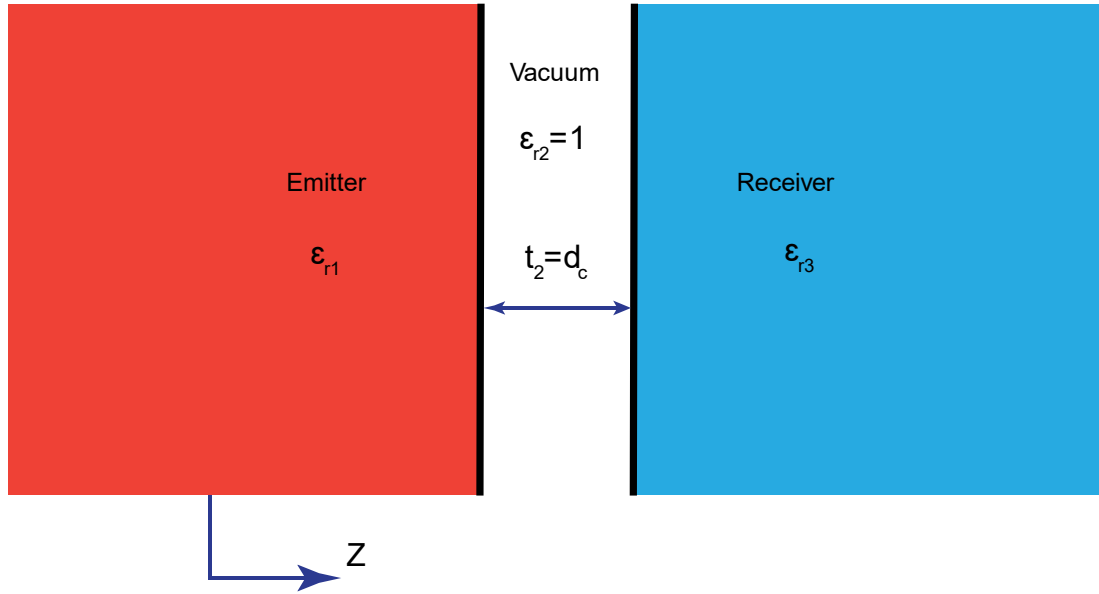
Figure 2-5:Thermal radiation between two semi-infinite bodies separated by vacuum

Chapter 3:   Thermal Calculator

The contents of this chapter have previously appeared in the following publication:

Mahmoud Elzouka contributed in the mathematical modeling of the near-field thermal radiation

3.1. Abstract

Thermal computing is a promising alternative to electronics which typically fail in harsh environments such as high temperatures and ionizing radiation. In this work, we built and simulated a thermal calculator based on thermal logic gates that can perform similar operations as their electronic counterparts. We present the design and modeling of thermal AND, OR, and NOT logic gates, achieved through the coupling between near-field thermal radiation and MEMS thermal actuation. In the process, we also developed two novel non-linear thermal expansion designs of microstructured chevron beams. These results are significant breakthroughs in the field of thermal computational science and technology as they demonstrate thermal computing at high temperatures based on demonstrated and easy to manufacture NanoThermoMechanical diodes and transistors.

3.2. Introduction

Limited performance and reliability of electronic devices at extreme temperatures, intensive electromagnetic fields, and radiation found in space exploration missions (i.e., Venus & Jupiter planetary exploration, and heliophysics missions) and earth-based applications require the development of alternative computing technologies. In the

pursuit of alternative technologies, research efforts have looked into developing thermal memory and logic devices that use heat instead of electricity to perform computations. Our group has experimentally demonstrated the world's first high-temperature thermal rectifier through near-field thermal radiation [19]. However, a rectifier is just one piece of the puzzle. Modern integrated electronic logic circuits are constructed from nonlinear and switchable electronic elements such as transistors, diodes, and switches. Similarly, thermal circuits will require nonlinear thermal components such as thermal diodes and transistors such as the ones proposed in the present work.

Any computational task can be broken down into a series of simple logic operations performed by logic gates. The basic logic gates, which are the building blocks for any logic circuit, are the AND, OR, and NOT gates. Logic states (i.e., input and output states) used in computational operations can take one of two values, namely, High or Low. The more contrast there is between the high and low values, the more robust a logic system is. Logic circuits work on the basis of current flow control using, for example, preferential flow resistance elements called diodes. Diodes are devices which allow current to pass in one direction (called the diode's forward direction), while blocking it in the opposite direction (the reverse direction). In an electrical circuit, logic states are 1 and 0 and the current is the flow of electric charges. In a thermal circuit, 1 corresponds to the high temperature (T_{max}) and 0 corresponds to the low temperature (T_{min}), while the current is represented by the heat flow.

Many designs have been proposed to realize thermal diodes, switches, transistors, and thermal logic gates [1] [2] [3]. Taking advantage of the non-linear behavior of the temperature / phase dependent thermal conductivity of certain materials, researchers have

successfully demonstrated thermal switches and regulators. Of particular interest is the use of materials such as VO_2 [4], $Ge_2Sb_2Te_5$ [5] [6], hexadecane/graphite composite materials [7], graphene [8], and $Pb(Zr, Ti)O_3$ ferroelectric [9]. Tailoring heat conduction through solid/solid and solid/liquid physical contact has also been proposed to achieve thermal switches and regulators [10] [11]. Beside conduction, convection heat transfer mechanisms have been employed to emulate thermal switches and regulators; these include jumping water droplets on superhydrophobic and superhydrophilic surfaces [12], electrowetting [13] [14], and electric field assisted evaporation [15]. Thermal radiation [19] [16] [17] [18] [20] [37], on the other hand, seems to be the most promising approach; however most of the current proposed thermal devices are limited to a small operating temperature range or specific materials. Clearly, there is enough challenge already in developing individual thermal rectifiers or diodes, seemingly making illusive the realization of an operating thermal logic circuit. This may have been true until now, as we show in this chapter the design and modeling of a full thermal adder which works over a wide range of high temperatures and with virtually any material. This new development is an extension of our Near-Field Thermal Radiation (NFTR) based NanoThermoMechanical diode [19]. Here, we extend the concept to design thermal logic AND, OR, and NOT gates. We show the stability of NanoThermoMechanical logic gates and their ability to be clustered and used in a full thermal logic operator to perform complex operations.

3.3. Mathematical Modeling of the Near-Field Thermal Radiation

Near-field thermal radiation is a mode of transferring heat via thermal radiation between two surfaces, which occurs when the vacuum gap separating them becomes

comparable to the radiation wavelength. The NFTR between two planar surfaces is calculated using the following formalism [38, 39]:

$$Q_{1\to2}(T_1, T_2, L) = \int_0^\infty \frac{d\omega}{2\pi} [\Theta(\omega, T_1) - \Theta(\omega, T_2)]\tau_{1\to2}(\omega, L) \tag{3-1}$$

$$\Theta(\omega, T) = \frac{\hbar\omega}{\exp\left(\frac{\hbar\omega}{k_bT}\right) - 1} \tag{3-2}$$

where $\Theta(\omega, T)$ is the energy of harmonic oscillatoar at frequency ω and temperature T, $\hbar$ is the circular Planck's constant, k_b is the Boltzmann constant, and $\tau_{1\to2}(\omega, L)$ is the spectral transmissivity in radiative transfer between the two planar surfaces separated by L. The spectral transmissivity is given by,

$$\tau_{1\to2}(\omega, L) = \int_0^\infty \frac{k_p dk_p}{2\pi} \xi(\omega, k_p) \tag{3-3}$$

where k_p is the parallel component of the wavevector and $\xi(\omega, k_p)$ is the energy transmission coefficient, and it is defined by equation (3-4) for propagating waves and (3-5) for evanescent waves:

$$\xi(\omega, k_p \le \omega/c) = \sum_{\mu=s,p} \frac{\left(1 - \left|\tilde{R}_1^{(\mu)}\right|^2\right)\left(1 - \left|\tilde{R}_2^{(\mu)}\right|^2\right)}{\left|1 - \tilde{R}_1^{(\mu)}\tilde{R}_2^{(\mu)}e^{2jk_zL}\right|^2} \tag{3-4}$$

$$\xi(\omega, k_p > \omega/c) = \sum_{\mu=s,p} \frac{4Im\left(\tilde{R}_1^{(\mu)}\right)Im\left(\tilde{R}_2^{(\mu)}\right)e^{-2|k_z|L}}{\left|1 - \tilde{R}_1^{(\mu)}\tilde{R}_2^{(\mu)}e^{-2|k_z|L}\right|^2} \tag{3-5}$$

where $\tilde{R}_1^{(\mu)}$ and $\tilde{R}_2^{(\mu)}$ are polarization dependent reflection coefficients of the two half spaces, $\mu = s$ (or p) refers to transverse electric (or magnetic) polarization, and k_z is the z-component of the wavevector in vacuum, where z is the direction normal to the two planar surfaces. Using a gold surface as an example, the dielectric function for the gold

follows the Drude model given by $\varepsilon(\omega) = \varepsilon_\infty - \frac{\omega_p{}^2}{\omega^2 - j\omega\Gamma}$, where $\omega_p = 9\,[eV] =$

$1.3673e + 16\,[rad/s]$ is the plasma frequency, $\Gamma = 35\,[eV] = 5.3174e + 13[rad/s]$

is the collision frequency or frictional coefficient, and $\varepsilon_\infty = 1$. Figure 3-1 shows the net

radiative heat transfer between two gold surfaces as a function of a separation gap. As

can be seen from the figure, NFTR's intensity has an accelerated increase with decreasing

a separation gap. The increased NFTR intensity results from the tunneling of the

evanescent surface waves between the two surfaces at separation gaps below $0.5\,\mu m$

[40].
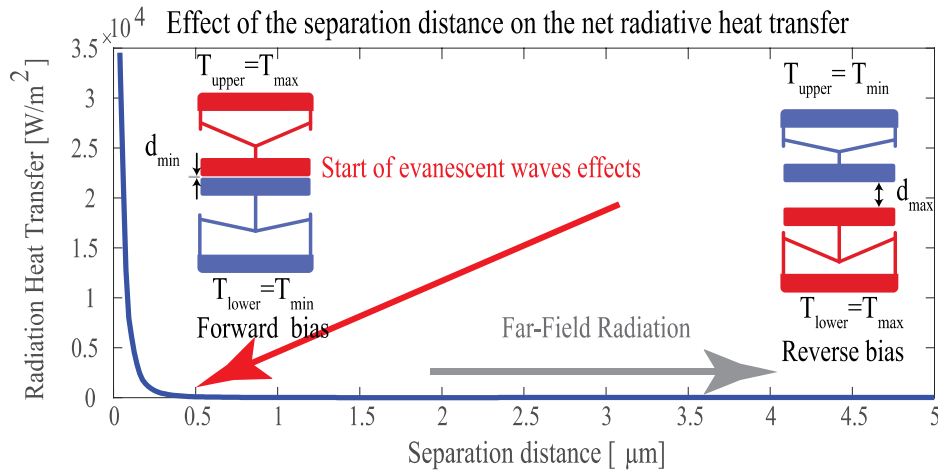
Figure 3-1: Effect of the separation distance between two gold terminals on the net radiative heat transfer.

3.4. Thermal Diode

As mentioned herein-before, diodes are the building blocks of logic gates. To

create a thermal diode, we need to control the resistance of heat flow in response to heat

flow direction. In our previous work [19], we achieved rectification through the coupling

between NFTR and the size of a micro/nano gap separating two terminals engineered

(e.g., MEMS thermal expansion) to be a function of heat flow direction. As shown in

Figure 3-2, the thermal diode consists of two terminals (upper and lower). Initially, both terminals are at low temperatures, T_{min}, separated by a spacing, d_{ini}, large enough to suppress any near-field radiative heat transfer. The gap also remains the same as both terminals are set to T_{max}. In the forward bias, the upper and lower terminal temperatures are set to T_{max} and T_{min}, respectively. This causes the upper terminal to move downward, effectively reducing the separation gap and significantly increasing the heat transfer rate through NFTR. By reversing the heat flow direction and by switching the temperatures of the terminals (i.e., reverse bias), the terminals move farther apart from each other and therefore reduce the heat transfer rate, effectively achieving thermal rectification.
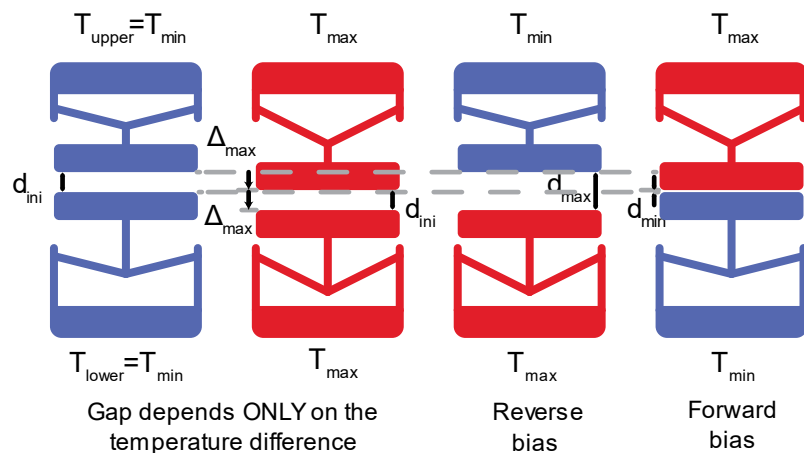
Figure 3-2: Schematic drawing of a NFTR thermal diode.

3.5. NanoThermoMechanical AND Logic Gate

Using the thermal diode described above, thermal logic gates can be built. Figure 3-9 shows the analogy between electronic and thermal logic AND gates based on diodes. A Simple logic AND gate takes two logic inputs, A and B, and returns an output C. Based on the AND gate 'truth table', the gate output is 1 (i.e., T_{max} for the thermal gate) only if both inputs are 1's (T_{max}), otherwise it will return an output as 0 (T_{min}). The

electrical resistance between the source (i.e., the heat source in a thermal gate) and the output terminal C is analogous to a conductive resistance.
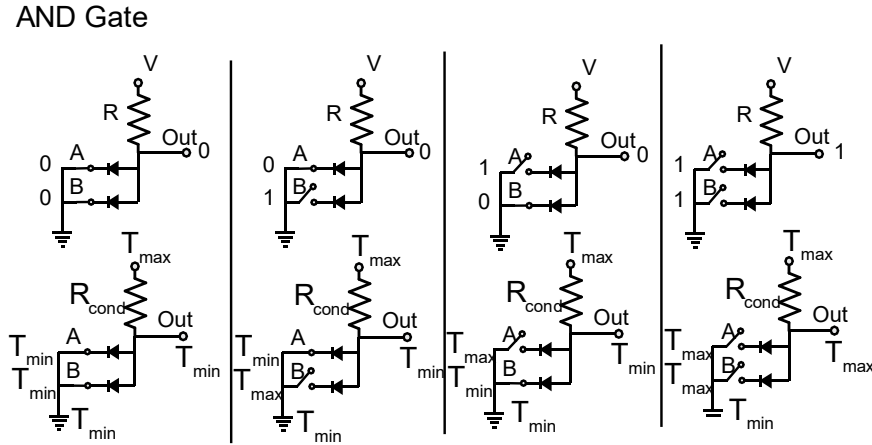
AND Gate

Figure 3-3: Analogy between electronic and thermal logic AND gates.

Based on the fore mentioned principles, a thermal AND gate is constructed using a combination of two thermal diodes and a fixed-value conduction thermal resistance as shown in Figure 3-4. The upper terminals of the two thermal diodes are connected together to a fixed conductive resistance (i.e., solid beams with tailored thermal conductance) which is connected to the heat source. The temperature of each of the lower terminals of the thermal diodes can be controlled independently by choosing to connect the terminals to either the heat source (T_{max}) or the heat sink (T_{min}). The temperature of the output terminal C is a result of the heat balance between the inward heat flow from the heat source and the outward heat flows to the lower input terminals (A and B). The heat balance at C is given by:

$$Q_{cond,S \to C} = Q_{rad,C \to A} + Q_{rad,C \to B} \qquad (3\text{-}6)$$

$$T_C = T_{max} - \frac{\left(Q''_{rad,C \to A} + Q''_{rad,C \to B}\right)}{\dfrac{kA_{cond}}{LA_{rad}}} \qquad (3\text{-}7)$$

where

$$Q_{cond,S \to C} = \frac{kA_{cond}}{L}(T_{max} - T_C) \tag{3-8}$$

$$Q''_{rad,C \to A}(T_C, T_A, \Delta_{CA}) \tag{3-9}$$

$$= \int_0^\infty \frac{d\omega}{2\pi}[\Theta(\omega, T_C) - \Theta(\omega, T_A)]\tau_{C \to A}(\omega, \Delta_{CA})$$

$$Q''_{rad,C \to B}(T_C, T_B, \Delta_{CB}) \tag{3-10}$$

$$= \int_0^\infty \frac{d\omega}{2\pi}[\Theta(\omega, T_C) - \Theta(\omega, T_B)]\tau_{C \to B}(\omega, \Delta_{CB})$$

where $Q_{cond,S \to C}$ is the conductive heat transfer from the heat source to the output

terminal C; $Q_{rad,C \to A}$ is the radiative heat transfer between C and A terminals in the first

thermal diode; $Q_{rad,C \to B}$ is the radiative heat transfer between C and B terminals in the

second thermal diode; k, A_{cond}, and L are the thermal conductivity, cross sectional area,

and length of the rods that connect the heat source and output terminal C, respectively;

and Δ_{CA} and Δ_{CB} are the separation distances between output terminal C and input

terminals A and B, respectively.
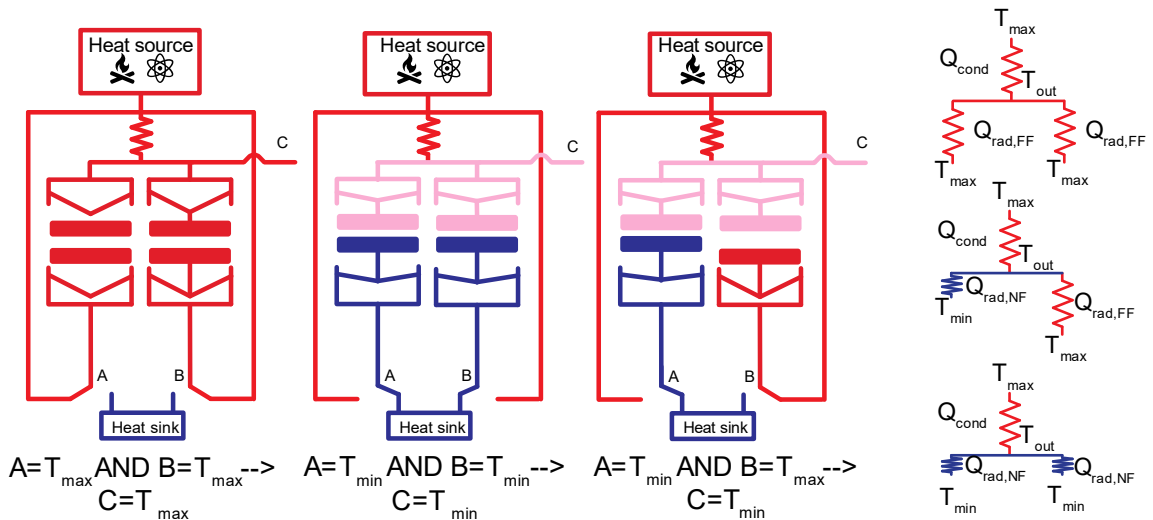
Figure 3-4: Schematic drawing and thermal circuit of the proposed thermal logic AND

gate by employing the linear (monotonic) thermal expansion of the terminals.

Using a linear thermal expansion of silicon V-shaped chevron beams, Figure 3-5

shows the effect of the $\frac{kA_{cond}}{LA_{rad}}$ conductance design parameter on the temperature of the

output terminal C for the three cases of the thermal logic AND gate operated between

$T_{max} = 700\ K$ and $T_{min} = 600\ K$. When both inputs are at T_{max}, the output is at T_{max} as

expected. However, when one of the inputs is at T_{min}, the temperature of the output

thermal remains significantly higher than T_{min}. We define the effectiveness, ϵ, of the

thermal logic AND gate as,

$$\epsilon = \frac{T_c - T_{min}}{T_{max} - T_{min}} \tag{3-11}$$

An ideal thermal logic AND gate should demonstrate $\epsilon = 0$ for all cases except

when both inputs are at T_{max}, for which case ϵ should be ideally equal to 1. The results in

Figure 3-5 show that the proposed thermal AND gate does not achieve, efficiently (i.e.,

$\epsilon = 0.43$ when both inputs are at T_{min}), the required output from the gate. Additionally,

as the conductance between the heat source and the output terminal C increases, the logic

AND gate deviates further from its truth table.
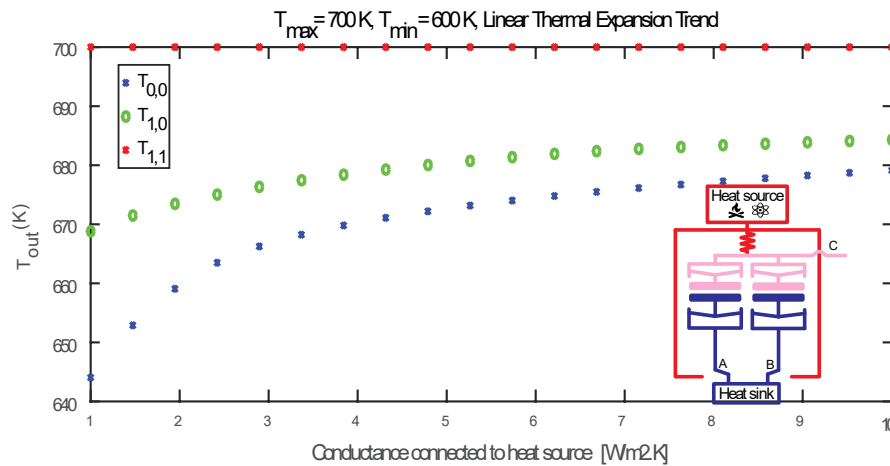
Figure 3-5: Effect of the conductance parameter on the thermal logic AND gate in the

case of linear thermal expansion.

The reason for the failure to achieve the required functionality of the proposed thermal AND gate is the direct result of the heat balance (conduction from source, radiation with A, and radiation with B). For example, if $T_A = T_{min} \ or \ T_B = T_{min}$, we find that $T_C < T_{max}$, and this is because the separation distance between the diode's terminals C, and A or B, is not at its minimum separation distance to achieve near-field radiation. Likewise, if $T_A = T_{max} \ or \ T_B = T_{max}$, we find that $T_C > T_{min}$, and this is because the separation distance between the terminals C, and A or B, is not at its maximum separation distance to achieve far field radiation. To resolve these two problems, the output upper terminal C needs to be at its bottom position when $T_A = T_{min} \ or \ T_B = T_{min}$, regardless of terminal C temperature. In addition, terminals A and B need to be relatively far away from terminal C when $T_A = T_{max} \ or \ T_B = T_{max}$, regardless of terminal C temperature. To achieve the above-mentioned characteristics, both upper and lower terminals need to be designed to feature non-monotonic thermal expansions.

Figure 3-6 shows schematic drawings of the modified thermal AND gate at room temperature, minimum operating temperature, and maximum operating temperature. The upper terminal is designed to feature a reduced ($\frac{\beta}{\alpha} < 1$) thermal expansion while the lower terminals experience amplification ($\frac{\beta}{\alpha} > 1$) between T_{min} and T_{max}. We achieved the required thermal expansion mechanisms as shown in

Figure *3-7* using novel and ingenious chevron mechanisms consisting of spring-assisted reduction and cascading chevrons amplification for the lower and upper terminals, respectively. To ensure the structural integrity of the proposed chevron design, Finite Element Analysis simulations were carried out using COMSOL Multiphysics® over the range of expected operating temperatures. Results of the mechanical stresses for

both the upper and lower terminals show that the calculated stresses are safely below the

mechanical failure limit of the silicon chevrons. Figure 3-8 shows the results for the

modified thermal logic AND gate using the above described chevron thermal expansion

profiles. As can be seen from the results, we were able to successfully develop a thermal

logic AND gate with effectiveness, ϵ, between 0.01 and 0.1 (for highest studied

conductance).
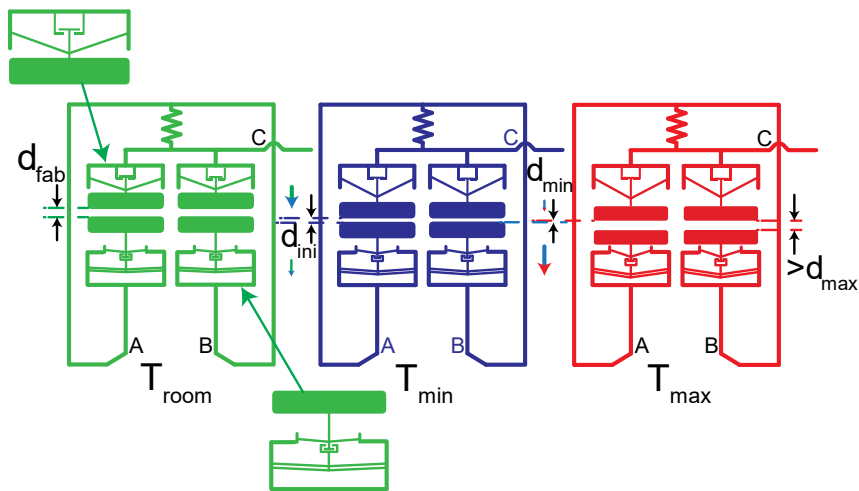
Figure 3-6: Schematic drawings of the thermal logic AND gate at different operating

temperatures with a reducing expansion mechanism for the upper terminal and

amplification expansion mechanism for the lower terminals.
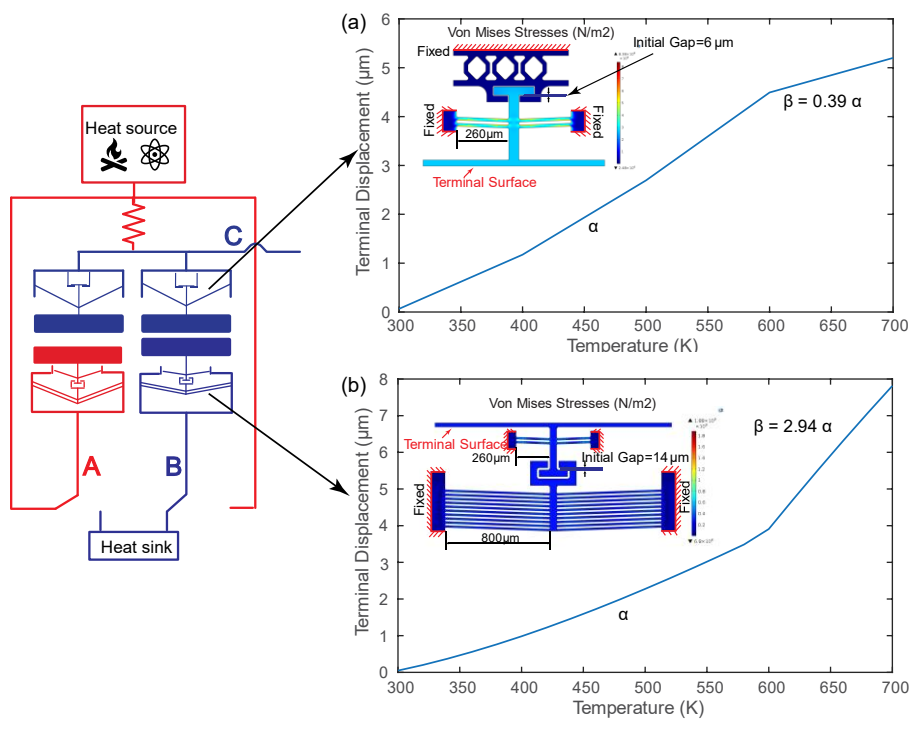
Figure 3-7: The von Mises stresses and displacement as a function of temperature for the non-linear thermal expansion mechanisms: (a) the reducing and (b) the amplification expansion mechanisms.
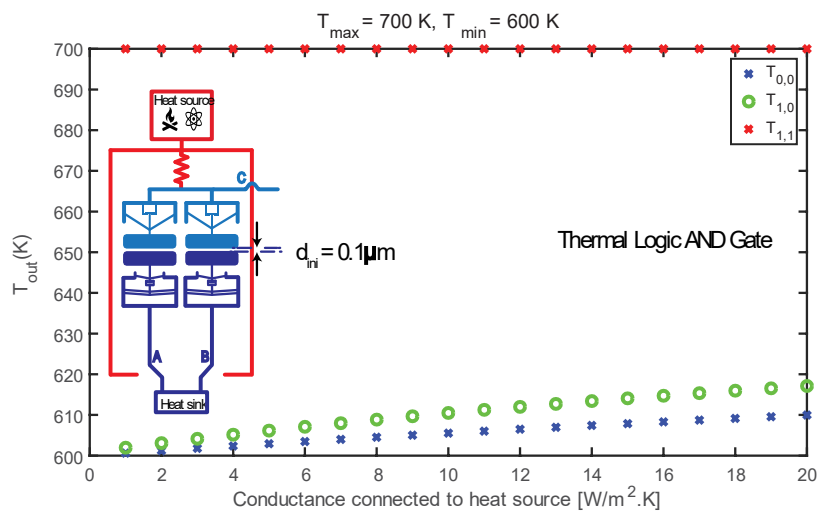
Figure 3-8: Effect of the conductance parameter on the modified thermal logic AND gate employing a reducing expansion mechanism for the upper terminal and amplification expansion mechanism for the lower terminals.

3.6. NanoThermoMechanical OR Logic Gate

Figure 3-9 shows the analogy between electronic and thermal logic OR gates based on diodes. A simple logic OR gate takes two logic inputs, A and B, and returns an output C. Based on the OR gate 'truth table', the gate output is 1 (i.e., T_{max} for thermal gate) if any of the input terminals is 1 (T_{max}), otherwise it will return an output of 0 (T_{min}). The electrical resistance between the ground (i.e., the heat sink in a thermal gate) and the output terminal C is analogous to a conductive resistance.
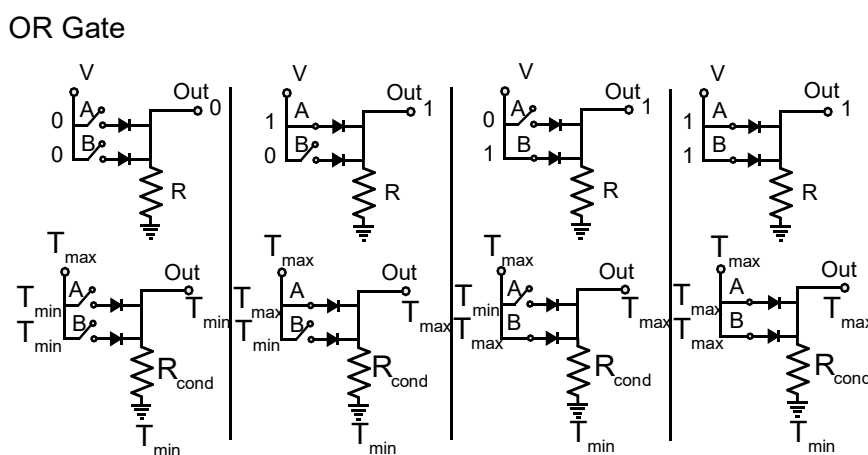
Figure 3-9: Analogy between electronic and thermal logic OR gates.

Figure 3-10 shows a thermal OR gate that is constructed using a combination of two thermal diodes and a fixed-value conduction thermal resistance. The lower terminals of the two thermal diodes are connected together to a fixed conductive resistance (i.e., solid beams with tailored thermal conductance), which is connected to the heat sink. The temperature of each of the upper terminals (inputs) of the thermal diodes can be controlled independently by choosing to connect the terminals to either the heat source (T_{max}) or the heat sink (T_{min}). The upper terminals are designed using a linear thermal expansion of silicon V-shaped chevron beams, while the lower terminals are fixed. The temperature of the output terminal C is a result of the heat balance between the inward

heat flows from the upper input terminals A and B and the outward heat flow to the heat sink. The heat balance at C is given by:

$$Q_{cond,C \to S} = Q_{rad,A \to C} + Q_{rad,B \to C} \tag{3-12}$$

$$T_C = T_{min} + \frac{\left(Q''_{rad,A \to C} + Q''_{rad,B \to C}\right)}{\dfrac{kA_{cond}}{LA_{rad}}} \tag{3-13}$$

where

$$Q_{cond,C \to S} = \frac{kA_{cond}}{L}(T_C - T_{min}) \tag{3-14}$$

$$Q''_{rad,A \to C}(T_A, T_C, \Delta_{AC}) \tag{3-15}$$

$$= \int_0^\infty \frac{d\omega}{2\pi} [\Theta(\omega, T_A) - \Theta(\omega, T_C)]\tau_{A \to C}(\omega, \Delta_{AC})$$

$$Q''_{rad,B \to C}(T_B, T_C, \Delta_{BC}) \tag{3-16}$$

$$= \int_0^\infty \frac{d\omega}{2\pi} [\Theta(\omega, T_B) - \Theta(\omega, T_C)]\tau_{B \to C}(\omega, \Delta_{BC})$$

where $Q_{cond,C \to S}$ is the conductive heat transfer from the output terminal C to the heat sink, $Q_{rad,A \to C}$ is the radiative heat transfer between A and C terminals in the first thermal diode, $Q_{rad,B \to C}$ is the radiative heat transfer between B and C terminals in the second thermal diode, and Δ_{AC} and Δ_{BC} is the separation distance between output terminal C and input terminals A and B, respectively.
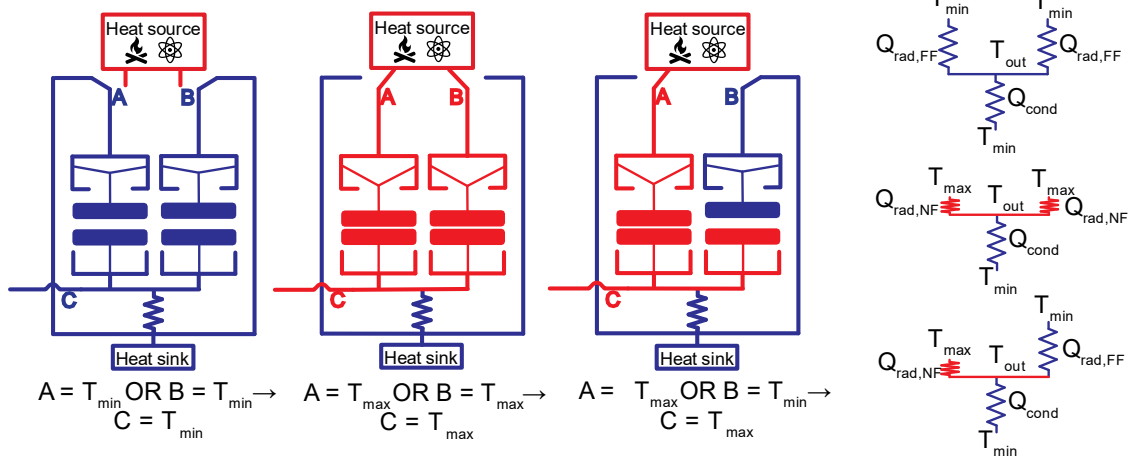
Figure 3-10: Schematic drawing and thermal circuit of the proposed thermal logic OR gate.

Figure 3-11 shows the effect of the $\frac{kA_{cond}}{LA_{rad}}$ conductance design parameter on the temperature of the output terminal C for the three cases of the thermal logic OR gate operated between $T_{max} = 700\,K$ and $T_{min} = 600\,K$. Based on the effectiveness of the thermal logic gate defined in equation (3-11), an ideal thermal logic OR gate should demonstrate $\epsilon = 1$ for all cases except when both inputs are at T_{min}, for which case ϵ should be ideally equal to 0. The results in Figure 3-11 show that we successfully developed a thermal logic OR gate with effectiveness, ϵ, between 0.97 (for highest studied conductance) and 0.995, for the cases when any input is at T_{max}.
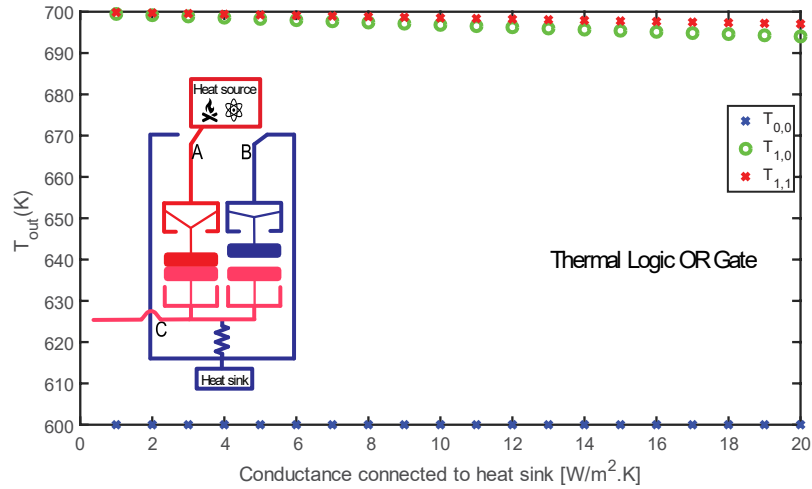
Figure 3-11: Effect of the conductance parameter on the thermal logic OR gate.

3.7. NanoThermoMechanical NOT Logic Gate

The logic NOT gate implements logical negation, which inverts the input signal of the gate. Figure 3-12 shows a schematic drawing of the designed thermal NOT gate consisting of a heat source supported by silicon V-shaped chevron beams, a fixed heat sink, and two silicon V-shaped chevron beams to support the output terminal. These two chevrons are at the input temperature; the thermal expansion of the input chevrons is based on the input temperature of the thermal NOT gate. The output terminal is connected to a fixed conductive resistance, which is connected to the input chevrons. The heat balance at the output is given by:

$$Q_{rad,O \to L} = Q_{cond,I \to O} + Q_{rad,H \to O} \tag{3-17}$$

$$T_O = T_I - \frac{\left(Q''_{rad,O \to L} - Q''_{rad,H \to O}\right)}{\frac{kA_{cond}}{LA_{rad}}} \tag{3-18}$$

where

$$Q_{cond,I \to O} = \frac{kA_{cond}}{L}(T_O - T_I) \tag{3-19}$$

$$Q''_{rad,O \to L}(T_O, T_L, \Delta_{OL}) \tag{3-20}$$

$$= \int_0^\infty \frac{d\omega}{2\pi} [\Theta(\omega, T_O) - \Theta(\omega, T_L)] \tau_{O \to L}(\omega, \Delta_{OL})$$

$$Q''_{rad,I \to O}(T_I, T_O, \Delta_{IO}) = \int_0^\infty \frac{d\omega}{2\pi} [\Theta(\omega, T_I) - \Theta(\omega, T_O)] \tau_{I \to O}(\omega, \Delta_{IO}) \tag{3-21}$$

where $Q_{cond,I \to O}$ is the conductive heat transfer from the input chevrons to the output

terminals, $Q_{rad,O \to L}$ is the radiative heat transfer between the output terminal and the heat

sink, $Q_{rad,H \to O}$ is the radiative heat transfer between the heat source and the output

terminal, and Δ_{OL} and Δ_{IO} are the separation distances between the output terminal and

the heat sink and source, respectively.
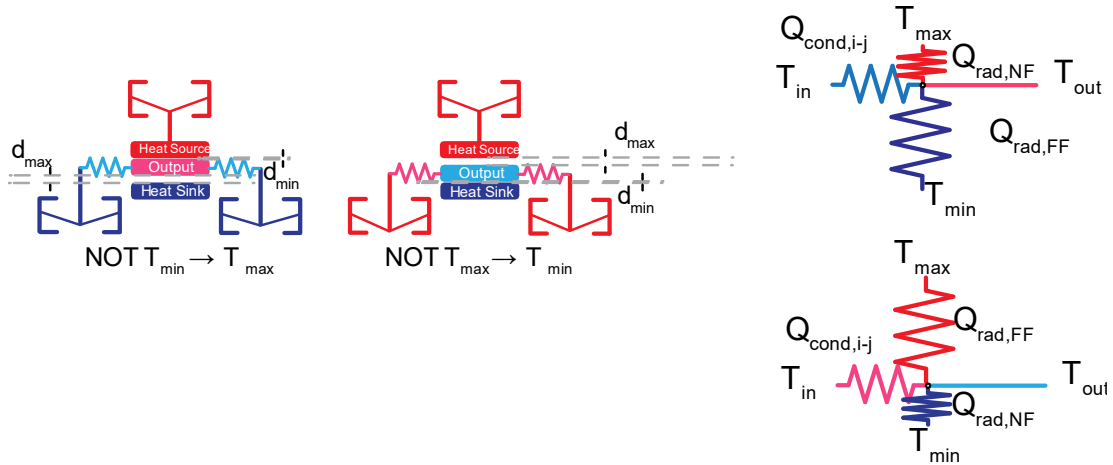
Figure 3-12: Schematic drawing and thermal circuit of the proposed thermal logic NOT

gate.

Figure 3-13 shows the effect of the $\frac{kA_{cond}}{LA_{rad}}$ conductance design parameter on the

temperature of the output terminal for the two cases of the thermal logic NOT gate

operated between $T_{max} = 700\ K$ and $T_{min} = 600\ K$. An ideal thermal logic NOT gate

should demonstrate $\epsilon = 1$ when the input is at T_{min}, and $\epsilon = 0$ when the input is at T_{max}.

The results in Figure 3-13 show that we successfully developed a thermal logic NOT gate

with effectiveness, ϵ, between 0 and 0.03, when the input is at T_{max}, and ϵ between 0.97 and 1, when the input is at T_{min}.
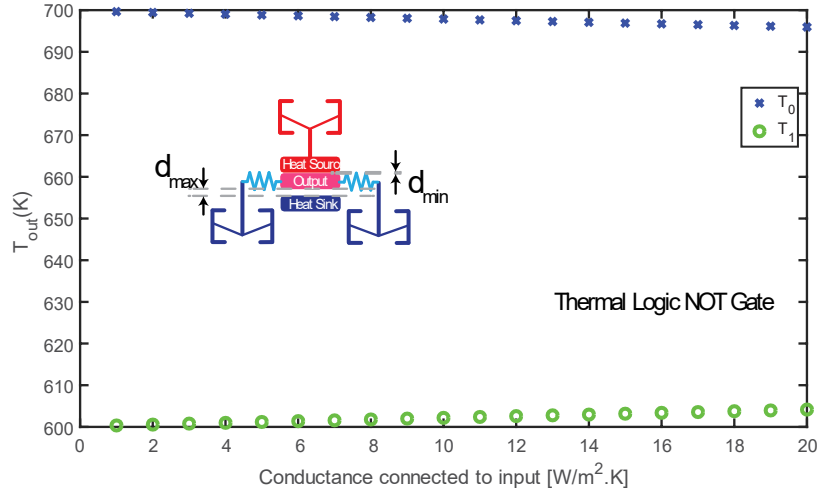
Figure 3-13: Effect of the conductance parameter on the thermal logic NOT gate.

3.8. NanoThermoMechanical Calculator

The successful design of basic thermal logic gates (i.e., AND, OR, and NOT gates) paves the way to develop full thermal logic circuits. Here, we present the design and simulation of a thermal calculator based on binary mathematical computations. The basis of the binary mathematical computations is the full adder, whose inputs are two binary bits and a carry-in bit, and its outputs are a sum bit and carry-out bit. Figure 3-14 shows the schematic drawing of the designed thermal full adder, which is a combination of AND, OR and XOR gates. Table 1 shows the results of creating a thermal full adder based on $T_{max} = 700\ K$, $T_{min} = 600\ K$ and a conductance parameter of $1\ W/m^2.K$; the table compares the results with an ideal full adder. By determining the high and low logic states by specified thresholds, 'high' state represents $T > T_{max} - 0.25(T_{max} - T_{min})$ and 'low' state represents $T < T_{min} + 0.25(T_{max} - T_{min})$. Table 3-1 indicates the successful development of the thermal adder.
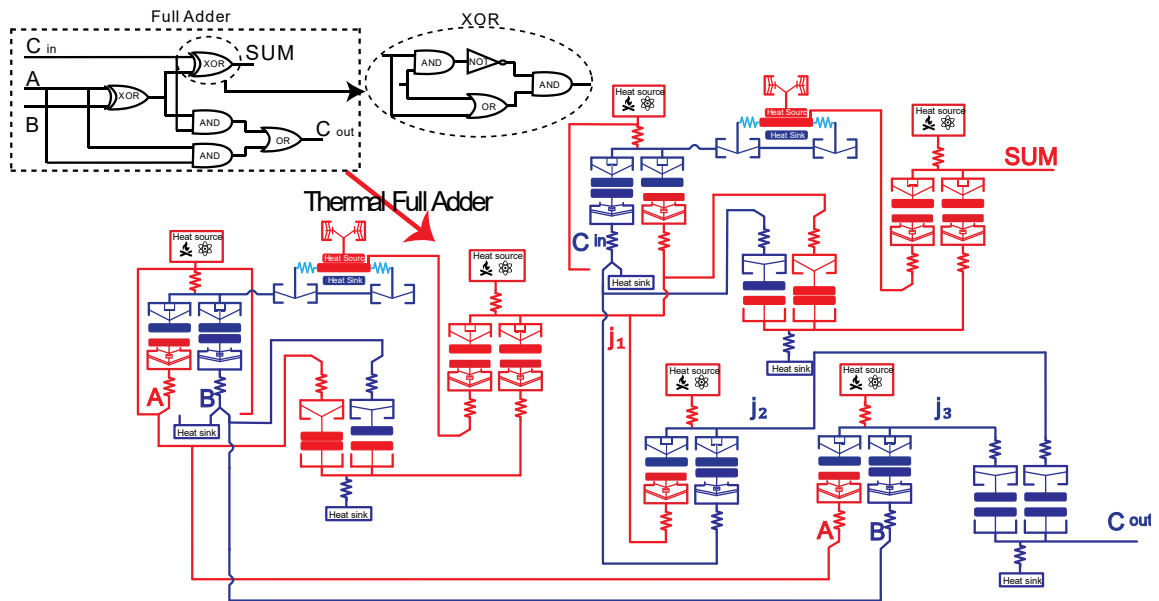
Figure 3-14: Schematic drawing of the thermal full adder.

Table 3-1: The 'Truth Table' for an electrical and a thermal full adder; units of temperatures are in degree Kelvin.

Electrical full adder					Thermal full adder				
A	B	C_{in}	SUM	C_{out}	A	B	C_{in}	SUM	C_{out}
0	0	0	0	0	600	600	600	603.4	600.7
0	0	1	1	0	600	600	700	690.2	601.8
0	1	0	1	0	600	700	600	696.2	601.5
0	1	1	0	1	600	700	700	603.1	698.0
1	0	0	1	0	700	600	600	696.2	601.5
1	0	1	0	1	700	600	700	603.1	698.0
1	1	0	0	1	700	700	600	603.5	699.5
1	1	1	1	1	700	700	700	688.0	699.5

Next, we developed a thermal calculator to perform the addition of two decimal numbers. Figure 3-15 shows a schematic drawing of the full thermal calulator performing the addition of 154 and 433. These decimal numbers are first converted to thermal binaries (i.e., 1 ≡ High temperature or H; 0 ≡ Low temperature or L) resulting in HLLHHLHL and HHLHHLLLH thermal binary numbers, respectively [41]. The sum of these two thermal binary numbers is the thermal binary number HLLHLLHLHH (1001001011), which is equivalent to decimal number 587.
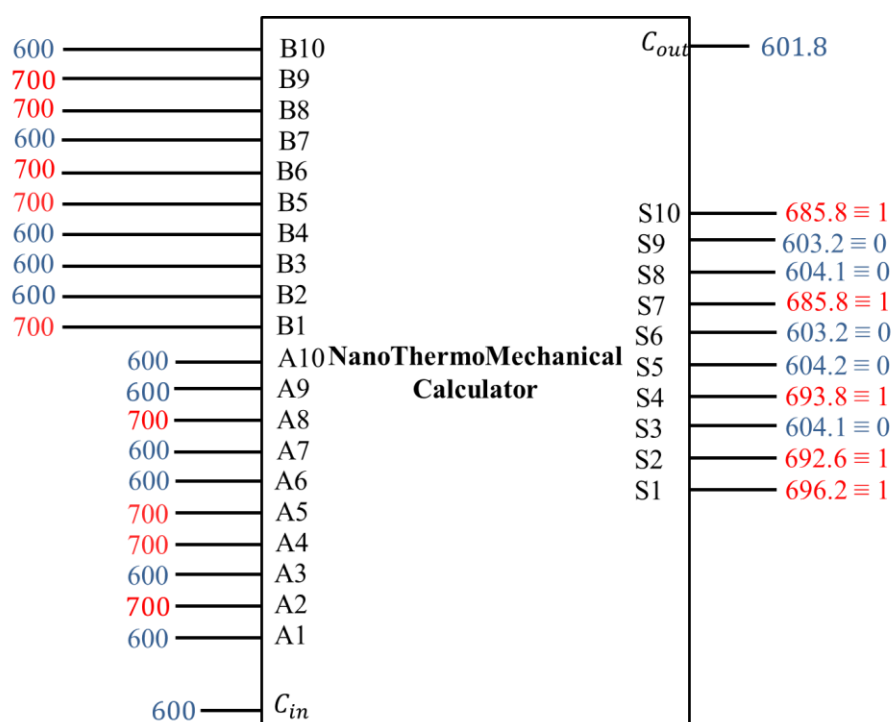
Figure 3-15: Schematic drawing of the NanoThermoMechanical calculator including a series of thermal full adders.

3.9. Conclusions

In this chapter, we introduced the basic building blocks of the thermal computation technology. We introduced the design and modeling of NanoThermoMechanical AND, OR and NOT logic gates achieved through the coupling

between near-field thermal radiation and MEMS thermal actuation. In the process, NanoThermoMechanical AND logic gate requires nonlinearity in the terminals' thermal displacement. We introduced the design of the two non-linear mechanisms using novel and ingenious chevron mechanisms consisting of spring-assisted reduction and cascading chevrons amplification for the output and the input terminals, respectively. The successful design of the basic thermal logic gates, which paves the way to develop full thermal logic circuits (i.e., thermal calculator). The results are significant breakthroughs in thermal computing science & technology as they demonstrate thermal computing at high temperatures based on demonstrated and easy to manufacture NanoThermoMechanical diodes and transistors.

3.10. Acknowledgments

Chapter 4:   Nonlinear Thermal Expansion of MEMS Chevron

The contents of this chapter have been submitted for publication in Journal of MicroElectroMechanical Systems.

4.1. Abstract

Today's electronics cannot perform in harsh environments (e.g., elevated temperatures and ionizing radiation environments) found in many engineering applications. Thermal computing, data processing based on heat instead of electricity, is proposed as a practical alternative and opens a new scientific area at the interface between thermal and computational sciences. Previously, we presented the design and modeling of a NanoThermoMechanical AND logic gate, achieved through the coupling between near-field thermal radiation and MEMS thermal actuation [42]. In the process, we developed two novel non-linear thermal expansion designs of microstructure silicon V-shaped chevron beams which were required to achieve the desired thermal AND gate operation. In this work, we introduce the design, fabrication, and characterization of the two non-linear mechanisms using novel and ingenious chevron mechanisms consisting of spring-assisted reduction and cascading chevrons amplification for the reducing and the amplification mechanisms, respectively. The results show non-linearity can be achieved successfully through demonstrated and easy-to-manufacture chevron mechanisms.

4.2. Introduction

Many engineering applications performed in harsh environments, such as intensive electromagnetic fields, radiation found in space exploration missions (i.e., Venus & Jupiter

planetary exploration, and heliophysics missions), and earth-based applications, require the development of alternative computing technologies. Developing thermal logic devices that use heat instead of electricity to perform computations is proposed as a practical solution. Our research group invented a thermal rectifier through the coupling of near-field thermal radiation (NFTR) in a vacuum and thermal actuation of a V-shaped (chevron beams) actuator [19]. The NFTR transfers heat via thermal radiation between two surfaces separated by a very small vacuum gap (i.e., comparable to the radiation wavelength). NFTR's intensity exponentially increases with a decreasing separation gap. The increased NFTR intensity results from the tunneling of the evanescent surface waves between the two surfaces at separation gaps below 0.5 μm [42]. We extended this concept to build and simulate a thermal calculator based on NanoThermoMechanical logic gates that can perform similar operations as their electronic counterparts, achieved through the coupling between near-field thermal radiation and MEMS thermal actuation. In the process, we developed two novel non-linear thermal expansion designs of microstructured chevron beams: the reducing and the amplification expansion mechanisms [42].

Thermal actuators have been demonstrated to be compact, stable, producing large actuation force, requiring low operating voltage, simple in design and integration, and easily microfabricated [43] [44]. Hence in the field of microelectromechanical systems (MEMS), thermal actuators have been used in applications such as micro grippers [45] [46] [47] [48] [49] [50] [51] [52], switches [53] [54] [55], relays [56], resonators [57], chemical [58] and physical [59] sensors, nanopositioners [60], in-situ microscopy [61] [62] , and thermal rectifier [19]. Thermal actuation is based on thermal expansion due to applying heat to the actuator, so the strain in the actuator is transduced to mechanical displacement

by the structure and configuration of the thermal actuator. Many configurations have been proposed in the literature, these include U-shape [56] [63] [64] [65], V-shape [19] [43] [51] [53] [54] [55] [60] [62] [66] [67], Z-shape [44] [68] [69], and compliant actuators [70] [71].

Non-linearity in actuation of MEMS devices are essential in many applications, such as a self-regulating valve at certain temperatures [70], bandwidth-tolerant vibration energy harvesting [72], and an electrostatic kinetic energy harvester [73]. Hence, various studies have introduced nonlinear actuators in a variety of configurations such as: thermal buckling of nickel beams [70], and nonlinear or softening springs [72] [73] [74]. Our non-linear thermal expansion mechanisms were achieved using novel and ingenious chevron mechanisms consisting of spring-assisted reduction and cascading chevrons amplification. In this chapter, we introduce the design, fabrication, and characterization of these two novel non-linear thermal expansion mechanisms. The results demonstrate the capability of achieving non-linear expansion based on easy-to-design and easy-to-manufacture microstructured chevron beams. In addition, the microstructures can be tailored to achieve non-linearity with different degrees and at different desired conditions.

4.3. Design and Modeling

Based on the concept of coupling NFTR and thermal actuation of a chevron beam actuator, a thermal AND gate can be constructed using a combination of two thermal diodes and a fixed-value conduction thermal resistance (i.e., solid beams with tailored thermal conductance) as shown in Figure 4-1 [42]. The upper terminals (output) of the two thermal diodes are connected together to a fixed conductive resistance, which is connected to the heat source. Consequently, the temperature of the output terminal C is a result of the heat

balance between the inward conduction heat flow from the heat source (Q_{cond}) and the outward radiation heat flows ($Q_{rad,NF}$ or $Q_{rad,FF}$) to the lower input terminals (A and B). To achieve the required functionality of the AND gate, output upper terminal C needs to be at its bottom position when $T_A = T_{min}$ or $T_B = T_{min}$, regardless the temperature of terminal C, to achieve the minimum separation distance between terminals (i.e., near-field thermal radiation). In addition, terminals A and B need to be separated by large enough gap from terminal C (i.e., far-field thermal radiation) when $T_A = T_{max}$ or $T_B = T_{max}$, regardless the temperature of terminal C. In other words, nonlinearity in the terminals' thermal displacement is required. The upper terminal (output) of the thermal AND gate must feature a reducing $\left(\frac{\beta}{\alpha} < 1\right)$ thermal expansion while the lower terminals (inputs) must experience amplification $\left(\frac{\beta}{\alpha} > 1\right)$ as illustrated in the ideal schematic shown in Figure 4-1. α represents the displacement rate of the terminal between T_{room} and T_{min}, and β is the displacement rate of the terminal between T_{min} and T_{max}.
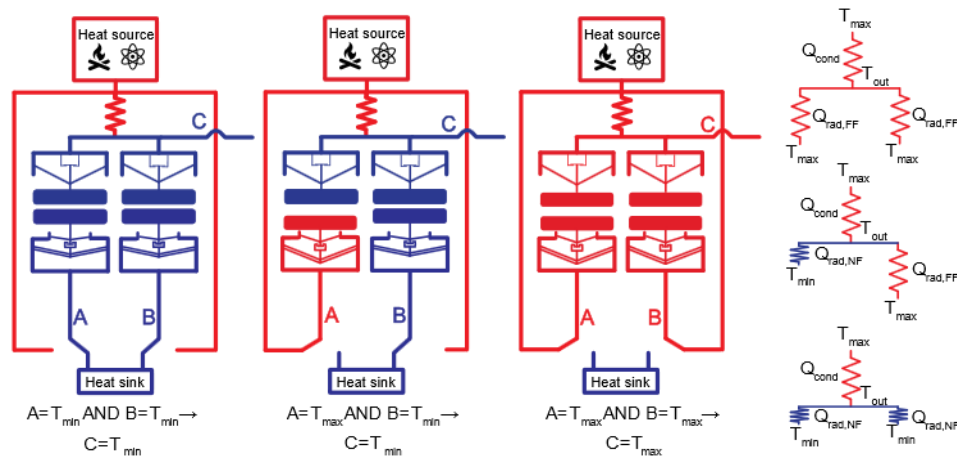

Figure 4-1: Schematic drawing of the thermal AND logic gate with reducing expansion mechanism for the upper terminal and amplification expansion mechanism for the lower terminals.

The reducing mechanism can be achieved by spring-assisted chevron beams. The terminal surface is connected to the chevron beams and separated by a small gap from a spring-loaded stopper. Through initial heating, the terminal surface is displaced downwards with a certain expansion rate α due to the thermal expansion of the chevron beams. Further heating to a certain designed temperature, the chevron comes in contact with the spring-loaded structure which reduces the expansion rate of the terminal surface to β $(\beta < \alpha)$ proportional to the spring constant and effectively achieving the desired reducing mechanism. As for the amplification mechanism, it can be achieved via two interlocked cascading chevrons with different arm lengths and separated by a small gap. The terminal surface is connected to the short arms chevron. Through heating, the terminal surface is displaced downwards with a certain expansion rate α, smaller than the expansion rate of the long arms chevron. Further heating to a certain designed temperature causes the two chevrons to interlock and for the terminal surface to expand at a higher rate β, $(\beta > \alpha)$, effectively achieving the desired amplification mechanism.

To ensure the structural integrity of the proposed silicon-based chevron design, finite element analysis simulations are carried out using COMSOL Multiphysics® over the range of expected operating temperatures. A solid mechanics model and heat transfer model are coupled to solve for von Mises stresses, temperature distribution, and mechanical displacements. The Solid mechanics interface is based on solving the equations of motion together with a constitutive model for a solid material. In our case of considering the geometric nonlinearity, the second Piola-Kirchhoff stress tensor and the Green-Lagrange strain tensor are used. The equation of motion can be written in the following form:

$$0 = \boldsymbol{F_V} + \nabla.FS \tag{4-1}$$

where $\boldsymbol{F_V}$ is a body force with components in the current configuration "the body force is given with respect to the undeformed volume; the gradient operator is taken with respect to the material coordinates", F is the deformation gradient, and S is the second Piola-Kirchhoff stress tensor. Hook's law relates the stress tensor to the elastic strain tensor using this constitutive equation:

$$S = S_{ex} + C:\varepsilon_{el} = S_{ex} + C:(\varepsilon - \varepsilon_{inel}) \tag{4-2}$$

where S_{ex} is the extra stress contribution from initial stresses and viscoelastic stresses, C is the 4th order elasticity tensor, ": " stands for the double dot tensor product, and ε_{el} is the elastic strain: the difference between the total strain ε and the inelastic strains ε_{inel}. The strains are related to the gradients of the displacements as the following:

$$\varepsilon = \frac{1}{2}[(\nabla\mathbf{u})^T + \nabla\mathbf{u} + (\nabla\mathbf{u})^T\nabla\mathbf{u}] \tag{4-3}$$

The detailed temperature distribution through the numerical domain is solved by using this governing equation:

$$-\nabla.k(T)\nabla T = Q \tag{4-4}$$

where k is the material thermal conductivity and Q is a heat source or sink. Constant temperature boundary conditions are considered for the fixed supports (base temperature) and the chevron beams. To consider the thermal expansion in the microstructured chevron beams, the coupling between the heat transfer and solid mechanics models happens through the thermal strain equation:

$$\varepsilon_{th} = \alpha(T - T_{ref}) \tag{4-5}$$

where α is the coefficient of the thermal expansion, T is the actual temperature, and T_{ref}
is the strain reference temperature. Figure 4-2 shows the results of the numerical
simulations along with computational domain and boundary conditions. As shown on the
plots, reducing and amplification Non-linear thermal expansion mechanisms are
achieved. The non-linear thermal expansion ratio $\frac{\beta}{\alpha}$ for the reducing and the amplification
mechanisms are 0.39 and 2.94, respectively. Results of the mechanical von Mises stresses
for both mechanisms are plotted on insets of Figure 4-2. It was found that in both cases,
calculated stresses are safely below the mechanical failure limit of the silicon chevrons.
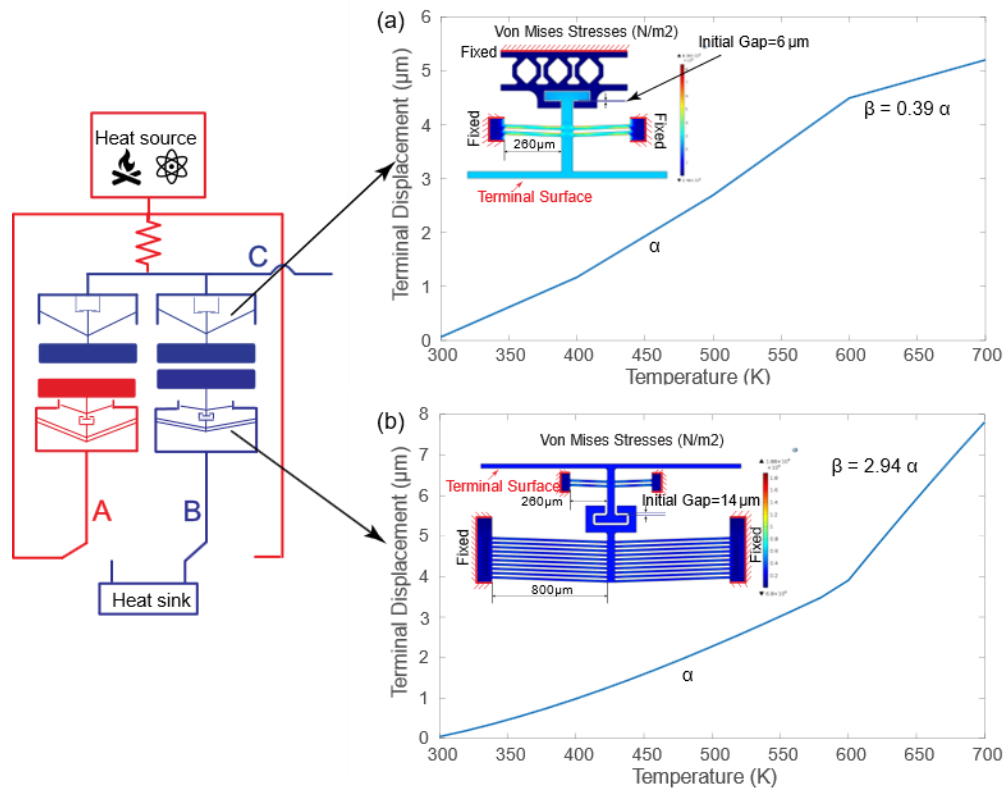
Figure 4-2: The von Mises stresses and displacement as a function of temperature for the
non-linear thermal expansion mechanisms: (a) the reducing and (b) the amplification
expansion mechanisms.

4.4. Microfabrication Process

The proposed microdevices were fabricated using cleanroom standard microfabrication techniques starting with a four-inch-diameter <100> silicon on insulator (SOI) wafer. The SOI wafer consisted of a 400-μm thick handle silicon substrate, a 1-μm thick buried silicon dioxide layer, and a 20-μm thick boron-doped silicon device layer. Figure 4-3 shows the steps of the process flow adopted for the fabrication of the non-linear thermal expansion mechanisms; in addition, the figure presents schematic of the proposed microdevices including fabricated dimensions. Following a cleaning step of the wafers, a 0.5-μm thick silicon dioxide film (acting as an electrical insulator) was thermally grown by wet oxidation in a furnace at 1100 C° (Figure 4-3b) on both sides of the wafer. On the substrate's backside, an additional 3-μm thick film of silicon dioxide was deposited via plasma-enhanced chemical vapor deposition (PECVD) to serve as an etching mask in subsequent backside etch steps. The microheaters (200-nm thick platinum and 10-nm thick tantalum as adhesion layer) were formed on top of the device layer using lift-off and E-beam evaporation as shown in Figure 4-3c. Following the formation of the microheaters, the suspended structures (Figure 4-3d), were formed through steps of reactive ion etching (to remove the 0.5-μm thick thermal silicon dioxide layer) and deep reactive ion etching of the silicon device layer. To release the final structures, backside etching was performed on the silicon dioxide, the silicon handle wafer, then the buried oxide (Figure 4-3e).
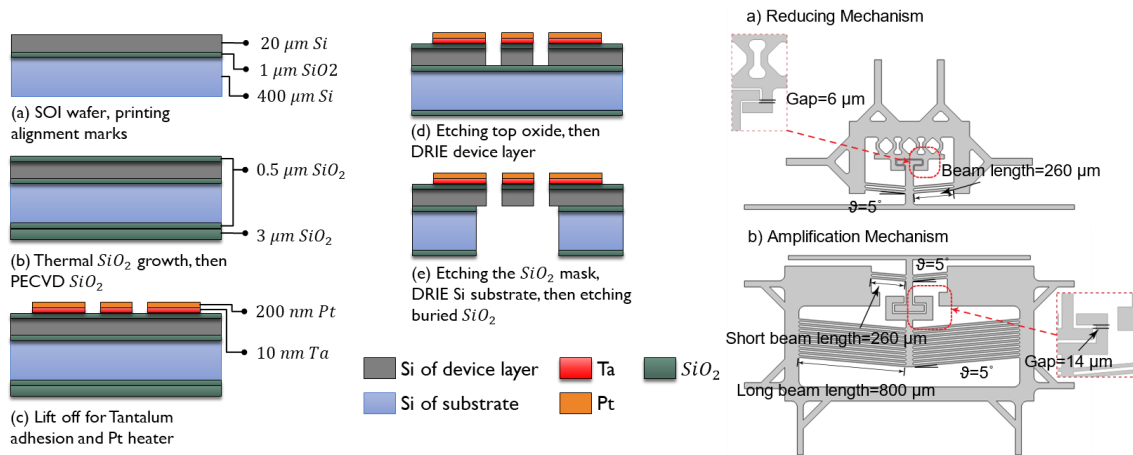
Figure 4-3: Fabrication steps and schematic of the two non-linear thermal expansion mechanisms: (a) the reducing and (b) the amplification expansion mechanisms.

Figure 4-4 shows the successful microfabrication of the proposed reducing and the amplification mechanisms.
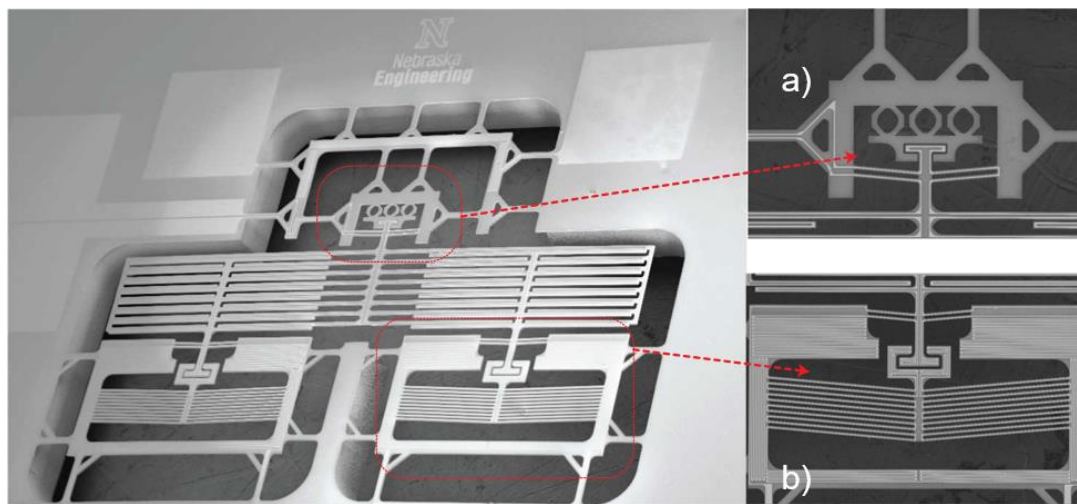
Figure 4-4: SEM images of the micro-structured thermal logic AND gate: a) the reducing and b) the amplification mechanism.

4.5. Experimental Procedure and Measurements

The non-linear thermal expansion mechanisms characterization and temperature measurements were performed inside a vacuum probe station at vacuum levels below 10^{-5} mbar; this eliminated convection and conduction heat losses. The platinum microheaters patterned on the chevron beams and terminals of the mechanisms were powered independently via two source-meter units (Keithley 2602 B and Keithley 2611 B). The microstructures' temperatures were determined from knowing the electrical resistance of the microheaters through a careful temperature coefficient of resistance (TCR) calibration. To acquire a stable TCR relationship, we annealed the microheaters many times by setting the chuck temperature to 750 K and supplying the maximum allowable current to the microheaters. The TCR calibration was carried out by varying the temperature of the chuck (which holds the microdevice inside the vacuum chamber) from room temperature to 750 K and measuring the corresponding microheaters' electrical resistances. Then, the resistance of each microheater was fitted to the corresponding temperature using a quadratic relationship [75]. The TCR measurements and relationships for both mechanisms' microheaters are shown in Figure 4-5.
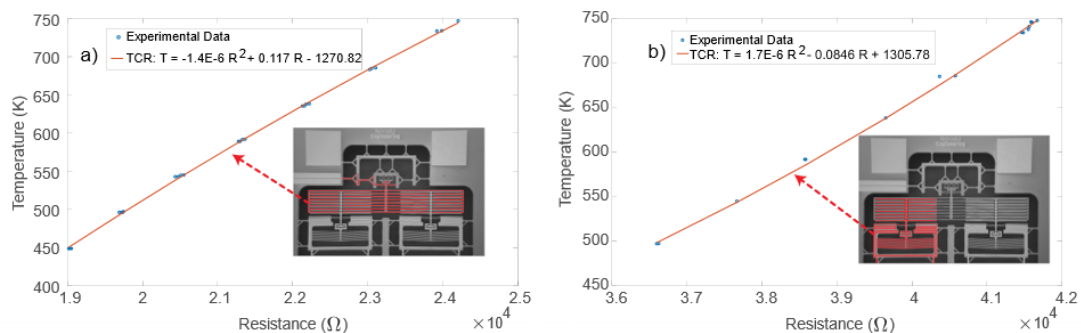

Figure 4-5: TCR calibration for the microheaters of: a) the reducing and b) the amplification mechanisms.

In the experiments, electrical current was supplied gradually through the microheaters over the mechanisms by steps of 0.1 or 0.25 mA. The voltage, resistance, and dissipated power of the microheaters were measured at each step of supplied current. According to the technique published by Moffat [76] and based on the datasheet documents of the source-meters [77] [78], the uncertainties in the voltage, current, resistance, and dissipated power were estimated at the range of 0.05-0.06 V, 0.6-0.7 μA, 18-248 Ω, and 0.001-0.5 mW, respectively. In addition, at each step, the displacement of the mechanisms was estimated by tracking their motions using the optical microscope attached to the vacuum probe station. The images captured by the microscope were analyzed using MATLAB to estimate the terminals' relative displacements. Due to the high electric resistances of the heaters, the experiments were performed at high chuck temperatures; this helped to reduce the required power to actuate the mechanisms. Figure 4-6 presents the motion evolution of the non-linear expansion mechanisms ((a) the spring-assisted reduction and (b) the cascading chevrons amplification) with increasing microstructure temperature. By increasing the supplied current, the temperature of the reducing mechanism increases, so the chevron beams are displaced downwards; the gap reduces. At a temperature of 861 K, the gap vanishes and the spring-assisted structure presence results in reducing the thermal expansion rate of the beams and that of the terminal surfaces as well. For the amplification mechanism, the initial increase of temperature results in displacing the short and long beams downwards, where the long beams are displaced by higher expansion rate; the gap reduces. Consequently, at a temperature of 873 K, the gap vanishes, and the interlocking of cascading structures results in magnifying the thermal expansion rate of the short beams and that of the terminal surfaces as well.
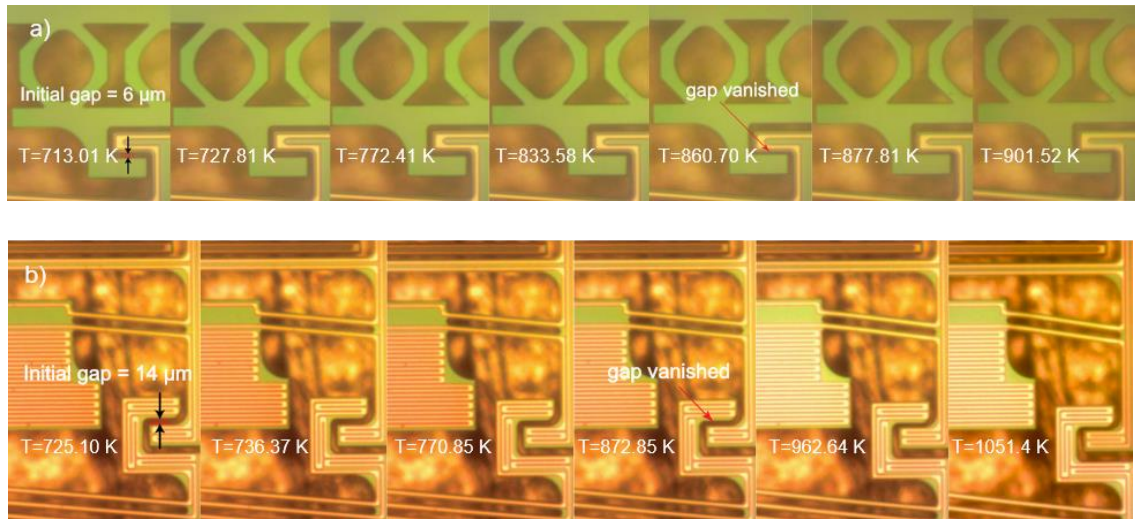
Figure 4-6: The motion evolution of the non-linear expansion mechanisms over the range of the operating temperatures: a) the spring-assisted reduction and b) the cascading chevrons amplification mechanisms.

In Figure 4-7, the relative displacements of the terminal surfaces (circled in the inset) are plotted as a function of temperature. The results show that we achieved experimentally non-linearity ratios of thermal expansion $\frac{\beta}{\alpha}$ of 0.36 and 3.06 for the reducing and the amplification mechanisms, respectively. It is worth mentioning that parameters such as the beams lengths and chevron angles and the initial gaps can be tailored to achieve a specific non-linearity ratio $\left(\frac{\beta}{\alpha}\right)$ or temperature threshold (i.e., temperature at which displacement slope begins to change).
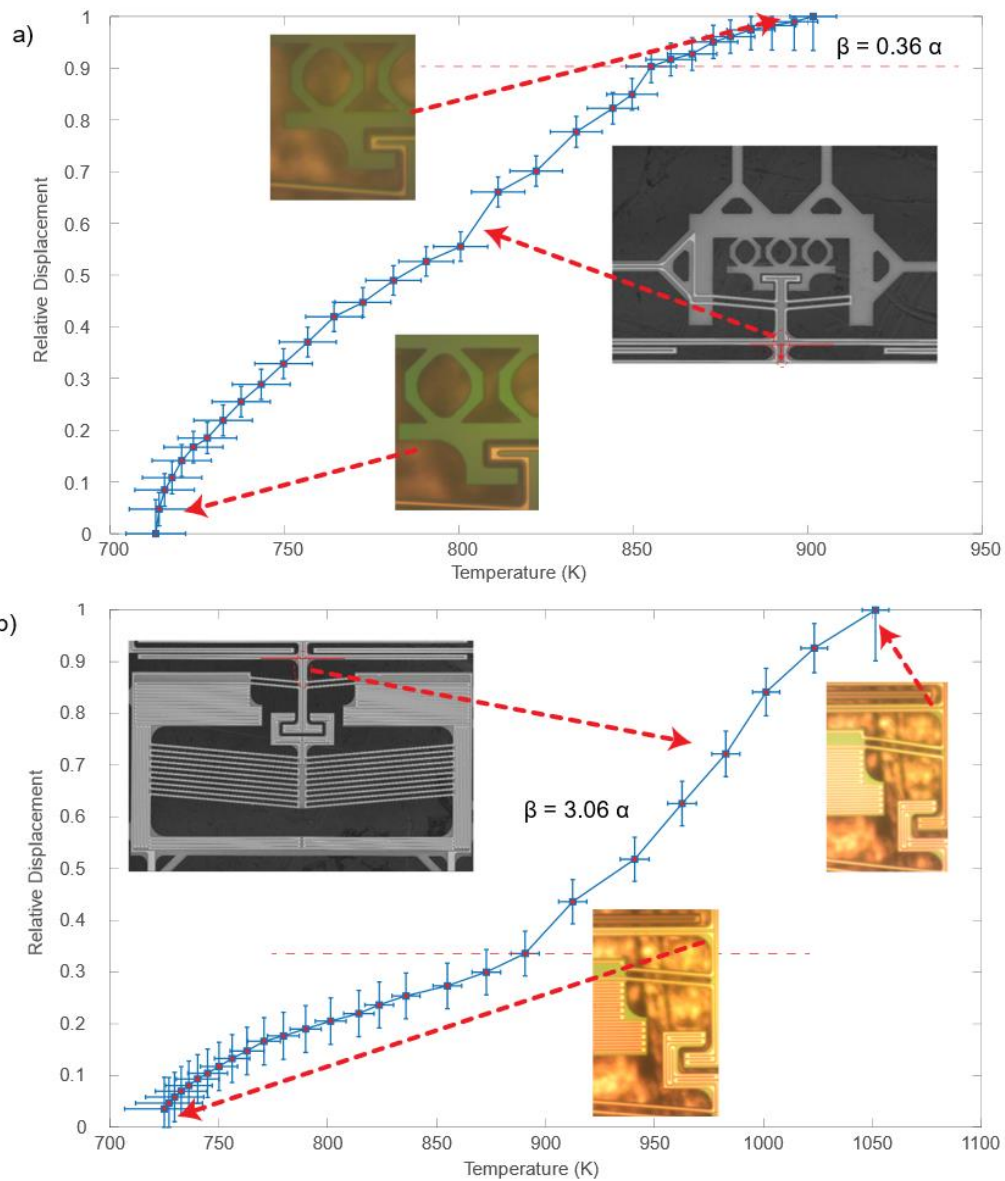
Figure 4-7: The relative displacement of both the non-linear expansion mechanisms over the range of the operating temperature: a) the reducing and b) the amplification mechanisms.

4.6. Conclusions

In this chapter, we presented the design, modeling, fabrication, and characterization of two novel non-linear thermal expansion designs of microstructure

silicon V-shaped chevron beams. The desired non-linearities of the mechanisms were achieved using easy-to-fabricate chevron mechanisms consisting of spring-assisted reduction and cascading chevrons amplification. The success in achieving the desired non-linearities of the expansion mechanisms enables the fabrication of the thermal AND gate with high effectiveness; hence, paving the path for the eventual realization of thermal computing.

4.7. Acknowledgments

Chapter 5: NanoThermoMechanical AND and OR Logic Gates

The contents of this chapter will be submitted for publication in Nature Scientific Reports.

5.1. Abstract

Today's electronics cannot perform in harsh environments (e.g., elevated temperatures and ionizing radiation environments) found in many engineering applications. Based on the coupling between near-field thermal radiation and MEMS thermal actuation, we presented the design and modeling of NanoThermoMechanical AND, OR, and NOT logic gates, and we showed their ability to be combined into a full thermal adder to perform complex operations. In this work, we introduce the fabrication and characterization of the first ever documented Thermal AND and OR logic gates. The results show thermal logic operations can be achieved successfully through demonstrated and easy-to-manufacture NanoThermoMechanical logic gates.

5.2. Introduction

Today's electronics have limited performance and reliability in harsh environments (e.g., elevated temperatures and ionizing radiation environments) found in many engineering applications such as space exploration (e.g., Venus) and geothermal energy exploitation deep beneath the earth; consequently, developing alternative computing technologies is necessary. Thermal computing, data processing based on heat instead of electricity, is proposed as a practical solution and opens a new scientific area at the interface between thermal and computational sciences. The traditional linear and passive thermal components, such as thermal resistors and capacitors, are not sufficient to

introduce an integrated thermal logic circuit. It is needed to realize switchable and nonlinear thermal components as their electronic counterparts, which leads to tunable thermal control devices and paves the way for thermal computation technology and thermal information treatment.

Many designs have been proposed to realize thermal diodes, switches, transistors, and thermal logic gates [1] [2] [3]. Researchers have successfully demonstrated thermal switches and regulators by taking advantage of the non-linear behavior of the temperature / phase-dependent thermal conductivity of certain materials [4] [5] [6] [7] [8] [9], tailoring heat conduction through solid/solid and solid/liquid physical contact [10] [11], and manipulating convection heat transfer mechanisms [12] [13] [14] [15]. Thermal radiation [16] [17] [18] [19] [20] [37]on the other hand seems to be the most promising approach; however, most of the currently proposed thermal devices are limited to a small operating temperature range or specific materials. Clearly, there are enough challenges already in developing individual thermal rectifiers or diodes, seemingly making illusive the realization of an operating thermal logic circuit. Previously, we built and simulated a thermal calculator based on clustered NanoThermoMechanical logic gates that could perform similar operations as their electronic counterparts. We presented the design and modeling of NanoThermoMechanical AND, OR, and NOT logic gates, achieved through the coupling between near-field thermal radiation (NFTR) and MEMS thermal actuation [42]. NFTR transfers heat via thermal radiation between two surfaces separated by a very small vacuum gap (i.e., comparable to the radiation wavelength). NFTR's intensity increases exponentially with a decreasing separation gap. Based on this design, we

present here the fabrication and characterization of the NanoThermoMechanical AND

and OR logic gates.

5.3. Design and Methodology

Based on the concept of coupling NFTR and thermal actuation of a chevron beam

actuator, thermal AND and OR gates are constructed using a combination of two thermal

diodes and a fixed-value conduction thermal resistance (i.e., solid beams with tailored

thermal conductance) as shown in Figure 5-1 [42]. For the AND gate, the upper terminals

(output) are connected together to a fixed conductive resistance, which is connected to

the heat source. Consequently, the temperature of the output terminal C is a result of the

heat balance between the inward conduction heat flow from the heat source (Q_{cond}) and

the outward radiation heat flows ($Q_{rad,NF}$ or $Q_{rad,FF}$) to the lower input terminals (A and

B). To achieve the required functionality of the AND gate, output upper terminal C needs

to be at its bottom position when $T_A = T_{min}$ or $T_B = T_{min}$, regardless the temperature of

terminal C, to achieve the minimum separation distance between terminals (i.e., near-

field thermal radiation). In addition, terminals A and B need to be separated by large

enough gap from terminal C (i.e., far-field thermal radiation) when $T_A = T_{max}$ or $T_B =$

T_{max}, regardless the temperature of terminal C. In other words, nonlinearity in the

terminals' thermal displacement is required. The upper terminal (output) of the thermal

AND gate must feature a reduced $\left(\frac{\beta}{\alpha} < 1\right)$ thermal expansion while the lower terminals

(inputs) must experience amplification $\left(\frac{\beta}{\alpha} > 1\right)$, where α is the displacement rate of the

terminal between T_{room} and T_{min}, and β is the displacement rate of the terminal between

T_{min} and T_{max}.

The reducing mechanism can be achieved by spring-assisted chevron beams. The terminal surface is connected to the chevron beams and separated by a small gap from a spring-loaded stopper. Through initial heating, the terminal surface is displaced downwards with a certain expansion rate α due to the thermal expansion of the chevron beams. Further heating to a certain designed temperature, the chevron comes in contact with the spring-loaded structure which reduces the expansion rate of the terminal surface to β ($\beta < \alpha$) proportional to the spring constant and effectively achieving the desired reducing mechanism. As for the amplification mechanism, it can be achieved via two interlocked cascading chevrons with different arm lengths and separated by a small gap. The terminal surface is connected to the short arms chevron. Through heating, the terminal surface is displaced downwards with a certain expansion rate α, smaller than the expansion rate of the long arms chevron. Further heating to a certain designed temperature causes the two chevrons to interlock and for the terminal surface to expand at a higher rate β, ($\beta > \alpha$), effectively achieving the desired amplification mechanism.

For the OR gate, the lower terminals (output) are connected together to the heat sink through a fixed conductive resistance. Consequently, the temperature of the output terminal C is a result of the heat balance between the inward heat flows ($Q_{rad,NF}$ or $Q_{rad,FF}$) from the lower input terminals (A and B) and the outward heat flow to the heat sink (Q_{cond}). The temperature of each of the input terminals can be controlled independently by choosing to connect the terminals to either the heat source (T_{max}) or the heat sink (T_{min}).
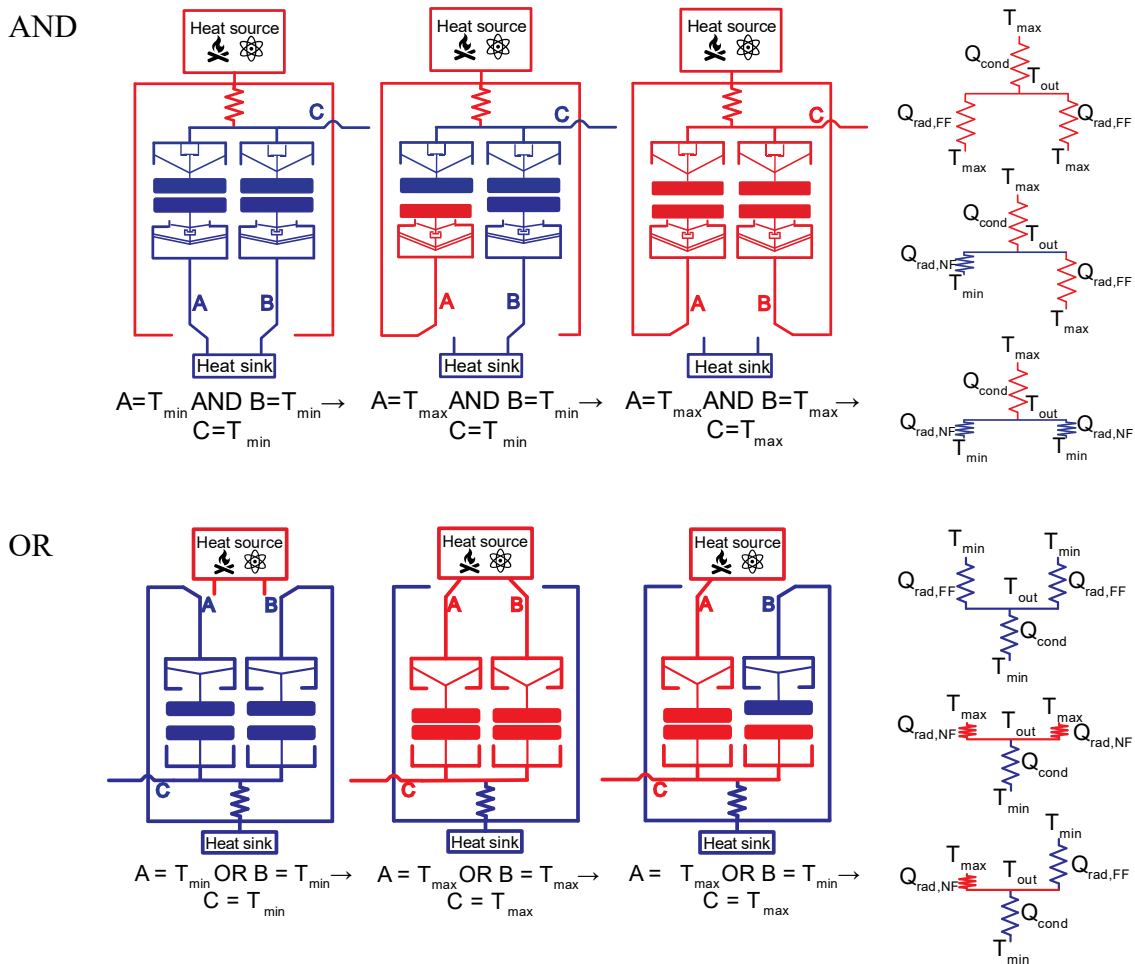
Figure 5-1: Schematic drawings of the thermal AND and OR logic gates with the heat transfer circuits.

5.4. Microfabrication Process

The proposed microdevices were fabricated using cleanroom standard microfabrication techniques starting with a four-inch-diameter <100> silicon on insulator (SOI) wafer. The SOI wafer consisted of a 400-µm thick handle silicon substrate, a 1-µm thick buried silicon dioxide layer, and a 20-µm thick boron-doped silicon device layer. Figure 5-3 presents schematic of the proposed microdevices including fabricated dimensions. Figure 5-3 shows the steps of the process flow adopted for the fabrication of

the NanoThermoMechanical logic gates. Following a cleaning step of the wafers, a 0.5-µm thick silicon dioxide film (acting as an electrical insulator) was thermally grown by wet oxidation in a furnace at 1100 C° (Figure 5-3b) on both sides of the wafer. On the substrate's backside, an additional 3-µm thick film of silicon dioxide was deposited via plasma-enhanced chemical vapor deposition (PECVD) to serve as an etching mask in subsequent backside etch steps. The microheaters (200-nm thick platinum and 10-nm thick tantalum as adhesion layer) were formed on top of the device layer using lift-off and E-beam evaporation as shown in Figure 5-3c. Following the formation of the microheaters, the suspended structures (Figure 5-3d), were formed through steps of reactive ion etching (to remove the 0.5-µm thick thermal silicon dioxide layer) and deep reactive ion etching of the silicon device layer. To release the final structures, backside etching was performed on the silicon dioxide, the silicon handle wafer, then the buried oxide (Figure 5-3e).
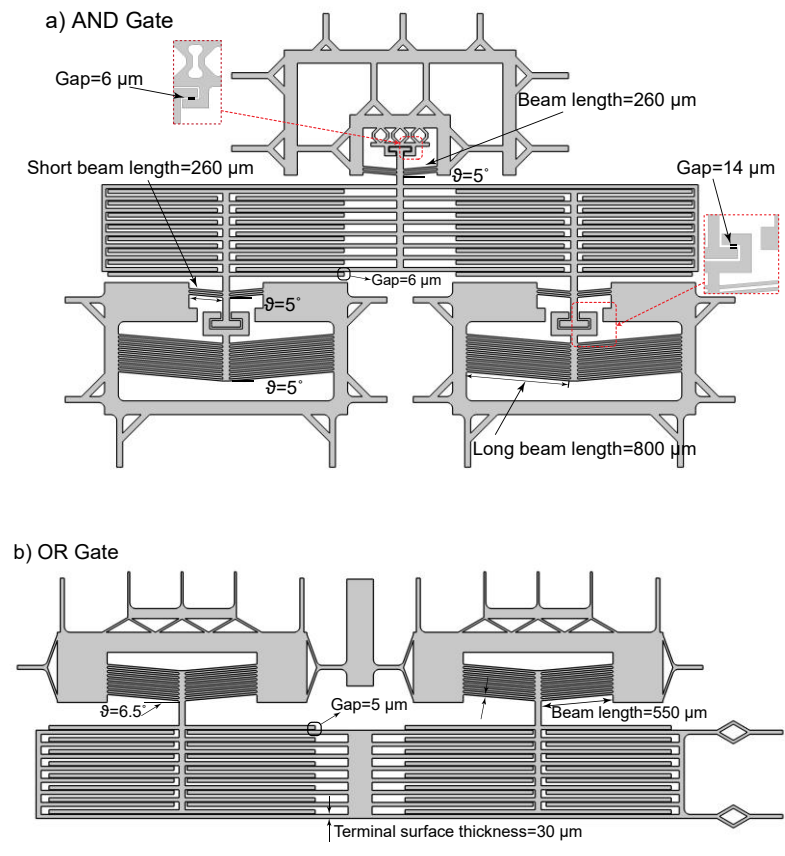
Figure 5-2: Schematic of the proposed NanoThermoMechanical a) AND and b) OR logic gates.
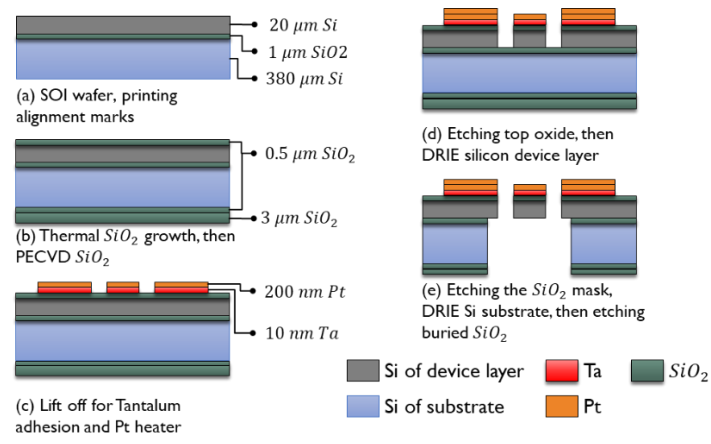
Figure 5-3: Microfabrication steps of the NanoThermoMechanical AND and OR logic gates.

We designed three photolithography masks: platinum microheaters, silicon front side microstructures, and silicon backside etching. These masks were employed through the microfabrication process flow adopted to fabricate the designed thermal gates. *Figure 5-4* and *Figure 5-5* show the successful microfabrication of the thermal AND and OR gates, respectively, including the reducing and the amplification mechanisms for the thermal AND gate.
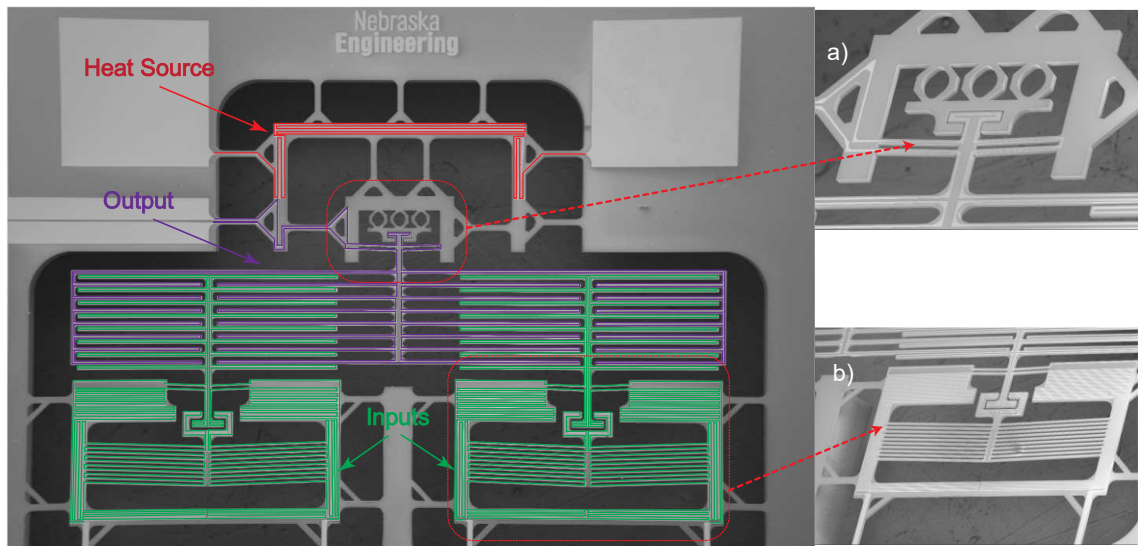
Figure 5-4: SEM images of the micro-structured thermal logic AND gate including: a) the reducing and b) the amplification mechanism.
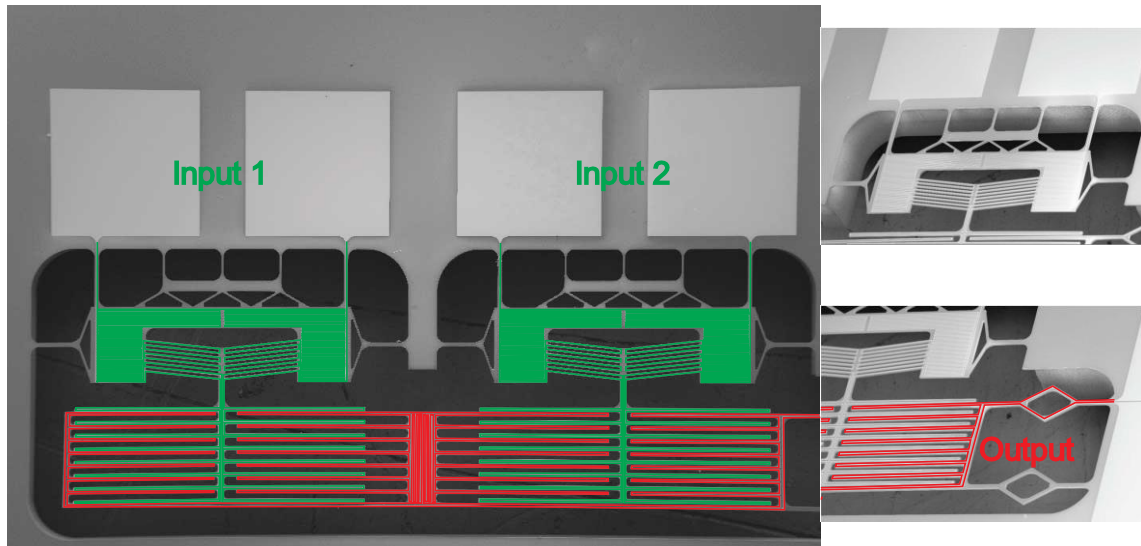
Figure 5-5: SEM images of the micro-structured thermal logic OR gate including two inputs (chevron beams) and output (fixed terminals).

5.5. Experimental Procedure and measurements

The characterization and heat transfer measurements of the thermal logic gates were performed inside a vacuum probe station at vacuum levels below 10^{-5} mbar, in order to eliminate convection and conduction heat losses. The platinum microheaters patterned on the mechanisms were powered independently via two source-meter units (Keithley 2602 B and Keithley 2611 B). The microstructures' temperatures were determined from knowing the electrical resistance of the microheaters through a careful temperature coefficient of resistance (TCR) calibration. To acquire a stable TCR relationship, we annealed the microheaters many times by setting the chuck temperature to 750 K and supplying the maximum allowable current to the microheaters. The TCR calibration was carried out by varying the temperature of the chuck (which holds the microdevice inside the vacuum chamber) from room temperature to 750 K and measuring the corresponding microheaters' electrical resistances. Then, the resistance of each

microheater was fitted to the corresponding temperature using a quadratic relationship

[75]. *Figure 5-6* and *Figure 5-7* show the TCR measurements and relationships for the

microheaters of the AND and OR thermal gates, respectively.
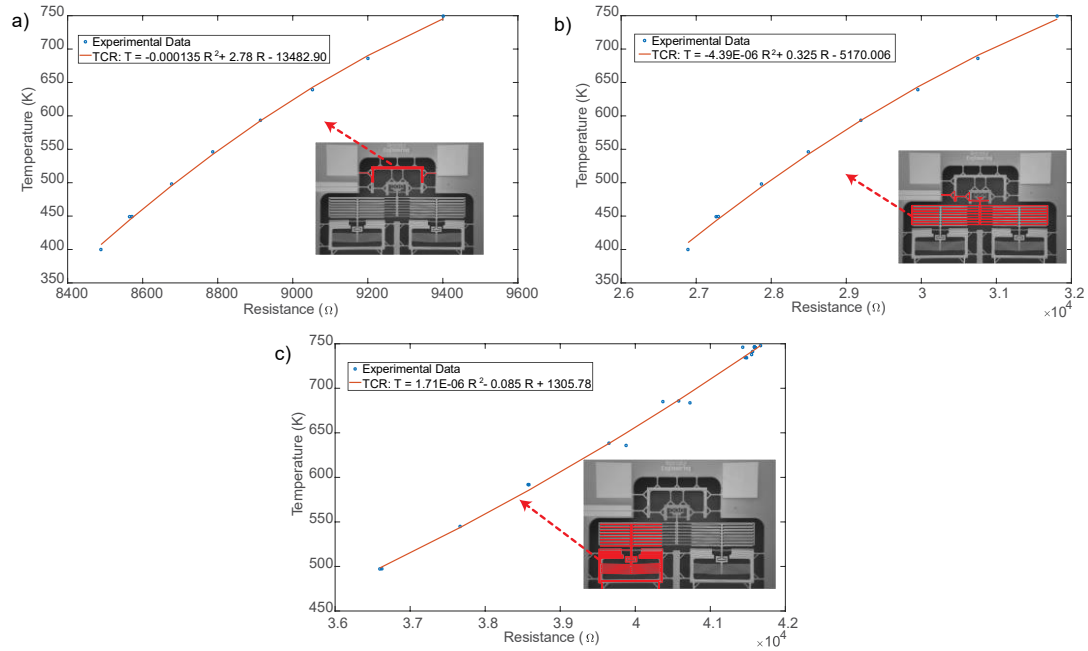
Figure 5-6: TCR calibration for the microheaters of the AND thermal gate for: a) the heat

source, b) the output and c) the input.
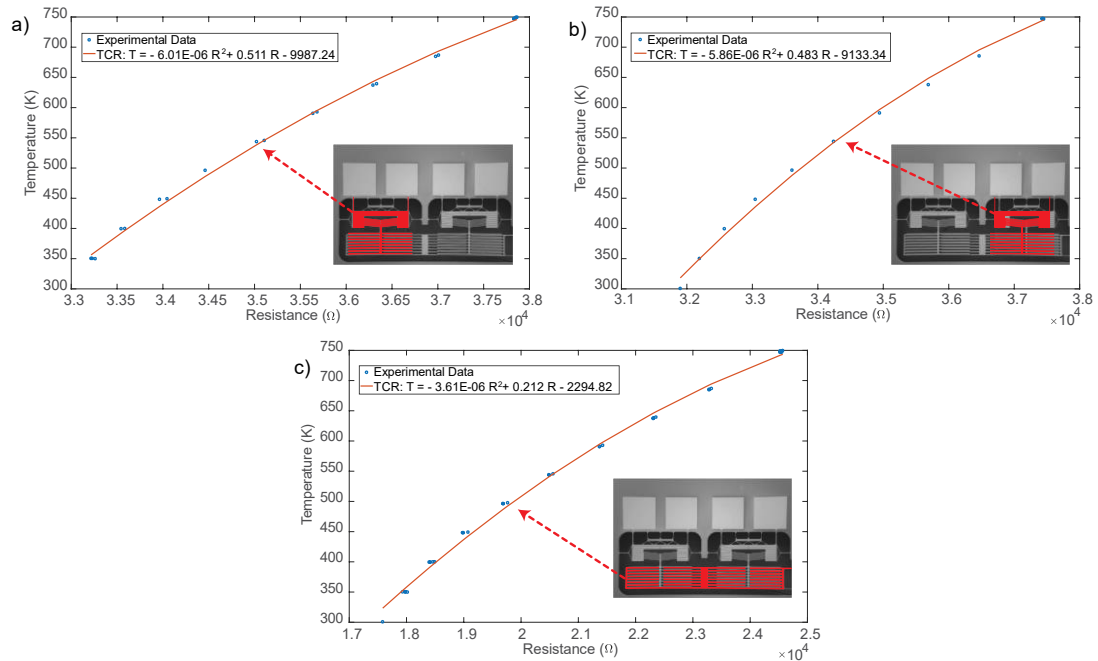
Figure 5-7: TCR calibration for the microheaters of the OR thermal gate for: a) the input 1, b) the input 2 and c) the output.

Throughout the experiments, the electrical current was supplied gradually through the microheaters over the mechanisms by a step of 0.1 or 0.25 mA. The voltage, resistance, and dissipated power of the microheaters were measured at each step of the supplied current. According to the technique published by Moffat [76] and based on the datasheet documents of the source-meters [77] [78], the uncertainties in the voltage, current, resistance, and dissipated power were estimated in the ranges of 0.05-0.06 V, 0.6-0.7 μA, 165-350 Ω, and 0.1-0.6 mW, respectively. Due to the high resistances of the heaters, the experiments were performed at high chuck temperatures, which helped in reducing the required power to actuate the mechanisms. Moreover, our vacuum probe station includes four probes, so just two heaters could be characterized simultaneously. Consequently, for the thermal AND logic gate, we could just present thermal results for

the case when the two inputs were at T_{min} (i.e., 0,0 case), since two probes were used for supplying the heat source heater and the other two probes were used for measuring the output heater. As shown in *Figure 5-8*, the effectiveness is represented as a function of the heat source temperature. We define the effectiveness, ϵ, of the thermal logic gates as

$\epsilon = \frac{T_{out} - T_{min}}{T_{max} - T_{min}}$, where T_{out} is the output terminals temperature, T_{min} is the minimum operating temperature (i.e., the chuck temperature) and T_{max} is the maximum operating temperature (i.e., the heat source temperature). It can be illustrated that the higher the heat source temperature, the lower the effectiveness that can be achieved. The effectiveness decreased from 17.9 % to 10.7 % by increasing the heat source temperature from 930 K to 1549 K. This is because at a higher heat source temperature, the output terminals get closer to the input terminals and near field radiation effects become important.
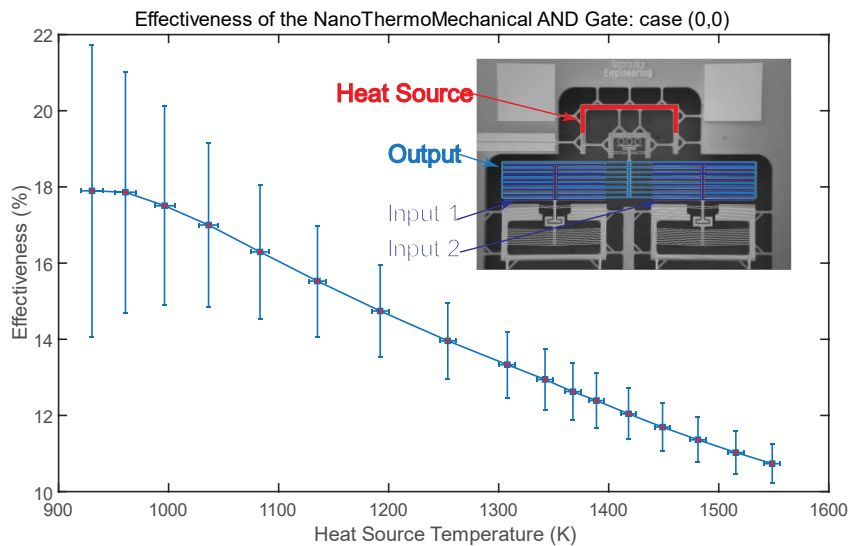
Figure 5-8: The effectiveness of the NanoThermoMechanical AND gate over the range of the heat source temperature for the case (0,0).

For the thermal OR logic gate, two probes were used for heating one of the two inputs, and the other two probes were used for measuring the temperature of the output heater. Consequently, temperature results for the cases of (1,0) and (0,1) could be presented for the thermal OR logic gate. The effectiveness of the gate for these two cases is shown in *Figure 5-9*a and *Figure 5-9*b as a function of the input temperature. It can be illustrated that the higher the input temperature, the higher the effectiveness that can be achieved. For the (1,0) case, the effectiveness increased from 13.5 % to 25.3 % with increasing input temperature from 943 K to 1324 K. For the (0,1) case, the effectiveness increased from 12.0 % to 23.2 % with increasing input temperature from 931 K to 1391 K. This is because at a higher input temperature, the input terminals get closer to the output terminals, making near-field radiation the dominant heat transfer mechanism.

The ratio between Q_{out} (the net power transferred to the output terminals) and Q_{in} (the supplied power to the input terminals) is shown in *Figure 5-10*a and *Figure 5-10*b. It is illustrated that by increasing the input temperature, the ratio of the powers increases because of the near-field radiative heat transfer. This ratio can be enhanced by reducing the conduction losses through the microdevice supports and the radiation losses to the chamber. It is worth mentioning that by conducting the experiment of the (1,1) case, where the two inputs are powered to high temperature, the effectiveness is expected to reach higher values.
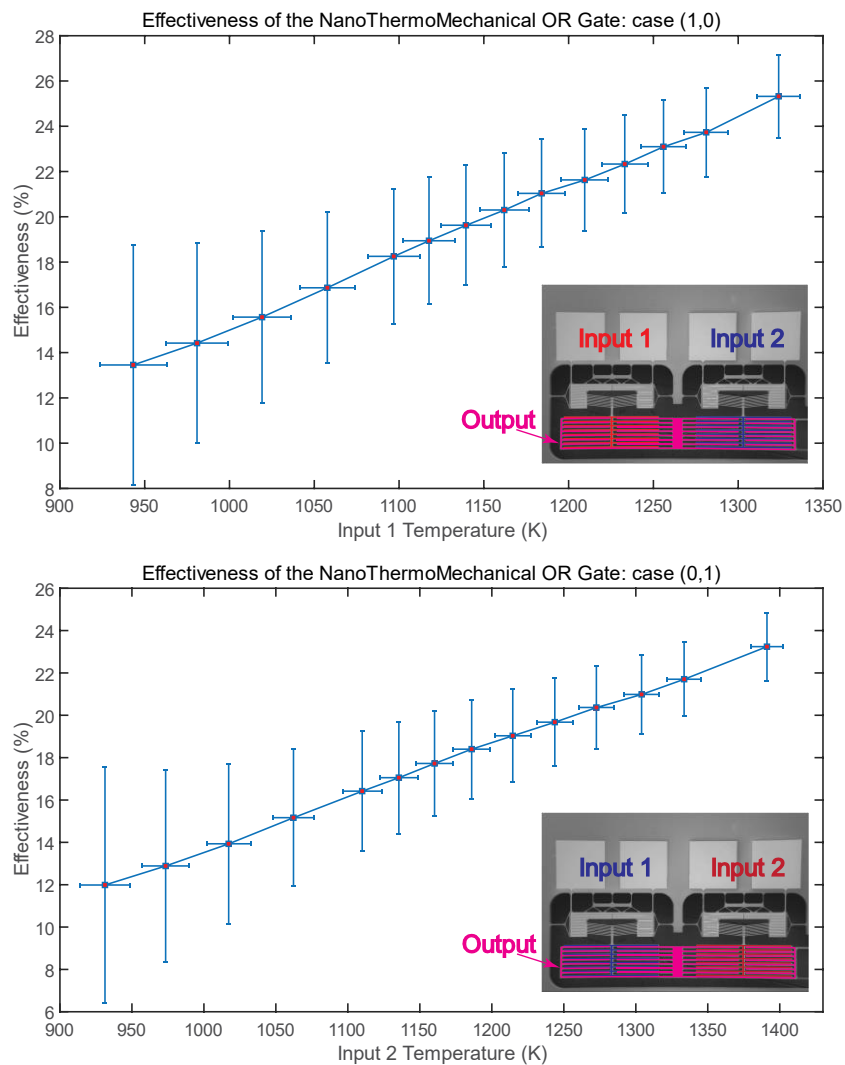
Figure 5-9: The effectiveness of the NanoThermoMechanical OR gate over the range of input temperatures for: a) case (1,0) and b) case (0,1).
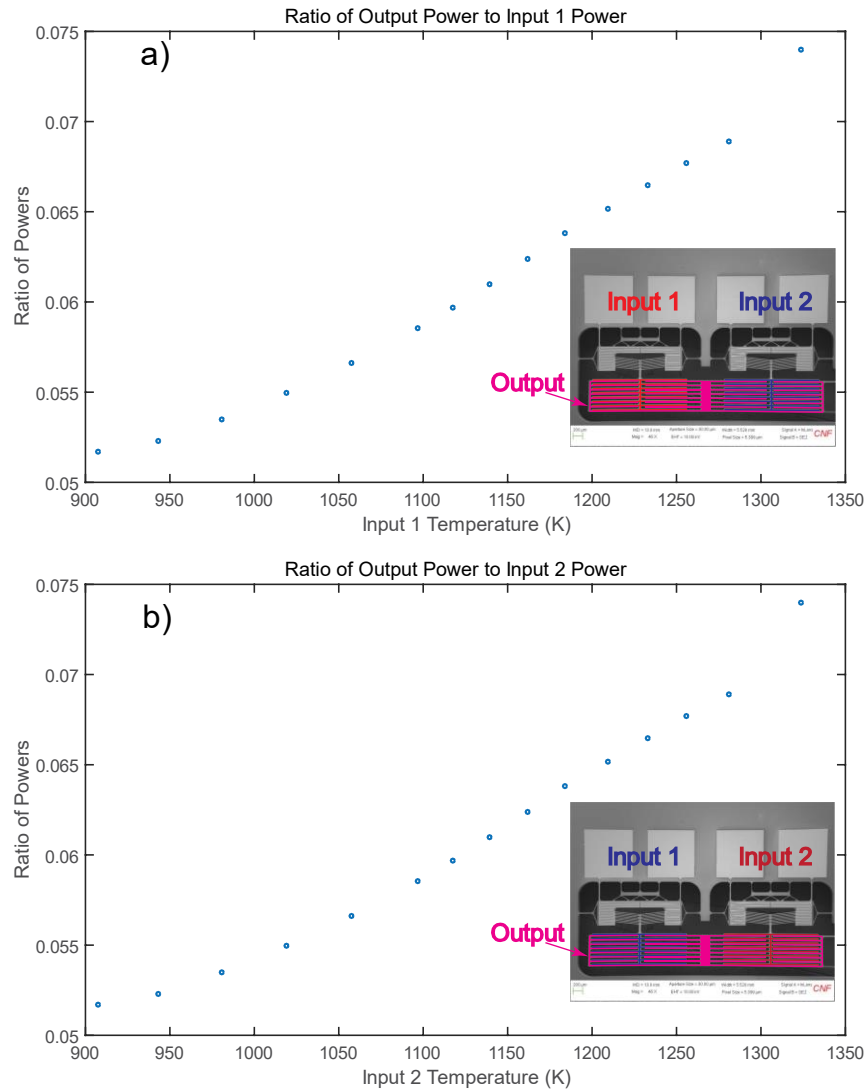
Figure 5-10: The ratio of the output net power to the input power of the

NanoThermoMechanical OR gate over the range of input temperatures for: a) case (1,0)

and b) case (0,1).

5.6. Conclusions

In this paper, we presented the design, microfabrication and characterization of

first ever documented thermal AND and OR logic gates. The desired non-linearities of

associated NanoThermoMecahnical mechanisms were achieved using novel, ingenious,

and easy to fabricate chevron mechanisms consisting of spring-assisted reduction and cascading chevron amplification. The success of the current experiments in achieving relatively high logic gate effectiveness has paved the path to the future dawn of thermal computing.

5.7. Acknowledgments

Chapter 6: Conclusions and Recommendations

This dissertation has introduced near-field thermal radiation coupled with MEMS thermal actuation to build NanoThermoMechanical logic gates operated at high temperatures. These NanoThermoMechanical logic gates are the building blocks of the thermal computation technology, which is a promising alternative to electronics that typically fail in harsh environments such as high temperatures and ionizing radiation.

First, we introduced the idea of creating a thermal diode to control the resistance of heat flow in response to heat flow direction. Using the thermal diode, we developed the design and modeling of NanoThermoMechanical AND, OR and NOT logic gates. In the process, NanoThermoMechanical AND logic gate requires nonlinearity in the terminals' thermal displacement. We developed two novel non-linear thermal expansion designs using novel and ingenious microstructured chevron mechanisms consisting of spring-assisted reduction and cascading chevrons amplification for the output and the input terminals, respectively.

The simulation results of the NanoThermoMechanical AND logic gate show that we were able to successfully develop a thermal logic AND gate with effectiveness between 0.01 and 0.1 (with the highest studied conductance), for $T_{0,0}, T_{1,0}$ and $T_{0,1}$ cases. For the NanoThermoMechanical OR logic gate, we successfully developed a thermal logic OR gate with effectiveness between 0.97 (for highest studied conductance) and 0.995, for the cases when any input is at T_{max}. For the NanoThermoMechanical NOT logic gate, the effectiveness is between 0 and 0.03, when the input is at T_{max}, and between 0.97 and 1, when the input is at T_{min}. For all thermal logic gates, as the

conductance increases, the thermal logic gates deviate slightly away from their ideal truth table. Based on the successful design of the basic thermal logic gates, we showed their ability to be combined into a full thermal calculator to perform the addition of two decimal numbers based on binary mathematical computations.

The concept of NanoThermoMechanical AND and OR logic gates have been shown experimentally by fabricating proof-of-concept microdevices via cleanroom standard microfabrication techniques starting with a four-inch-diameter <100> silicon on insulator (SOI) wafer. First, we investigated experimentally the non-linearity of the two novel non-linear thermal expansion mechanisms employed in the NanoThermoMechanical AND gate. The desired non-linearities of the mechanisms were achieved using easy-to-fabricate V-shaped chevron mechanisms consisting of spring-assisted reduction and cascading chevrons amplification for the reducing and the amplification mechanisms, respectively. The results show that we achieved experimentally non-linearity ratios of thermal expansion $\frac{\beta}{\alpha}$ of 0.36 and 3.06 for the reducing and the amplification mechanisms, respectively. It is worth mentioning that parameters such as the beams lengths and chevron angles and the initial gaps can be tailored to achieve a specific non-linearity ratio $\left(\frac{\beta}{\alpha}\right)$ or temperature threshold (i.e., temperature at which displacement slope begins to change).

Furthermore, we investigated experimentally the thermal computation of the NanoThermoMechanical AND and OR logic gates. We investigated the case (0,0) of the thermal AND logic gate, and we achieved an effectiveness of 10.7 % at a heat source temperature of 1549 K. For the thermal OR logic gate, for the cases of (1,0) and (0,1), we

achieved an effectiveness of 25.3 % and 23.2 % at an input temperature of 1324 K and 1391 K, respectively. These results are significant breakthroughs in the field of thermal computation science and technology as they demonstrate thermal computing at high temperatures based on demonstrated and easy to manufacture NanoThermoMechanical logic gates.

Through the quest to realize this dissertation, I can list the following areas that need the scientific and engineering community attentions:

- We need to develop smaller NanoThermoMechanical Logic gates in order to enhance the dynamic interaction between near-field thermal radiation and expansion in microstructure. This can be achieved through advancements in microfabrication technologies that enable the minimum feature (i.e., separation distance between terminals) to be less than 0.5 μm. This helps to tailor the beams to have shorter sizes (i.e., smaller microdevices).

- We need to develop structures/materials that can achieve the enhancement of near-field thermal radiation at micrometric distance, rather than nanometric. This can be achieved through employing meshed photonic crystals, but the challenge that it enhances both the near-field and the far-field thermal radiation [79]. Meanwhile, we need more contrast between the near-field and the far-field thermal radiation (i.e., forward and backward directions) to achieve more robust logic system.

- We need to develop mechanisms and structures to support terminals exchanging near-field thermal radiation that are robust, compact and feature low thermal conductance. Based on the results in chapter 3, lower thermal conductance results

in enhancement of the NanoThermoMechanical logic gates performance (i.e., effectiveness).

- Regarding the design of the microheaters, the electrical resistance should be high enough to improve the accuracy of the measurements. Meanwhile, the resistance should be low enough to reduce the required voltage to actuate the mechanism, also the actuation can be activated at lower chuck temperatures. Additionally, during the annealing process, the resistances reach higher values (about two or three times) compared to their values after the microfabrication, and this must be considered during the design of the heater.

- Another idea is to design the microheaters of the two inputs to be electrically in series, so two probes can be used to operate the two microheaters simultaneously.

- Regarding the experimental procedure and measurements, to reduce the radiation losses, the vacuum station is recommended to be heated up to the same temperature as the chuck temperature. This indicates that the surrounding temperature is the same as the heat sink, which mimics the harsh environments that the thermal computation technology targets.

- We need to investigate thermal communication technology (data traffic). The challenge is how to generate pulses (ON-OFF) using heat instead of electrical or laser sources.

References

[1] G. Wehmeyer, T. Yabuki, C. Monachon, J. Wu and C. Dames, "Thermal Diodes, Regulators, and Switches: Physical Mechanisms and Potential," *Applied Physics Reviews,* vol. 4, no. 041304, 2017.

[2] P. Ben-Abdallah and S.-A. Biehs, "Contactless Heat Flux Control with Photonic Devices," *AIP Advances,* vol. 5, no. 053502, 2015.

[3] N. Li, J. Ren, L. Wang, G. Zhang, P. Hanggi and B. Li, "Colloquium: Phononics: Manipulating Heat Flow with Electronic Analogs and Beyond," *Reviews of Modern Physics,* vol. 84, 2012.

[4] S. Lee, K. Hippalgaonkar, F. Yang, J. Hong, C. Ko, J. Suh, K. Liu, K. Wang, J. J. Urban, X. Zhang, C. Dames, S. A. Hartnoll, O. Delaire and J. Wu, "Anomalously Low Electronic Thermal Conductivity in Metallic Vanadium Dioxide," *Science,* no. 355, pp. 371-374, 2017.

[5] J. P. Reifenberg, M. A. Panzer, S. Kim, A. M. Gibby, Y. Zhang, S. Wong, W. H.-S. Philip, E. Pop and K. E. Goodson, "Thickness and Stoichiometry Dependence of the Thermal Conductivity of GeSbTe Films," *Applied Physics Letters,* vol. 91, no. 111904, 2007.

[6]   J. Lee, E. Bozorg-Grayeli, S. Kim, M. Asheghi, H.-S. P. Wong and K. E. Goodson, "Phonon and electron transport through Ge2Sb2Te5 films and interfaces bounded by metals," *Applied Physics Letters,* vol. 102, no. 191911, 2013.

[7]   R. Zheng, J. Gao, J. Wang and G. Chen, "Reversible temperature regulation of electrical and thermal conductivity using liquid–solid phase transitions," *Nature Communications,* vol. 2, no. 289, 2011.

[8]   J. Crossno, J. K. Shi, K. Wang, X. Liu, A. Harzheim, A. Lucas, S. Sachdev, P. Kim, T. Taniguchi, K. Watanabe, T. A. Ohki and K. C. Fong, "Observation of the Dirac Fluid and the Breakdown of the Wiedemann-Franz Law in Graphene," *Science,* vol. 351, no. 6277, pp. 1058-1061, 2016.

[9]   J. F. Ihlefeld, B. M. Foley, D. A. Scrymgeour, J. R. Michael, B. B. McKenzie, D. L. Medlin, M. Wallace, S. Trolier-McKinstry and P. E. Hopkins, "Room-Temperature Voltage Tunable Phonon Thermal Conductivity via Reconfigurable Interfaces in Ferroelectric Thin Films," *Nano Letters,* vol. 15, no. 3, p. 1791–1795, 2015.

[10] J. Cho, C. Richards, D. Bahr, J. Jiao and R. Richards, "Evaluation of Contacts for a MEMS Thermal Switch," *Journal of Micromechanics and Microengineering,* vol. 18, no. 105012, 2008.

[11] C. Tso and C. Y. Chao, "Solid-State Thermal Diode with Shape Memory Alloys," *International Journal of Heat and Mass Transfer,* vol. 93, pp. 605-611, 2016.

[12] J. B. Boreyko, Y. Zhao and C.-H. Chen, "Planar Jumping-Drop Thermal Diodes," *Applied Physics Letters,* vol. 99, no. 234105, 2011.

[13] G. Cha, C.-J. Kim and Y. S. Ju, "Thermal Conductance Switching Based on the Actuation of Liquid Droplets through the Electrowetting on Dielectric (EWOD) Phenomenon," *Applied Thermal Engineering,* vol. 98, pp. 189-195, 2016.

[14] A. R. McLanahan, C. D. Richards and R. F. Richards, "A Dielectric Liquid Contact Thermal Switch with Electrowetting Actuation," *Journal of Micromechanics and Microengineering,* vol. 21, no. 104009, 2011.

[15] H. J. Cho, J. P. Mizerak and E. N. Wang, "Turning Bubbles on and off During Boiling Using Charged Surfactants," *Nature Communications,* vol. 6, no. 8599, 2015.

[16] K. Ito, K. Nishikawa, H. Iizuka and H. Toshiyoshi, "Experimental Investigation of Radiative Thermal Rectifier Using Vanadium Dioxide," *Applied Physics Letters,* vol. 105, no. 253503, 2014.

[17] P. Ben-Abdallah and S.-A. Biehs, "Phase-Change Radiative Thermal Diode," *Applied Physics Letters,* vol. 103, no. 191907, 2013.

[18] P. Ben-Abdallah and S. A. Biehs, "Towards Boolean Operations with Thermal Photons," *Physical Review B,* vol. 94, no. 241401, 2016.

[19] M. Elzouka and S. Ndao, "High Temperature Near-Field NanoThermoMechanical Rectification," *Scientific Reports,* vol. 7, no. 44901, 2017.

[20] B. Song, D. Thompson, A. Fiorino, Y. Ganjeh, P. Reddy and E. Meyhofer, "Radiative Heat Conductances between Dielectric and Metallic Parallel Plates with Nanoscale Gaps," *Nature Nanotechnology,* vol. 11, p. 509–514, 2016.

[21] T. L. Bergman, A. S. Lavine, F. P. Incropera and D. P. Dewitt, Fundamentals of Heat and Mass Transfer 7th edition, New York: John Wiley & Sons, Inc., 2011.

[22] G. Chen, Nanoscale Enery Transport and Conversion, New York: Oxford University Press, 2005.

[23] S. J. Orfanidis, Electromagnetic Waves and Antennas, Rutgers University, 2016.

[24] "BC Open Textbooks," [Online]. Available: https://opentextbc.ca/chemistry/cnx_chem_06_01_emspectrum/. [Accessed 15 8 2019].

[25] S. M. Rytov, Y. A. Kravtsov and V. I. Tatarskii, Principles of Statistical Radiophysics 3, Springer-Verlag Berlin Heidelberg, 1989.

[26] H. B. Callen and T. A. Welton, "Irreversibility and Generalized Noise," *Physical Review,* vol. 83, no. 1, pp. 34-40, 1951.

[27] M. T. H. Reid, A. W. Rodriguez and S. G. Johnson, "Fluctuation-Induced Phenomena in Nanoscale Systems: Harnessing the Power of Noise," *Proceedings of the IEEE,* vol. 101, no. 2, pp. 531-545, 2013.

[28] S. Basu, Near-Field Radiative Heat Transfer across Nanometer Vacuum Gaps, Oxford, UK: Elsevier, 2016.

[29] B. Song, A. Fiorino, E. Meyhofer and P. Reddy, "Near-Field Radiative Thermal Transport: From Theory to Experiment," *AIP Advances,* vol. 5, no. 053503, pp. 1-47, 2015.

[30] K. Park and Z. Zhang, "Fundamentals and Applications of Near-Field Radiative Energy Transfer," *Frontiers in Heat and Mass Transfer,* vol. 4, no. 013001, pp. 1-26, 2013.

[31] M. Francoeur and M. P. Mengüç, "Role of Fluctuational Electrodynamics in Near-Field Radiative Heat Transfer," *Journal of Quantitative Spectroscopy and Radiative Transfer,* vol. 109, no. 2, p. 280–293, 2008.

[32] A. F. Peterson, S. L. Ray and R. Mittra, Computational Methods for Electromagnetics, Oxford, New York: Oxford University Press, 1998.

[33] R. Paknys, Applied Frequency-Domain Electromagnetics, Chichester, UK: John Wiley & Sons, Ltd, 2016.

[34] M. Francoeur, M. P. Menguc and R. Vaillon, "Solution of Near-Field Thermal Radiation in One-Dimensional Layered Media Using Dyadic Green's Functions and the Scattering Matrix Method," *Journal of Quantitative Spectroscopy & Radiative Transfer,* vol. 110, pp. 2002-2018, 2009.

[35] L. Tsang, J. A. Kong and K.-H. Ding, Scattering of Electromagnetic Waves. Theories and Applications, John Wiley & Sons, Inc. , 2000.

[36] M. Francoeur, "Near-Field Radiative Transfer: Thermal Radiation, Thermophotovoltaic Power Generation and Optical Characterization," University of Kentucky Doctoral Dissertation, 2010.

[37] M. Elzouka and S. Ndao, "Near-Field NanoThermoMechanical Memory," *Applied Physics Letters,* vol. 105, no. 243510, 2014.

[38] A. Narayanaswamy and G. Chen, "Direct Computation of Thermal Emission from Nanostructures," *Annual Reviews of Heat Transfer,* vol. 14, pp. 169-195, 2005.

[39] M. Francoeur, M. P. Menguc and R. Vaillon, "Spectral Tuning of Near-Field Radiative Heat Flux between Two Thin Silicon Carbide Films," *Journal of Physics D: Applied Physics,* vol. 43, no. 075501, pp. 1-12, 2010.

[40] X. Liu, L. Wang and Z. M. Zhang, "Near-Field Thermal Radiation: Recent Progress and Outlook," *Nanoscale and Microscale Thermophysical Engineering,* vol. 19, pp. 98-126, 2015.

[41] "Binary to Decimal Conversion," Electronics Tutorials, [Online]. Available: https://www.electronics-tutorials.ws/binary/bin_2.html. [Accessed 25 June 2018].

[42] A. Hamed, M. Elzouka and S. Ndao, "Thermal Calculator," *International Journal of Heat and Mass Transfer,* vol. 134, pp. 359-365, 2019.

[43] L. Que, J.-S. Park and Y. B. Gianchandani, "Bent-Beam Electrothermal Actuators—Part I: Single Beam and Cascaded Devices," *Journal of Microelectromechanical Systems,* vol. 10, no. 2, pp. 247-254, 2001.

[44] C. Guan and Y. Zhu, "An Electrothermal Microactuator with Z-Shaped Beams," *Journal of Micromechanics and Microengineering,* vol. 20, no. 085014, pp. 1-9, 2010.

[45] G. K. Lau, J. Goosen, F. v. Keulen, T. C. Duc and P. Sarro, "Polymeric Thermal Microactuator With Embedded Silicon Skeleton: Part I—Design and Analysis," *Journal of Microelectromechanical Systems,* vol. 17, no. 4, pp. 809-822, 2008.

[46] T. C. Duc, G. K. Lau and P. Sarro, "Polymeric Thermal Microactuator with Embedded Silicon Skeleton: Part II—Fabrication, Characterization, and Application for 2-DOF Microgripper," *Journal of Microelectromechanical Systems,* vol. 17, no. 4, pp. 823-831, 2008.

[47] B. Piriyanont and S. O. R. Moheimani, "MEMS Rotary Microgripper with Integrated Electrothermal Force Sensor," *Journal of Microelectromechanical Systems,* vol. 23, no. 6, pp. 1249-1251, 2014.

[48] R. Zhang, J. Chu, H. Wang and Z. Chen, "A Multipurpose Electrothermal Microgripper for Biological Micro-Manipulation," *Microsystem Technologies,* vol. 19, no. 1, pp. 89-97, 2013.

[49] Z. Wang, X. Shen and X. Chen, "Design, Modeling, and Characterization of a MEMS Electrothermal Micogripper," *Microsystem Technologies,* vol. 21, no. 11, pp. 2307-2314, 2015.

[50] S. Iamoni and A. Somà, "Design of an Electro Thermally Actuated Cell Microgripper," *Microsystem Technologies,* vol. 20, no. 4-5, pp. 869-877, 2014.

[51] P. Shivhar, G. U. and M. Umapathy, "Design Enhancement of a Chevron Electrothermally Actuated Microgripper for Improved Gripping Performance," *Microsystem Technologies,* vol. 22, no. 11, pp. 2623-2631, 2016.

[52] A. Somà, S. Iamoni, R. Voicu, R. Müller, M. H. M. Al-Zandi and C. Wang, "Design and Experimental Testing of an Electro-Thermal Microgripper for Cell Manipulation," *Microsystem Technologies,* vol. 24, no. 2, pp. 1053-1060, 2018.

[53] J. J. Khazaai, M. Haris, H. Qu and J. Slicker, "Displacment Amplification and Latching Mechanism Using V-Shape Actuators in Design of Electro-Thermal MEMS Switches," in *IEEE SENSORS 2010*, 2010.

[54] M. Daneshmand, S. Fouladi, R. R. Mansour, M. Lisi and T. Stajcer, "Thermally Actuated Latching RF MEMS Switch and its Characteristics," *IEEE Transactions on Microwave Theory and Techniques,* vol. 57, no. 12, pp. 3229-3238, 2009.

[55] D. Shojaei-Asanjan, M. Bakri-Kassem and R. R. Mansour, "Analysis of Thermally Actuated RF-MEMS Switches for Power Limiter Applications," *Journal of Microelectromechanical Systems,* vol. 28, no. 1, pp. 107-113, 2019.

[56] J. Qiu, J. H. Lang, A. H. Slocum and A. C. Weber, "A Bulk-Micromachined Bistable Relay with U-Shaped Thermal Actuators," *Journal of Microelectromechanical Systems,* vol. 14, no. 5, pp. 1099-1109, 2005.

[57] A. Rahafrooz, A. Hajjam, B. Tousifar and S. Pourkamali, "Thermal Actuation, a Suitable Mechanism for High Frequency Electromechanical Resonators," in *IEEE 23rd International Conference on Micro Electro Mechanical Systems (MEMS)*, Wanchai, Hong Kong, China, 2010.

[58] J. H. Seo and O. Brand, "High Q-Factor In-Plane-Mode Resonant Microsensor Platform for Gaseous/Liquid Environment," *Journal of Microelectromechanical Systems,* vol. 17, no. 2, pp. 483-493, 2008.

[59] A. Hajjam, A. Rahafrooz, J. Wilson and S. Pourkamali, "Thermally Actuated MEMS Resonant Sensors for Mass Measurement of Micro/Nanoscale Aerosol Particles," in *SENSORS, 2009 IEEE*, 2009.

[60] L. L. Chu and Y. B. Gianchandani, "A Micromachined 2D Positioner with Electrothermal Actuation and Sub-Nanometer Capacitive Sensing," *Journal of Micromechanics and Microengineering,* vol. 13, pp. 279-285, 2003.

[61] Y. Zhu, A. Corigliano and H. D. Espinosa, "A Thermal Actuator for Nanoscale in Situ Microscopy Testing: Design and Characterization," *Journal of Micromechanics and Microengineering,* vol. 16, pp. 242-253, 2006.

[62] Y. Zhu and H. D. Espinosa, "An Electromechanical Material Testing System for in Situ Electron Microscopy and Applications," *PNAS (Proceedings of the National Academy of Sciences of the United States of America),* vol. 102, no. 44, pp. 14503-14508, 2005.

[63] Q.-A. Huang and N. K. S. Lee, "Analysis and Design of Polysilicon Thermal Flexure Actuator," *Journal of Micromechanics and Microengineering,* vol. 9, pp. 64-70, 1999.

[64] N. D. Mankame and G. K. Ananthasuresh, "Comprehensive Thermal Modelling and Characterization of an Electro-Thermal-Compliant Microactuator," *Journal of Micromechanics and Microengineering,* vol. 11, pp. 452-462, 2001.

[65] R. Hickey, D. Sameoto, T. Hubbard and M. Kujath, "Time and Frequency Response of Two-Arm Micromachined Thermal Actuators," *Journal of Micromechanics and Microengineering,* vol. 13, pp. 40-46, 2003.

[66] C. D. Lott, T. W. McLain, J. N. Harb and L. L. Howell, "Modeling the Thermal Behavior of a Surface-Micromachined Linear-Displacement Thermomechanical Microactuator," *Sensors and Actuators A: Physical,* vol. 101, no. 1-2, pp. 239-250, 2002.

[67] H. Steiner, F. Keplinger, J. Schalko, W. Hortschitz and M. Stifter, "Highly Efficient Passive Thermal Micro-Actuator," *Journal of Microelectromechanical Systems,* vol. 13, pp. 40-46, 2015.

[68] J. Ouyang and Y. Zhu, "Z-Shaped MEMS Thermal Actuators: Piezoresistive Self-Sensing and Preliminary Results for Feedback Control," *Journal of Microelectromechanical Systems,* vol. 21, no. 3, pp. 596-604, 2012.

[69] Y. Zhu, S. O. R. Moheimani and M. R. Yuce, "Bidirectional Electrothermal Actuator with Z-Shaped Beams," *IEEE Sensors Journal,* vol. 12, no. 7, pp. 2508-2509, 2012.

[70] M. McCarthy, N. Tiliakos, V. Modi and L. G. Fréchette, "Thermal Buckling of Eccentric Microfabricated Nickel Beams as Temperature Regulated Nonlinear Actuators for Flow Control," *Sensors and Actuators A: Physical,* vol. 134, no. 1, pp. 37-46, 2006.

[71] K. Ogando, N. L. Forgia, J. Zárate and H. Pastoriza, "Design and Characterization of a Fully Compliant Out-of-Plane Thermal Actuator," *Sensors and Actuators A: Physical,* vol. 183, pp. 95-100, 2012.

[72] S. D. Nguyen and E. Halvorsen, "Nonlinear Springs for Bandwidth-Tolerant Vibration Energy Harvesting," *Journal of Microelectromechanical Systems,* vol. 20, no. 6, pp. 1225-1227, 2011.

[73] Y. Lu, F. Cottone, S. Boisseau, F. Marty, D. Galayko and P. Basset, "A Nonlinear MEMS Electrostatic Kinetic Energy Harvester for Human-Powered Biomedical Devices," *Applied Physics Letters,* vol. 107, no. 253902, pp. 1-5, 2015.

[74] P. Basset, D. Galayko, F. Cottone, R. Guillemet, E. Blokhina, F. Marty and T. Bourouina, "Electrostatic Vibration Energy Harvester with Combined Effect of Electrical Nonlinearities and Mechanical Impact," *Journal of Micromechanics and Microengineering,* vol. 24, no. 035001, pp. 1-14, 2014.

[75] J. P. Bentley, "Temperature Sensor Characteristics and Masurement System Design," *Journal of Physics E: Scientific Instruments,* vol. 17, no. 6, pp. 430-439, 1984.

[76] R. J. Moffat, "Describing the uncertainties in experimental results," *Experimental Thermal and Fluid Science,* vol. 1, no. 1, pp. 3-17, 1988.

[77] I. Keithley Instruments, "System SourceMeter® Specifications Model 2611B, 2612B and 2614B," 2013.

[78] I. Keithley Instruments, "System SourceMeter® Specifications Model 2601B, 2602B and 2604B," 2013.

[79] M. Elzouka and S. Ndao, "Meshed Doped Silicon Photonic Crystals for Manipulating Near-Field Thermal Radiation," *Journal of Quantitative Spectroscopy & Radiative Transfer,* vol. 204, pp. 56-62, 2018.

[80] I. Lake Shore Cryotronics, "User's Manual Model 335 Temperature Controller," 2014.

Appendix: Uncertainty Analysis

In our experiment for measuring thermal expansion mechanisms, we have the following uncertainties:

1- Uncertainty in electrical measurements for current, voltage, resistance and dissipated power, denoted by $\delta I, \delta V, \delta R,$ and δP, respectively, for all microheaters:

Electrical measurements were performed using Keithley SourceMeter 2602B and 2611B. The uncertainty in measured voltage and measured current was adopted from the datasheet document *'Model 2601B, 2602B and 2604B System SourceMeter®️ Specifications'* and *'Model 2611B, 2612B and 2614B System SourceMeter®️ Specifications'* [77] [78].

Current Range	Uncertainty of measured δI (2602B Model)	Uncertainty of measured δI (2611B Model)
$\leq 100\ \mu A$	$0.02\ \% + 25\ nA$	$0.02\ \% + 25\ nA$
$\leq 1\ mA$	$0.02\ \% + 200\ nA$	$0.02\ \% + 200\ nA$
$\leq 10\ mA$	$0.02\ \% + 2.5\ \ \mu A$	$0.02\ \% + 2.5\ \ \mu A$

Voltage Range	Uncertainty of measured δV (2602B Model)	Uncertainty of measured δV (2611B Model)
$\leq 1\ V$	$0.015\ \% + 200\ \mu V$	
$\leq 6\ V$	$0.015\ \% + 1\ mV$	
$\leq 40\ V$	$0.015\ \% + 8\ mV$	
$\leq 2\ V$		$0.02\ \% + 350\ \mu V$

$\leq 20\ V$		$0.015\ \% + 5\ mV$
$\leq 200\ V$		$0.015\ \% + 50\ mV$

The uncertainty in the calculated resistance and power were calculated using the technique published by Moffat [76]:

$$\delta R = \sqrt{\left(\frac{\partial R}{\partial V}\delta V\right)^2 + \left(\frac{\partial R}{\partial I}\delta I\right)^2} = \sqrt{\left(\frac{1}{I}\delta V\right)^2 + \left(-\frac{V}{I^2}\delta I\right)^2}$$

$$\delta P = \sqrt{\left(\frac{\partial P}{\partial V}\delta V\right)^2 + \left(\frac{\partial P}{\partial I}\delta I\right)^2} = \sqrt{(I\delta V)^2 + (V\delta I)^2}$$

2- Uncertainty in chuck temperature measurement (denoted by δT_{ch}):

Chuck temperature measurements were performed using the Lake Shore temperature controller (335 series). We used a resistance temperature detector (RTD) made of platinum, with a positive temperature coefficient (PTC). The temperature measurement error was adopted from the user's manual [80], which was 62 mK for a temperature range below 300 K, and 106 mK otherwise.

3- Uncertainty in the correlation between the microheater resistance and its temperature (denoted by δTCR)

The temperature coefficient of resistance (TCR) is calculated from the experimental relationship between the microheater resistance and its corresponding temperature (i.e., chuck temperature). The TCR relation was found by regression analysis; by fitting the experimental data points corresponding to microheater resistance and its corresponding

temperature (i.e., chuck temperature) to a linear relationship. The uncertainty in the TCR

at each point (δTCR) was assumed to be the maximum of the two values; δT, and $\delta R \times \frac{dT}{dR}$.

$\frac{dT}{dR}$ was determined by the TCR relationship (i.e., the slope of the fitting curve).

4- Uncertainty in estimating the mechanism's temperature (denoted by δT)

During heat transfer experiments, the microheater temperature was estimated from

resistance measurement. The uncertainty of estimated temperature can be evaluated from

the relationship $\delta T = \delta R \times \frac{dT}{dR} + \delta TCR$.

5- Uncertainty in estimating mechanism's displacement (denoted by $\delta \Delta$)

The images captured by the microscope were analyzed by MATLAB to estimate

the distance displaced by the mechanisms' terminals. The distance between the terminal

surface and a certain surface reference in the microstructure is expressed in pixels of the

captured image. Before supplying the current through the microheater, the measured

distance is considered the minimum distance D_{min} of the terminal surface. By supplying

the current gradually, the distance D increases due to the displacement of the terminal

surface. The maximum distance D_{max} measured by supplying the maximum current

through the microheater. The relative displacement Δ and its uncertainty are defined as:

$$\Delta = \frac{D_{max} - D}{D_{max} - D_{min}}$$

$$\delta \Delta = \sqrt{\left(\frac{\partial \Delta}{\partial D} \delta D\right)^2 + \left(\frac{\partial \Delta}{\partial D_{min}} \delta D_{min}\right)^2 + \left(\frac{\partial \Delta}{\partial D_{max}} \delta D_{max}\right)^2}$$

$\delta\Delta$

$$= \sqrt{\left(\frac{-1}{D_{max} - D_{min}}\delta D\right)^2 + \left(\frac{D_{max} - D}{(D_{max} - D_{min})^2}\delta D_{min}\right)^2 + \left(\left(\frac{1}{D_{max} - D_{min}} - \frac{D_{max} - D}{(D_{max} - D_{min})^2}\right)\delta D_{max}\right)^2}$$

where δD, δD_{min}, and δD_{max} are estimated to be 1 pixel each.

6- Uncertainty in estimating the thermal gate's effectiveness (denoted by $\delta\varepsilon$)

The effectiveness, ε, of the thermal gate and its uncertainty are defined as:

$$\varepsilon = \frac{T_{out} - T_{min}}{T_{max} - T_{min}}$$

$$\delta\varepsilon = \sqrt{\left(\frac{\partial\varepsilon}{\partial T_{out}}\delta T_{out}\right)^2 + \left(\frac{\partial\varepsilon}{\partial T_{min}}\delta T_{min}\right)^2 + \left(\frac{\partial\varepsilon}{\partial T_{max}}\delta T_{max}\right)^2}$$

$$\delta\varepsilon = \sqrt{\left(\frac{1}{T_{max} - T_{min}}\delta T_{out}\right)^2 + \left(\frac{T_{out} - T_{max}}{(T_{max} - T_{min})^2}\delta T_{min}\right)^2 + \left(\frac{T_{min} - T_{out}}{(T_{max} - T_{min})^2}\delta T_{max}\right)^2}$$